DEVELOPMENT AND CHARACTERIZATION OF DIFFERENT INSULIN BASED NANOFORMULATIONS FOR WOUND HEALING ACTIVITY

Thesis submitted in the fulfilment of the

requirement of the degree of

Doctor of Philosophy

Submitted by

Pawandeep Kaur

(Regn. No. 901609008)

THAPAR INSTITUTE
OF ENGINEERING & TECHNOLOGY
(Deemed to be University)

Under the Supervision of

Dr. Diptiman Choudhury

(Assistant Professor)

SCHOOL OF CHEMISTRY AND BIOCHEMISTRY

THAPAR INSTITUTE OF ENGINEERING AND TECHNOLOGY

PATIALA-147004

PUNJAB, INDIA

Candidate's Declaration

I, hereby declare that the work presented in the thesis entitled "**DEVELOPMENT AND CHARACTERIZATION OF DIFFERENT INSULIN BASED NANOFORMULATIONS FOR WOUND HEALING ACTIVITY**" in partial fulfilment of the requirement for the award of the Degree of Philosophy, School of Chemistry and Biochemistry, Thapar Institute of Engineering and Technology, Patiala, is an authentic record of my own work carried out under the supervision of Dr. Diptiman Choudhury, Assistant Professor, School of Chemistry and Biochemistry, Thapar Institute of Engineering and Technology, Patiala, India. The matter embodied in this thesis has not been submitted in part or full to any other university or institute for the award of any degree in India or Abroad.

Pawandeep Kaur

Pawandeep Kaur
Reg. No. 901609008
School of Chemistry and Biochemistry
Thapar Institute of Engineering and Technology, Patiala-147004
Punjab (India)

Dr. Diptiman Choudhury
(Supervisor)
Assistant Professor
School of Chemistry and Biochemistry
Thapar Institute of Engineering and Technology, Patiala-147004
Punjab (India)

i

Certificate

This is to certify that thesis entitled "**DEVELOPMENT AND CHARACTERIZATION OF DIFFERENT INSULIN BASED NANOFORMULATIONS FOR WOUND HEALING ACTIVITY**" being submitted by Pawandeep Kaur in the fulfilment of the requirement for the award of the Degree of Philosophy, School of Chemistry and Biochemistry, Thapar Institute of Engineering and Technology, Patiala, is an authentic record of candidate's own work carried out by her under my supervision and guidance. The matter embodied in this thesis has not been submitted in part or full to any other university or institute for the award of any degree in India or Abroad.

Dr. Diptiman Choudhury
(Supervisor)
Assistant Professor
School of Chemistry and Biochemistry
Thapar Institute of Engineering and Technology, Patiala-147004
Punjab (India)

Dr. Susheel Mittal
(Head of SCBC)
School of Chemistry and Biochemistry
Thapar Institute of Engineering and Technology, Patiala-147004
Punjab (India)

ii

Acknowledgement

I wholeheartedly thank my mighty God for giving me the vision, power, spirit and endurance to complete the interesting research.

Completion of this doctoral dissertation was possible with the support of people. I would like to express my sincere gratitude to all of them.

First and foremost, I would like to express my sincere gratitude to my research supervisor, Dr. Diptiman Choudhury, Assistant Professor, School of Chemistry and Biochemistry for introducing me to this exciting field of Science and for his valuable guidance, continuous support, motivation, patience, scholarly inputs and consistent encouragement. I received throughout the Ph.D. work. I have learnt extensively from his, including how to regard an old question from a new perspective and how to approach a problem by systematic thinking. He has always made himself available to clarify my doubts despite his busy schedules and I consider it as a great opportunity to do my doctoral programme under his guidance and to learn from his research expertise. His mentorship was paramount in providing a well round experience consistent my long term career goals. His persistent courage and confidence will always inspire me, and I hope to continue to work with his novel thoughts. I am also grateful to Dr. Bishwrap Basu and his co-workers, Department of Pharmacy, Amity University, Noida for carrying out the *in vivo* experiments on Wister rat model and they were cared animals as per the standards of CPCSEA, New Delhi, Govt of India and approved protocol of institutional animal ethical committee (Approval Number: CPCSEA/IAEC/AIP/2016/04/13).

I express my gratitude to Director, Thapar Institute of Engineering & Technology, Patiala, Dr. Rafat Siddique, Dean of Research and Sponsored Projects (RSP), Prof. O.P. Pandey, former Dean RSP, Dr. Susheel Mittal (Head of SCBC), Dr. Amjad Ali (Former), Dr. Bonamali Pal (Former Head of SCBC) for all facilities which have been immensely helpful in completing my work. I am also very grateful to my doctoral committee members Dr. Manmohan Chibber, Dr. Satnam Singh and Dr. Mondem Sudhakara Reddy, for their fruitful discussion and encouragement, constructive criticism and inspirations.

I am thankful to my labmates Vanshita Goel, Parmandeep Kaur, Sunidhi Sharma, Deepinder Sharda, Komal Attri, and Poulomi Chandra who all have extended their support during my research work. Special thanks to my close thanks Dr. Sumit Singh Aggarwal, Dr. Iqubal Singh, Dr. Gulshan Kumar, and Dr. Amit Mishra, for always standing by my side and sharing

a great relationship as compassionate friends. I will recover cherish the warmth shown by them, whose smiling face always made me refreshing and also for unforgettable memories during my research work. I gained a lot from them, through their professional and scholarly interactions. I acknowledge the help of Mr. Mayank Sharma, office staff and Chander Singh Thakur, Chandar Shekhar, Hemant Sharma and Vishwanath Dass, technical staff of School of Chemistry and Biochemistry for their support in various aspects.

Some of the results described in this thesis would not have been possible without the help or laboratories at the institutes like, SAI labs, Thapar Institute of Engineering and Technology, Patiala. I thankfully acknowledge to the Dr. Manoj Raje, Chief scientist and Mr. Randeep Sharma, Institute of Microbial Technology, CSIR, Chandigarh, India for providing TEM facility. I extend my gratitude to Dr. Neha Garg and her lab members especially Kundlik Gadhave, IIT Mandi (BioX center and AMRC) for providing experimental facilities and am grateful to Ramanujan SERB grant, India (SB/S2/RJN-072/2015). I extend my thankful acknowledgment TEM facility, funded by a TPF Nanomission, GOI project at Centre for Nano and Soft Matter Sciences, Bangluru. The authors acknowledge the DBT-IPLS facility of the University of Calcutta, Kolkata for supporting the confocal microscopic study.

I gratefully acknowledge, Department of Science and Technology for INSPIRE SCHEME (DST/INSPIRE FELLOWSHIP/2016/IF160636) for providing me financial support.

I owe thanks to very special person, my beloved life partner Navjot Singh Brar, for his continued and unfailing love, support, guidance, patience, and always being there for me as a friend. I greatly value his contribution and deeply appreciate his belief in me. I consider myself the luckiest in the world to have such a lovely and caring life partner, standing beside me with his love and unconditional support.

Finally, I owe my gratitude to my respected my family members whose blessings, belief and encouragement have shown me the path to pursue goals in my life. My heartfelt regard goes to my father in law, mother in law and sister in law for their love and moral support. I thank my sister and brothers for everything they have done for me. They all have been amazing and always been there for me. I cannot thank them enough. Thank you for your everlasting love and support. This is for you!

Pawandeep Kaur

iv

DEDICATED TO

MY BELOVED

FAMILY

ABBREVIATIONS

A549	Human lung non-small epithelial carcinoma
AgNPs	Silver nanoparticles
Akt	Protein kinase B
ATCC	American type culture collection
ATE	Aqueous tulsi leaf extract
bFGF	Basal fibroblast growth factor
BSA	Bovine serum albumin
cm	Centimetre
CO_2	Carbon dioxide
ºC	Degree Celsius
CI	Combination index
Cu	Copper salt
$CuSO_4$	Copper sulfate
D_1	Zinc salt dose
D_2	Insulin dose
dl	Decilitre
DMEM	Dulbecco's modified eagle medium
DMSO	Dimethyl sulphoxide
DRS	Diffuse reflectance spectroscopy
DSC	Differential scanning calorimetry
E_a	Activation energy
4EBP-1	4E binding protein
EDAX	Electron dispersive X-ray spectroscopy
eIF4B	Eukaryotic initiation factor 4B
EP	Epithelization period
ERK	Extracellular signal regulated kinase
eNOS	Endothelial nitric oxide synthase
f_a	Affected cell fraction
F_{Corr}	Fluorescence corrected
Fmax	Fluorescence maxima
FOXO	Fork head box protein
FTIR	Fourier transform infrared

f_u	Unaffected cell fraction
g	Gram
GH	Growth hormone
ΔG	Gibbs free energy
h/hr	Hour
HCl	Hydrochloric acid
HEKa	Human epithelial keratinocyte cells
HeLa	Human cervical carcinoma cell line
HIF PHD	Hypoxia inducible factor prolylhydroxylase
Hr TEM	High-resolution transmission electron microscopy
HSI	Hyperspectral imaging
ΔH	Change in entropy
JAK	Janus kinase
JNK	Jun N-terminal kinase
I	Molar concentration of Insulin coated silver nanoparticles
IAgNP	Insulin coated silver nanoparticles
ICuQCs	Insulin copper quantum clusters
IDF	International diabetes foundation
IFN	Interferon-alpha
IGF	Insulin-like growth factor
IGF-1R	Insulin-like growth factor 1 receptor
IL	Interleukin
IP	Induced protein
IR	Insulin receptor
IL-IR	Interleukin insulin receptor
IMT	Insulator metal transition
IRS-1	Insulin receptor substrate
IZnQCs	Insulin zinc insulin quantum clusters
K	Consistency index
K_a	Association constant
KBr	Potassium permanganate
K_d	Dissociation constant
Kg	Kilogram

µl	Microliter
LDI	Laser doppler imaging
LSI	Laser speckle imaging
M1	Pro-inflammatory macrophages
M2	Anti-inflammatory macrophages
MAPK	Mitogen-activated protein kinase
MEK	MAPK ERK kinase
mg	Milligram
MIB	Metal ion binding
MIF	Migration inhibitory factor
min	Minutes
MIP	Macrophage inflammatory proteins
mm	Millimetre
MMP- 2, 4	Matrix metalloproteinase
MP	Methylparaben
MOFs	Metal-organic frameworks
MSI	Multispectral imaging
mTOR	Mechanistic target of rapamycin
MTT	3-(4, 5-dimethylthiazol-2-yl)-2, 5-diphenyltetrazolium bromide
mV	Millivolt
µM	Micro molar
n	Flow index
NADH	Nicotinamide adenine dinucleotide
NADP	Nicotinamide adenine dinucleotide phosphate
NaOH	Sodium hydroxide
NFkβ	Nuclear factor kappa beta
NIROS	Near-infrared optical scanner
NK	Natural killer
nm	Nanometre
NO	Nitric oxide
NOX	NADP oxidase
OD	Optical density
PBS	Phosphate buffered saline

PDB	Protein data bank
PDH	Pyruvate dehydrogenase
PEG	Polyethylene glycol
PFK-1	6-phosphofructo-1- kinase
PG	Propylene glycol
pH	Potential of hydrogen
PI	Propidium iodide
PI3K	Phosphoinositide-3-kinase
PKC	Protein kinase C
PMNL	Polymorphonuclear leucocytes
PP	Propylparaben
PPAR-ϒ	Peroxisome Proliferator Activated Receptor Gamma
PTIFS	Photon technology fluorescence spectrophotometer
QCs	Quantum clusters
QDs	Quantum dots
%	Percentage
r	Shear rate
R	Gas constant
RAF	Rapidly accelerated fibro sarcoma
ROS	Reactive oxygen species
rpS6	Ribosomal protein
SAED	Selected area electron diffraction
SD	Standard deviation
SERS	Surface enhanced raman scattering
SFDI	Spatial frequency domain imaging
SPR	Surface plasmon resonance
STAT	Signal transducer and activator of transcription
STZ	Streptozotocin
τ	Shear stress
T	Template protein structure
TGF	Transforming growth factor
TEM	Transmission electron microscope
TLR	Toll like receptor

TNF	Tumour necrosis factor
TNP	Tri-nitro-phenol
TSC ½	Tuberous sclerosis protein ½
UV	Ultra violet
UV CD	Ultra violet circular dichroism
VEGF	Vascular endothelial growth factor
WHO	World Health Organisation
Zn	Zinc salt
$ZnSO_4$	Zinc sulfate

Table of Contents

INTRODUCTION

Wound, loss of continuity of tissue structure (such as skin, muscle, nerves, blood vesicles, bones, etc) caused due to mechanical (such as friction, pressure, heat or cold), chemical, electrical, or radiation force exposure.[1,2] Wounds have chronic pain or completely painless, swelling (redness, heat, swelling, pain, and loss of function), susceptible to infection are the signs.[3] Wounds are either internal or external based on their origin. Internally originated wounds also like ingrown toenails or calluses, break the skin and surrounding tissue, create an external wound and open wounds; due to environmental exposure is prone to infection.[4] The different types of wounds are shown in **Figure 1**. To prevent infection; initiate a series of dynamic events, collectively known as the wound healing process.[5] But the chronic wound is characterized by a persistent rise of pro-inflammatory cytokines and low anti-inflammatory cytokines and growth signal and is a major issue for patients undergoing surgery.[6] Chronic wounds result in isolation, pain, anxiety, frustration, discomfort, and also lead to depression in patients.[7,8] All conditions affect the normal life, emotions, behavior, and thought pattern of the patient and ruin the quality of life.[9]

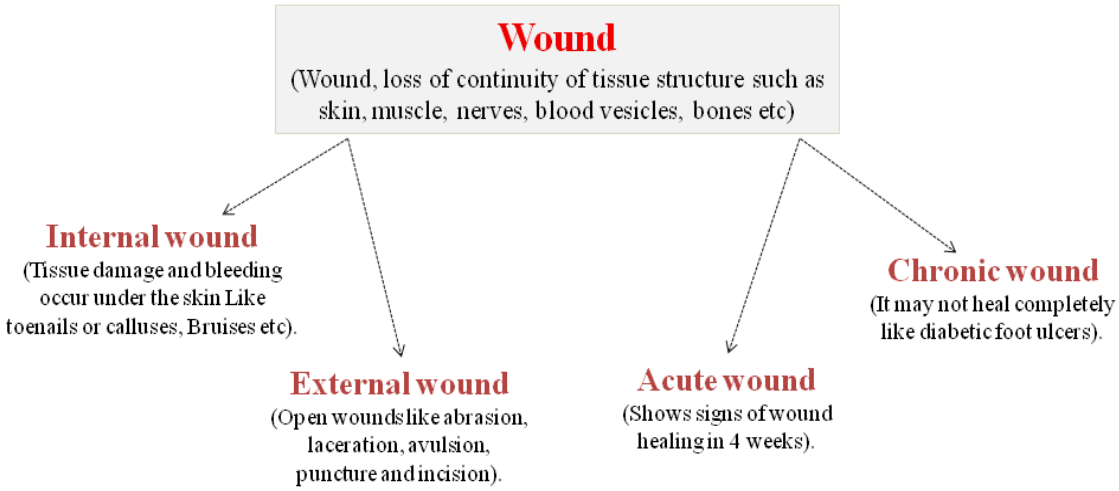

Figure 1: *Showing the different types of wounds.*

The wound healing process riles on activation of a cascade of physiological events such as hemostasis, inflammation, proliferation, remodeling.[10] The inflammation plays an important role throughout this process, the fast recovery of the wound depends on the transition of pro-inflammatory (M1 macrophages) to anti-inflammatory (M2 macrophages) and in chronic wounds, delay in transition in chronic wounds result in a prolonged proinflammatory phase leading to delay in wound healing.[11] In the early phase, macrophage functions through the release of cytokines (including IL-6 (interleukin), IL-12, IL-1β, TNF-α

(tumor necrosis factor), etc) and activating leucocytes to produce proinflammatory response.[12] Secretion of anti-inflammatory cytokines (including IL-4, IL-10, IL-13, TFG-β, etc) is responsible for the closure of the wound and induces angiogenesis and re-epithelialization.[13] In **Figure 2** the various phases of wound healing are shown.

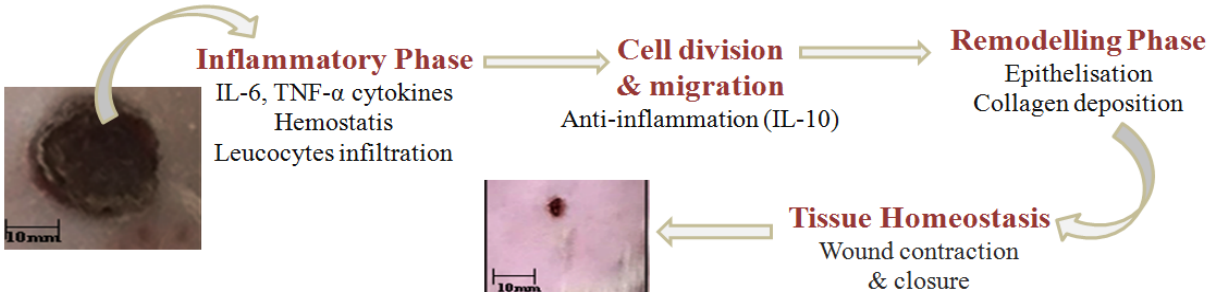

Figure 2: *Schematic diagram of the wound healing process.*

Diabetes is characterized by the presence of a chronic high free glucose level in the body fluid, including blood, urine, sweat, etc.[14] Among one of the main reasons for the occurrence of the diseases is the failure of hormone-mediated metabolic regulation. Hormones such as insulin and glucagon play the most important role in maintaining the sugar balance in the blood.[15] Maintaining a steady balance of sugar in the blood is very critical for the normal functioning of the body.[16] The presence of excess glucose in body fluids leads to various pathological conditions such as susceptibility to infection, inducing the onset of various diseases like cataract, retinopathy, neuropathy, arthritis, hypertension, cardiovascular problems, kidney damage, damaged blood vesicles, and a delay in wound healing, etc.[16,17]

About 422 million people are suffering from diabetes worldwide making it the 8th most fatal disease (WHO, 2016 report).[18,19] Estimated 15-25% of diabetic patients will develop foot ulcers with more than 6% needing clinical attention among which 15-20% will need amputation of lower limb due to worsening of the wound.[20] This counts for around 50% of all traumatic amputations and has a five years postsurgical survival rate of less than 50%.[21,22] Wound leads to activation of the pro-inflammatory pathway followed by an anti-inflammatory cascade, responsible for the healing process. But the chronic diabetic wound is characterized by a persistent raise of pro-inflammatory cytokines and low anti-inflammatory cytokines and growth signal and is a major issue for patients undergoing surgery.[23] Numerous approaches including various kinds of dressings stem cell-based therapies and use of growth factors (epithelial growth factor (EGF), platelet-derived growth factor (PDGF), fibroblast growth factor (FGF), transforming growth factor-beta (TGF-β), and insulin-like growth

factor-1 (IGF-1) have been targeted to treat diabetic wounds.[24,25] Despite potential usefulness is limited due to limitation including moisture associated delaying (alginates based dressings), reduced aeration (hydrocolloid based dressings), low mechanical strength (hydrogels based dressing), high cost (stem cell and growth factors based therapies) and increase in the economic burden.[26-31]Healing of diabetic wound attained the great attention of investigators but promising therapeutic intervention is still awaited. Insulin is one of the most common and effective therapeutic choices for the treatment of type-I diabetes. Healing of wound attained the great attention of investigators but promising therapeutic intervention is still awaited. Insulin is one of the most common and effective therapeutic choices for the treatment of diabetes type-I; it acts as an anti-inflammatory agent by activating cytokines which can reduce inflammation and promotes glucose uptake by cells thereby helping maintenance of blood glucose level.[32]Insulin also works as a cellular growth promotes and works through insulin-like growth factor receptor-I (IGFR-I) binding.[33]

According to the International Diabetes Federation (IDF) data till 2019, 463 million people were having diabetes.[34] IDF estimates that by 2045 the diabetic cases raise from 628 to 700 million.[34,35] The patients suffering from diabetes are at 25% risk of developing foot ulcers.[36] More than 6% of diabetic ulcer patients needing clinical attention among which 15-20% will need amputation of lower limb due to worsening of the wound.[37] Despite so many uses of insulin as anti-diabetic agents, it has rarely been explored for its wound healing activities. The total accomplished work in this dissertation has been divided into the following chapters:

Chapter 1: Review of literature

Chapter 2: Mechanism of wound healing by insulin

Chapter 3: Insulin capped silver nanoparticles

Chapter 4: Amorphous insulin zinc quantum clusters

Chapter 5: Crystalline insulin copper quantum clusters

CHAPTER-1
REVIEW OF LITERATURE

1.1. Insulin structure

Insulin, a peptide hormone produced by beta cells of the islets of Langerhans of the pancreas. The precursor of insulin is proinsulin, a single polypeptide encoded by the INS gene in humans, after processing 2 secretory proteins are generated, with one consisting of two chains namely A and B (21 and 30 amino acids respectively) that generates mature insulin and the second is the C chain of 31 amino acids, commonly known C-peptide.[38,39] The "A" chain is fairly compact and has 2 small α helical regions whereas the B chain has only one of such kind. 2 disulfide linkages between A7-B7 and A20-B19 hold the A and B chains together, other than the internal disulfide bridge of the A chain (A7-A11). Insulin exists in hexameric and monomeric forms and is stored in the pancreas.[40] Receptor binding depends upon several regions present in insulin. These regions are mainly present at the surface; mutations in these regions reduce the affinity of binding of insulin.[41]

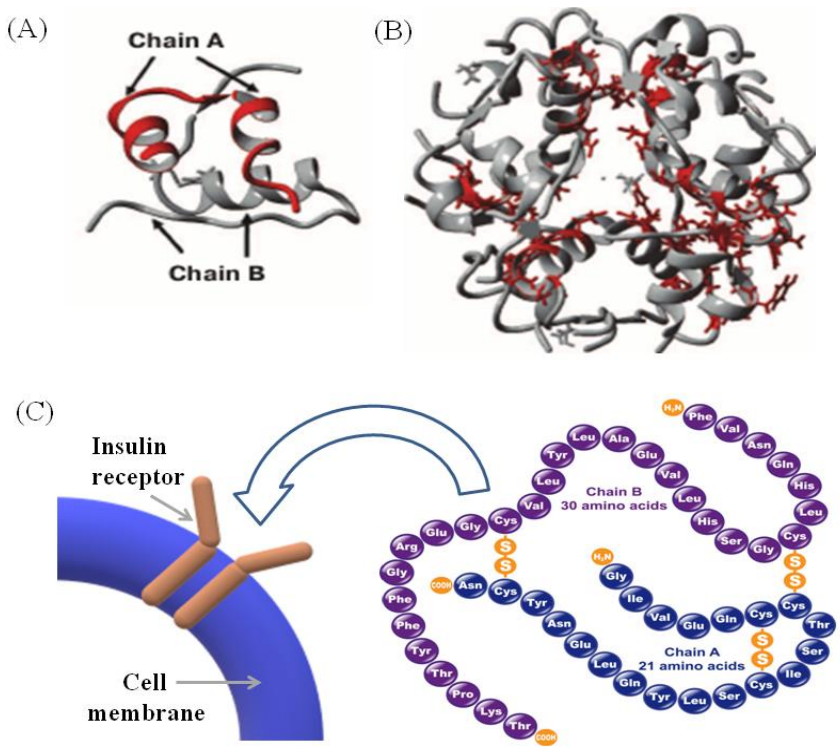

Figure 3: *Insulin structure* (A) *monomer* (B) *hexamer and* (C) *its binding to the insulin receptor.*[42,43]

The regions are located at GlyA1 (glycine), IleA2 (isoleucine), ValA3 (valine), GluA4 (glutamine) on the N terminus, and TyrA19 (tyrosine), CysA20 (cysteine), AsnA21 (asparagine) on the C-terminus of the "A" chain, and at GlyB23(glycine), PheB24

(phenylalanine), PheB25, and TyrB26 at the C-terminus of the "B" chain.[44] Not only present in humans, but insulin-like peptides are also found in invertebrates such as molluscs and insects. The growth-related function of insulin-like peptides shows that insulin is not only involved in glucose metabolism.[45]

1.2. Insulin as a wound-healing agent

Over the last 25 years, there has been a fourfold increase in cases of diabetes mellitus, commonly known as diabetes.[46] In the year 2016, worldwide 422 million people have been reported to have diabetes. According to the World Health Organisation (WHO), diabetes is the 8th leading cause of death and was directly associated with 1.5 million deaths worldwide in the year 2012.[47] Due to the association of these diseases with diabetes, the International Diabetes Foundation (IDF) estimated the loss of 4.9 million lives, ~1.25% of all diabetic patients in 2014, as being directly or indirectly caused due to diabetes.[48] These diseases are associated and affect various organs of the body with different pathologies, however; all these pathological conditions are associated with tissue inflammation.[49] Diabetes induces low-grade systemic inflammation and promotes disease conditions such as hypertension, arthritis, retinopathy, etc.[50]

One of the important aspects of diabetes to inflammation is its association with delayed wound healing.[51] The chronic diabetic wound is characterized by the persistent increment of pro-inflammatory cytokines and the absence of growth signal in damaged tissues.[52] Various diabetes treatments help control blood glucose levels and thereby can also delay the progression of the diseases associated with diabetes, such as hypertension, arthritis, retinopathy, cataract, neuropathy, etc, but very little is known about their effect on the recovery of diabetic wounds.[53] Wounding induces tissue inflammation and induces the release of various pro-inflammatory cytokines such as interleukin-1 (IL-1), IL-6, IL-12, IL-18, interferon-gamma (IFN-γ), and tumor necrosis factors (TNFs).[54,55] Pro-inflammatory cytokines, such as IL-1β, IL-6, secreted from monocytes, and macrophages in wound tissue triggers pain responses by stimulating neuronal signaling.[56] IFN-γ, TNF-α, and IL-1β induce tissue apoptosis and pyroptosis mediated by oxidative stress and by activating innate immunity.[57] IFN-γ is a potent activator of tissue macrophages by modulating STAT1 expression to generate a foreign pathogen defense state in the affected area.[58] IL-12 stimulates the production of IFN-γ and TNF-α and reduces IL-4, anti-inflammatory cytokine-mediated suppression of IFN-γ, IL-4 inhibits IFN-γ through STAT3 signaling.[59] IL-18 activates Natural killer (NK) cells and T cells thereby promoting the release of IFN-γ in

wound conditions for pathogen defense.[60] However, the persistence of prolonged inflammatory conditions is detrimental and causes tissue damage which eventually delays the repair process. IL-1 is a potent activator of TNFs and therefore induces cell damage. Overproduction of IL-1β is especially involved in neuronal inflammation and causes the damage of neuromuscular junctions, which delays the wound healing procedure. The FDA has approved the use of IL-1 blockers as an effective therapeutic approach to fight against rheumatoid arthritis.[61] Macrophages, in response to foreign pathogens, secrete IL-6 which infers Toll-like receptor (TLR), especially the TLR-9 response-mediated defense against the foreign pathogen by killing it. The TLR-9 pathway is activated by unmethylated DNA which is present in prokaryotes and kills the pathogen. But in the case of a wound, spillage of mitochondrial DNA takes place, which is essentially unmethylated DNA and triggers a similar response in the injured tissue.[62] IL-12 inhibits the formation of new blood vessels in the tissue by IFN-γ-mediated overexpression of Interferon gamma-induced protein 10 (IP-10 or CXCL-10).[63] IL-18 suppresses the expression of vascular endothelial growth factor (VEGF) which is essential for cell blood vessel development of the wound tissue and it is, therefore, essential for growth and repair.[64]

Overcoming the inflammatory response is important to initiate and control the repair mechanism. In the normal course, anti-inflammatory cytokines such as IL4, IL-10, IL-11, IL-13, Interferon-alpha (IFN-α), and transforming growth factor-beta (TGF-β) play crucial roles in the wound recovery process.[65] TLR-9 response at an early phase causes rapid production of pro-inflammatory signals such as TNF-α via rapid activation of p38/ mitogen-activated protein kinase (MAPK) and the c-Jun N-terminal kinase (JNK) pathway.[66] In normal conditions, the prolonged activation of MAPK results in activation of MAPK phosphatase which works as a feedback inhibitor of p38/MAPK and JNK pathways, resulting in the downregulation of TNF-α production. Dephosphorylated p38/MAPK results in the production of anti-inflammatory cytokines IL-10, homodimeric (35 kDa) cytokine, produced by monocytes, macrophages and induce TGF-β signaling which promotes cell division.[67] Like IL-10, IL-4 and IL-13 also stimulate the synthesis of fibrinogen and the extracellular matrix, especially collagens. IL-4, a 20 kDa cytokine, is secreted from inflamed T cells, mast cells, and macrophages and activates Janus kinase/ signal transducer and activator of transcription-6 (Jak/STAT6) pathway promoting wound repair.[68] IL-4 helps in the synthesis of the extracellular matrix, especially collagen which provides the physical support for wound recovery.[69] Another cytokine, L-1RA, is secreted by cells including immune cells, epithelial cells, and adipocytes, and shows inhibition of the IL-1β pro-inflammatory effect by

binding itself to the interleukin-1 receptor (IL-1R). On the other hand, deregulation of IL-1β and TNF-α prolongs the inflammatory phase and delays healing.[70] IL-11, a 23 kDa protein released by bone marrow cells shows its anti-inflammatory activity. IL-11 inhibits IL-1 and TNF-α synthesis through $NFk\beta^{P50/P65}$ inhibition by up-regulating inhibitory $NFk\beta^{P50/P50}$ synthesis in monocytes/macrophages cells.[71] The dynamics between pro-inflammatory and anti-inflammatory cytokines are critically maintained in normal physiological conditions for the effective wound recovery process, but in diabetic conditions, the normal dynamics of the cytokines get impaired.

The first line of diabetes treatment for insulin-dependent, type-I diabetes is the administration of insulin systematically. Although very few studies have been performed involving insulin as a wound-healing agent, S.E. Greenway and his co-workers in 1999 from Harbor-UCLA Medical Center, Torrance, California showed almost 25% faster recovery of the wound in the case of diabetic patients. They found that the wound of the five diabetic subjects healed in 6.6 ± 1.7 days with insulin treatment and 8.8 ± 1.6 days with saline, a difference of 2.2 ± 0.6 days. They also found that insulin has wound healing activity even in non-diabetic patients. They found that the wounds of the six nondiabetic subjects healed in 4.8 ± 0.4 days with insulin treatment and 7.3 ± 0.7 days with saline, a difference of 2.5 ± 0.5 days, which is almost 35% faster than the placebo.[72] But in spite of the promising result, not much follow-up has been done in this respect. In another study in 2012, it was shown that the application of insulin topically inhibits the infiltration of neutrophils in wound tissue in diabetic mice.[73] A few other discrete works in 2017 showed that topical insulin is beneficial in burn wound healing in diabetic rats.[74] W. Li and his co-workers in 2019 prepared synthesized keratin conjugated hydrogel of insulin to check its wound-healing effect. These showed promotion in hemostasis, regulates hydroxyproline (HYP) and transforming growth factor β1 (TGF-β1) expression level.[75]

1.3. Insulin based nanoformulations as a wound-healing agent

Numerous approaches for developing nanoformulations of insulin have been carried out. In 2017, X. Li and co-workers synthesized the microparticles of silk fibroin encapsulating insulin and showed deposition of collagen, vascularisation, and significant promotion in wound healing.[76] A. Ehterami and other co-workers in 2018 prepared insulin loaded chitosan particles by ion gelation method and then coated them on poly (Ɛ-caprolactone) (PCL) which showed complete non-diabetic wound healing in 14 days.[77] In 2018, D.H. Abdelkader and co-workers synthesized insulin-loaded polyvinyl alcohol borate nanoparticles (insulin-PLGA

NP) showed a significant enhancement in wound healing that takes place after treatment.[78] M.C. Ribeiro and co-workers in 2020 used chitosan to form insulin loaded nanoparticles and the observed reduction in inflammation, enhancement in cell proliferation, and wound maturation after treatment in comparison to free insulin.[79]

1.4. Conclusions

Insulin is well known for its antidiabetic activity by regulating blood glucose levels. In addition to that insulin is also a potent inflammatory regulator it inhibits pro-inflammatory signaling and promotes anti-inflammatory signaling which allows it to promote cellular growth. Although in the normal physiologic conditions we do not observe the highly efficient would healing effect of insulin due to inadequate availability of the protein in soluble form. Nanoformulaion may become an effective solution for increasing the insulin concentration at the wound site allowing its enhanced efficacy for healing activity.

CHAPTER-2
MECHANISM OF WOUND HEALING BY INSULIN

2.1. Abstract

In diabetic people with chronically increased free body glucose in their body fluids generally suffer with various problems including retinopathy, neuropathy, arthritis, damaged blood vessels, etc; it also causes a delay in wound healing. Insufficiency of insulin is the main reason for diabetes-I and systemic insulin treatment is a remedy. The perspective of the potential use of insulin to treat chronic wounds in diabetic conditions is focused on in this work (**Figure 4**).

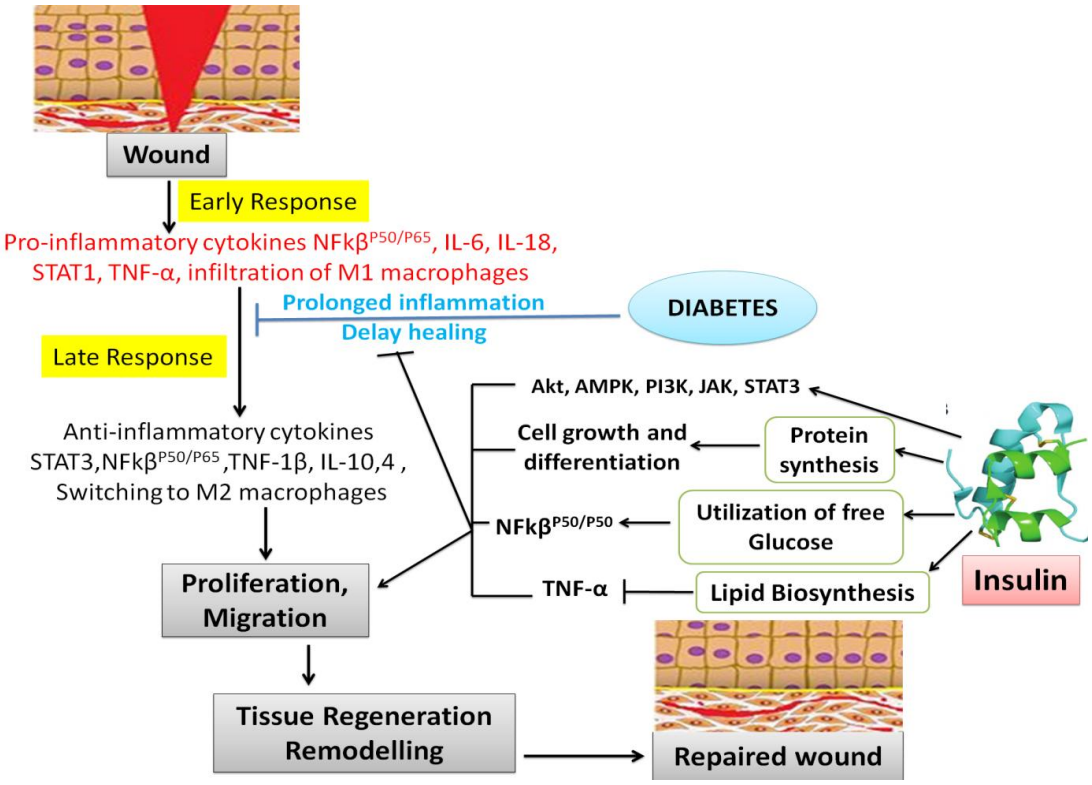

Figure 4: *At the site of the wound the different physiological events take place i.e. inflammation, proliferation, migration, tissue regeneration, and remodeling results in contraction and healing of the wound. Insulin plays a role in anti-inflammation and cell survival through metabolic and synthesis pathways. In the case of diabetes, the inflammatory phase is prolonged and doesn't allow the wound to heal. Insulin through the glucose and fats metabolism leads to the activation of TNF-a and NFkβ respectively which in turn inactivates the inflammatory signaling and helps in cell survival and protein synthesis.*

At the site of the wound, TNF-α, IFN-ϒ, IL-1β, and IL-6 pro-inflammatory cytokines cause the generation of free radicals, leading to inflammation which becomes persistent in

diabetes. Insulin induces expression of IL-4/ IL-13, IL-10 anti-inflammatory cytokines, etc which further down-regulates NFkβ$^{P50/P65}$ assembly. Insulin shifts the equilibrium towards NFkβ$^{P50/P50}$ which leads to down-regulation of inflammatory cytokines such as IL-6, IL-10, etc through STAT6, STAT3, and c-Maf activation causing nullification of an inflammatory condition. Insulin also promotes protein and lipid biosynthesis which indeed promotes wound recovery. Here, in this article, the contributions of insulin in controlling wound tissue microenvironments and remodulation of tissue have been summarised, which may be helpful to develop novel insulin-based formulation(s) for effective treatment of wounds in diabetic conditions.

2.2. Mechanism of wound healing by insulin

Insulin is a peptide hormone, which can also act as an anti-inflammatory agent by activating cytokines which can reduce inflammation and help to recover the wound. Also, through metabolism and synthesis activities, it plays an important role in cell differentiation and survival. Insulin promotes up-regulation of NFkβ$^{P50/P50}$ by suppression of p65 expression and TNF-α. Suppression of NFkβ$^{P50/P65}$ decreases the expression of IL-6, IL-1β, IL-12, and TNF-α cytokines in the wound site.[80-83] Inhibition of proinflammatory cytokines drives the equilibrium toward the expression of anti-inflammatory cytokines, such as IL-10, IL-4, VEGF, etc, which inhibits cellular apoptosis and induces cell proliferation like IGF.[84-86] In the following section the regulation of the dynamics of cytokines under the influence of insulin is discussed under the following sections: a) Insulin inactivated NFkβ$^{p50/p65}$ to decrease inflammation by inducing glucose uptake, b) Insulin induces fatty acid biosynthesis and thereby inactivates the TNF-α mediated inflammatory pathway, c) Insulin induces cell growth and differentiation by protein synthesis and inhibits proteolysis through FOXO inactivation to promote cell survival, d) Insulin behaves as an IGF growth factor and can activate the same signaling pathway to reduce inflammation, and e) Insulin modulates inflammation through the reduction of proinflammatory cytokines and inducing anti-inflammatory cytokines.

2.2.1. Insulin inactivated NFkβ$^{p50/p65}$ to decrease inflammation by inducing glucose uptake

The presence of excess glucose at the site of a wound allows microbial growth, leading to the activation of inflammatory pathways. Insulin is mainly recognized for its anti-glycemic activity. With the help of insulin, glucose molecules get internalized by the cells via glucose

transporters and get stored as glycogen. In muscle tissue, stored glycogen works as an energy source and gets utilized aerobically.[87] Wounds which result from microcirculatory damage mainly in peripheral nerves, the retina, and the renal cortex and, due to increases in oxygen consumption by inflammatory cells, leads to the promotion of glycolytic aerobic to anaerobic switch.[88] The direct consequence of this is the release of lactic acid as an end product of glycolysis. Additional sources of anaerobic glycolysis are the proliferating cells in wound tissues, performing anaerobic respiration in muscles.[88,89] Lactic acid present in the blood gets reused to synthesize glucose in the liver. Lactate dissociates into nicotinamide adenine dinucleotide (NADH) and pyruvate; the NADH formed during this acts as the substrate for nicotinamide adenine dinucleotide phosphate (NADPH) oxidase, results in the production of lactate-induced reactive oxygen species (ROS).[90] Due to the synthesis of more NADPH, the ratio of NADPH to NAD^+ decreases, leading to the activation of VEGF, and facilitation of angiogenesis and pyruvate both together are responsible for the synthesis of collagen and angiogenesis by inactivation of prolyl hydroxylase (PHD) hypoxia-inducible factor (HIF).[91,92]

HIF may cause tissue damage and inflammation at the wound site.[93] Peripheral blood vessel damaged responsive hypoxia causes oxidative stress through activation of NADP oxidase (NOX) at the wound site which is a key regulating factor in the wound healing process and leads to the overexpression of intercellular ROS.[94,95] High levels of ROS, in turn, induces the oxidation of protein and lipid peroxidation leads to cellular apoptosis.[94-97] Further production of ROS induces accumulation of $NFk\beta^{P50/P65}$, which inhibits the expression of HIF1-α and mTOR. Other than inhibition of HIF1 and mTOR, $NFk\beta^{P50/P65}$ induces expression of resistin which is responsible for intercellular insulin resistance.[98,99] Resistin activates a vicious cycle by inducing overexpression of p65.[100] Activation of p65 drives the equilibrium of NFκβ from $NFk\beta^{P50/P50}$ to $NFk\beta^{P50/P65}$ which results in the development of insulin resistance.[98-100] Insulin on the other hand induces HIF1 and mTOR through activation of the AKT pathway and inhibits TNF-α.[101] Activation of HIF1 drives back the NFκβ equilibrium from $NFk\beta^{P50/P65}$ to $NFk\beta^{P50/P50}$. The normalization of blood glucose level with the proper functioning of insulin also effectively reduces the $NFk\beta^{P50/P65}$ expression level.[102] Activation of $NFk\beta^{P50/P50}$ inhibits expression of proinflammatory cytokines like IL-6, IL1β[103,104], and induces overexpression of anti-inflammatory cytokines which results in a decline in inflammatory conditions and promotes tissue repair.[103-106]

NADPH and pyruvate inactivate HIF PHDs, through oxidation of Fe (II) and ascorbic acid. HIF PHDs are dioxygenase, dependent on Fe (II) and 2-oxoglutarate, requiring ascorbic acid. Elsewhere in the presence of lactate, Fe (II) and ascorbic acid are oxidized. As a result

of this, lactate acts as an inhibitor of tissue damage and promotes the release of basal fibroblast growth factor (bFGF), IL-8, and activation of $NFk\beta^{P50/P50}$.[107] The upregulation of $NF\text{-}k\beta^{P50/P50}$ by lactate through suppression of the generation of $NFk\beta^{P50/P65}$ ultimately decreases the release of IL-6, IL-1β, IL-12, and TNF-α. This signaling ultimately leads to an increase in cell viability.[80] In addition, ROS-dependent inhibition of IkBα and expression of VEGF receptors are responsible for collagen synthesis and angiogenesis.[108] IkBα is responsible for the translocation of NFkβ to the nucleus and expression of the p65 gene which in turn induces inflammation.[109,110] In addition to this, suppression of expression of $NFk\beta^{P50/P65}$ takes place by the phosphorylation of ERK through insulin signaling.[111] In contrast to the popular belief on the role of lactate in wound healing, Cheol and his co-workers suggested that lactate, mainly produced in skeletal muscles, either inhibits glucose metabolism by impairing insulin signaling or decreases uptake of glucose by decreasing transmembrane glucose gradient.[112] The insulin signaling for glucose metabolism takes place through 6-phosphofructo-1-kinase (PFK-1), which is produced by fructose-2, 6-biphosphate, and pyruvate dehydrogenase (PDH) used to convert pyruvate to oxaloacetate. Lactate inhibits this insulin signaling by increasing citrate level and decreasing fructose-2, 6-biphosphate which inhibit and promote PFK-1 respectively. Inhibition of PDH by increasing NADH to NAD ratio ultimately inhibits the transformation of pyruvate to oxaloacetate.[112,113] This shows that lactate acts as an inhibitor of glycolysis increasing glucose concentration in blood.[114] A high concentration of glucose in the blood, in turn, leads to prolonged inflammation at the site of the wound.

2.2.2. Insulin induces fatty acid biosynthesis and thereby inactivates the TNF-α mediated inflammatory pathway

Insulin also has several other functions. It stimulates lipogenesis and protein synthesis, as well as cell growth and differentiation.[115] Lipogenesis is a process of synthesizing fatty acid from acetyl-CoA that eventually gets converted to triglycerides.[116] Insulin stimulates lipogenesis by activating two types of enzymes, PDH (pyruvate dehydrogenase) which allows the conversion of pyruvate to acetyl CoA, and acetyl CoA carboxylase which converts acetyl CoA to malonyl CoA. Malonyl CoA provides the 2-carbon building blocks that are used to synthesize the larger fatty acids in the cytoplasm.[117] The transportation of acetyl CoA from the mitochondria to the cytoplasm takes place using the enzyme tricarboxylate translocase, after its conversion to citrate by the reaction with oxaloacetate. Glucose plays an important role in the stimulation of the release of both insulin and citrate.[118,119]

Fatty acids, mainly polyunsaturated ones, play a role in the production of the cell membrane. The composition of the membrane of the cell affects the absorption of the enzymes responsible for the functioning of the cell's phosphatidylinositol 4-kinase (PI4K), a membrane-associated phosphatidylinositol kinase, which plays a central role in cell signaling.[120-122] The products of fat metabolism activate PI4K which regulates the functioning of Protein Kinase C (PKC) which controls the signaling of TNF-α the proinflammatory cytokines.[123] PKC induces inflammation by increasing the expression of p38MAPK and NFkβ. In the presence of PI4K, the activity of PKC inhibited ultimately reduces the release of proinflammatory cytokine TNF-α.[124] The free fatty acid components thus play the role in wound healing.

2.2.3. Insulin induces cell growth and differentiation by protein synthesis and inhibits proteolysis through FOXO inactivation to promote cell survival

The role of insulin in protein synthesis is not very clear. Insulin can stimulate protein synthesis in many types of cells and tissues in various animals including humans. In muscle tissue, insulin induces changes in blood flow and induces increased delivery and uptake of amino acids by muscle tissues which help in muscle anabolism.[125,126] Though, many times it has been found that patient with diabetes-I undergoing systemic insulin uptake loses muscle volume which happens mainly as systemic insulin infusion results in a decrease in the concentration of free amino acids in the blood, which are essential for muscle anabolism.[127] This phenomenon can be overcome by applying exogenous amino acids systematically.[128] Insulin stimulates essential protein synthesis in tissues by increasing the RNA contents and translocation of mRNA mainly through the phosphoinositide-3-kinase (PI3K) pathway of the insulin signaling pathway.[129] In the PI3K pathway, Akt inhibits tuberous sclerosis protein ½ (TSC1/2) that acts as an inhibitor of the mechanistic target of rapamycin (mTOR) which ultimately activates eukaryotic initiation factor (eIF4B) through the phosphorylation of 4E Binding protein (4EBP1). eIF4B binds with the eukaryotic secondary structured mRNA 5'end. During protein synthesis, eIF4B binds to eIF4G and eIF4A, which are further linked with the 40S ribosome and have RNA helicase activity respectively. If insulin is insufficient as in diabetic condition, phosphorylation of 4EBP1 is limited or absent resulting in impaired protein synthesis. Also, the activation of mTOR inhibits proteolysis through MAPox activation.[130-132] Hyperinsulinemia in the muscle also inhibits degradation of protein which results in expansion of the muscle tissue.[133,134] Insulin decreases the concentration of free amino acids in the blood due to inhibition of overall protein degradation in the body.[135] These

roles of insulin in the regulation of amino acid metabolism suggest that insulin can play a very important role in wound recovery in case of diabetic condition where patients are undergoing systemic insulin treatment.

2.2.4. Insulin behaves as an IGF growth factor and can activate the same signaling pathway to reduce inflammation

Insulin-like growth factors (IGFs) are proteins comprised of IGF ligand (IGF-I and IGF-II) that regulate growth and development during embryogenesis, differentiation in adult tissues and has an anti-inflammatory effect. Insulin shows an anti-inflammatory effect via stimulating the release of IL-4/13 and IL-10 (more significantly 100-150%) chemokines and decreasing the release of IFN-ϒ proinflammatory cytokine.[84,135] IGFs bind to the IGF-1 receptor, insulin receptor (IR), insulin-related receptor, IGF-2 receptor, and other receptors. Most functions of both IGF-I and IGF-II are mediated through IGF-Insulin receptor (IGF-IR).[136] IGF-I is an important growth factor produced by fibroblast cells, keratinocytes, macrophages, and platelets. It promotes the migration of endothelial cells into the wound. It also induces the proliferation or mitosis of fibroblast cells for the formation of extracellular matrix and angiogenesis by activating the protein kinase B signaling pathway. In addition, IGF also induces protein synthesis and blocks muscle atrophy to catalyze skeletal hypertrophy.[137]

Upon receptor binding, IGF-I activates insulin receptor substrate 1 (IRS1) which phosphorylates protein kinase B (Akt) via phosphatidylinositol-4, 5-bisphosphate 3-kinase (PI3K). Phosphorylated Akt then activates mTOR, PI3K related kinase which controls cellular proliferation.[138,139] Again IGF-I promotes cellular growth by activating extracellular signal-regulated kinase/mitogen-activated protein kinase/ERK/MAPK pathway via phosphorylation of RAS/RAF kinase.[140] Also, receptor binding of IGF-I leads to the secretion of anti-inflammatory cytokine interleukin-10 (IL-10) which can again activate Akt through AMPK signaling.[81] Similarly, like IL-10, IL-4 also can bind to Akt and helps in the infiltration of M2 macrophages at the wound site.[82,83]

2.2.5. Insulin modulates inflammation through the reduction of proinflammatory cytokines and inducing anti-inflammatory cytokines

Decreased insulin action, either due to insulin resistance or insufficient release of insulin, leads to diabetes. Insulin decreases either due to loss of functions of β-cells, malfunctioning of insulin receptors, or disease in the kidney.[141] Systemic insulin treatment is taken regularly

by 6 million Americans to control hyperglycemic conditions. Hyperglycemia can lead to damage of tissue through oxidative stress by increasing the flux of glucose and other sugars through the polyol pathway, it increases the expression of advanced glycation end products and its activating ligand-receptor, the over activation of hexosamine pathway, and activation of protein kinase. These mechanisms mainly take place through mitochondrial ROS overproduction.[142] In the polyol pathway, more redox stress appears as NADPH consumption in glucose transport remains insufficient to form ROS scavengers i.e. reduced GSH. Formation of the precursors of advanced glycinate product modifies the plasma proteins that bind to the advanced glycination product receptors present on vascular endothelial cells, macrophages, and smooth cells. This activates transcription factor NFkβ, which activates HIF-α to lead to the production of hypoxia stimulated chemokines through the production of ROS.[143] Hyperactivity of protein kinase, in the presence of high glucose, stimulates the eNOS expression in cells of smooth muscles and leads to tissue destruction. Increased ROS production shows the activation of a number of pro-inflammatory pathways and generates epigenetic changes that lead to the persistent expression of proinflammatory genes during wounds. Excessive production of matrix metalloproteinase (MMP-2, 4) impairs wound healing leading to the breakdown of extracellular matrix proteins like fibronectin and vitronectin.[144-146]

In a normal wound, the healing process relies on the activation of a cascade of physiological events such as inflammation, proliferation, epithelisation, vascularisation, maturation, and remodeling at the scar site.[145-147] Macrophages play an important role throughout the whole process. In the early wound healing phase, macrophages function through the release of cytokines and activating leucocytes to produce inflammatory response.[148] Macrophage infiltration takes place into the wound site due to chemotaxis induced by factors such as PDGF, LPS (Lipopolysaccharide), PAMP (Pathogen-associated molecular patterns), Toll-like receptor (TLR) ligand and IFN-gamma (IFN-ϒ).[149,150] M1 are responsible for the secretion of high levels of IFN-β/TNF-α and STAT1. Insulin via PI3/Akt pathway activates STAT3 which inhibits STAT1 synthesis and induces class switching of M1 to M2 macrophages repair macrophages that function in the constructive process like in tissue repair and wound healing. M2 macrophages also produce polyamines and ornithine through the arginase pathway and anti-inflammatory IL-4, IL-10, and IL-13 cytokines.[151,152] Insulin together with M2 macrophages induced anti-inflammatory activates IP3K/Akt pathway to induce protein and fatty acid biosynthesis, cell division, cell migration, and angiogenesis to promote wound recovery.[86,87,150,151] In diabetes with insulin resistance there are consistently

elevated levels of TNFα and IL-6, the proinflammatory cytokines have been shown. In normal glycemic conditions, the adipocytes produce cytokines, like IL-13, that promotes the activation of alternative or M2 macrophages. M2 or activated macrophages are responsible for the secretion of anti-inflammatory cytokines like IL-10 and may secrete insulin-sensitizing factors, PPAR-ϒ (Peroxisome Proliferator-Activated Receptor Gamma), which generates a vicious circle for insulin activity.[152,153] PPAR-ϒ can also activate the anti-inflammatory cytokine IL-10.[154] In the diabetic condition, there is the prolonged-expression of the pro-inflammatory macrophage phenotype sustained by IL-1β and TNF-α, and wound healing gets impaired. Overexpression of IL-1β, TNF-α, or IL-17 cytokines decreases the expression of inflammatory cytokines, upregulates wound healing related genes, and accelerates the healing of wounds.[154-158] Furthermore, adipose tissue and the blood have elevated TNFα cytokines, and TNF-α neutralization improves the sensitivity of insulin in the animals. Diabetes induces changes in gene expression and metabolism in adipocytes and results in increased lipolysis and production of free fatty acids (FFAs) and pro-inflammatory factors that recruit and induce activation of macrophages, such as monocytes chemotactic protein-1 (MCP-1) and tumor necrosis factor α (TNF-α). Activation of M1 macrophages produces a huge concentration of inflammatory cytokines, like IL-1β, resistin, and TNF-α that acts on adipocyte cells to make them insulin resistant. This signaling forms a kind of feedback loop that increases inflammation and resistance to insulin.[159] TNF-α, an inflammatory cytokine, plays an important role in the normal healing process, but its activation for a long period leads to an increase in protease activity. In non-healing wounds of humans, MMPs were detected at very high concentrations. In chronic or inflamed wounds, there is an imbalance in pro-inflammatory cytokines and their inhibitors, proteases, and their anti-proteases expression.[160-163] The transition of macrophages gets delayed in the hyperglycemic condition due to oxidative stress of IL-6, IL-1β, MMPs and ROS, etc cytokines (**Figure 5**).

This delay in transition is responsible for the prolonged inflammatory phase in the case of diabetic wounds and leads to a delay in the wound healing process.[164] The role of insulin in the transition from inflammatory (TNF-α, STAT1, and $NFk\beta^{P50/P65}$, etc) to anti-inflammatory (IL-10, like PKC, HIF-α, STAT3, and $NFk\beta^{P50/P50}$, etc) state is shown in **Figure 6**. The molecular pathway for the transition of M1 macrophages to M2 macrophages in the presence of insulin is depicted in **Figure 7**.[165,166] The transition of M1 macrophages to M2 macrophages is necessary for the healing of the wound.

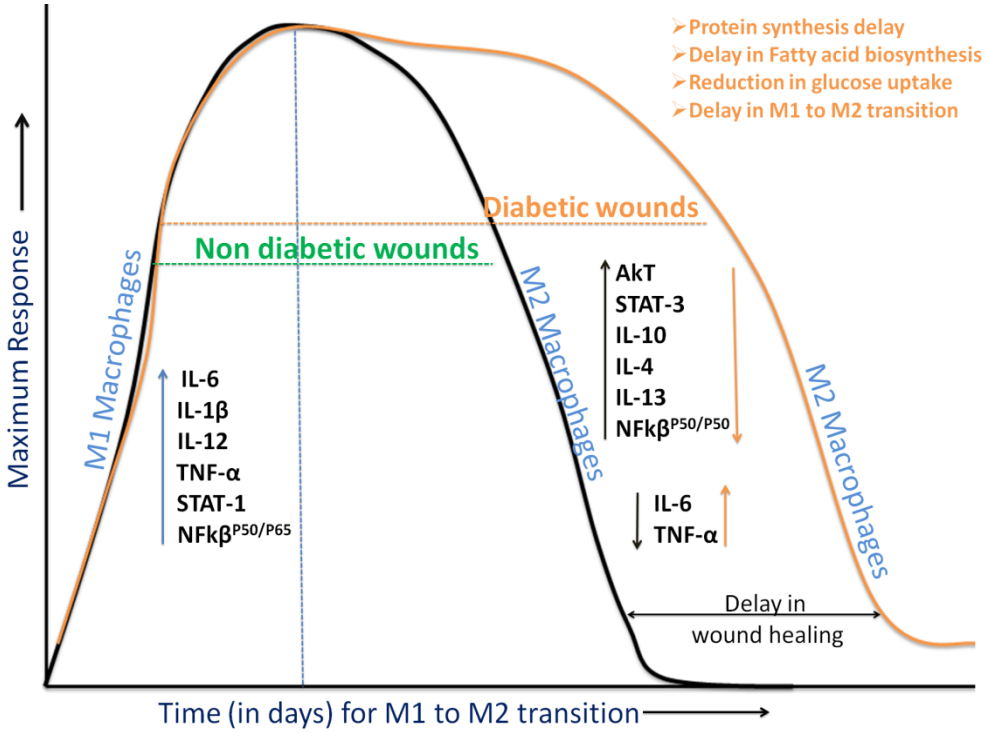

Figure 5: *M1 macrophages, like IL-10, IL-1β, IL-12, TNF-α, STAT1, and NFkβ$^{P50/P65}$, are responsible for inflammation at the wound site. M2 macrophages, like PKC, HIF-α, STAT3, NFkβ$^{P50/P50}$, etc, help in wound recovery by reducing the inflammation.*

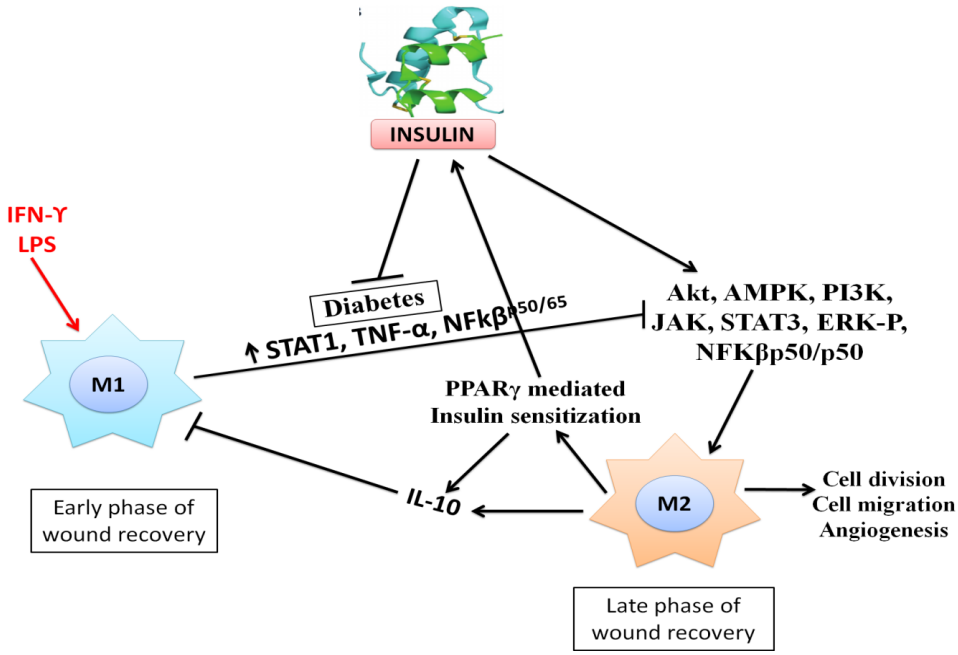

Figure 6: *Effect of insulin of M1 to M2 macrophages transition. In the presence of insulin the expression of M2 macrophages Akt, PI3K, AMPK, PKC, HIF-α, STAT3, NFkβ$^{P50/P50}$, and ERK increases lead to anti-inflammatory response and help in wound recovery.*

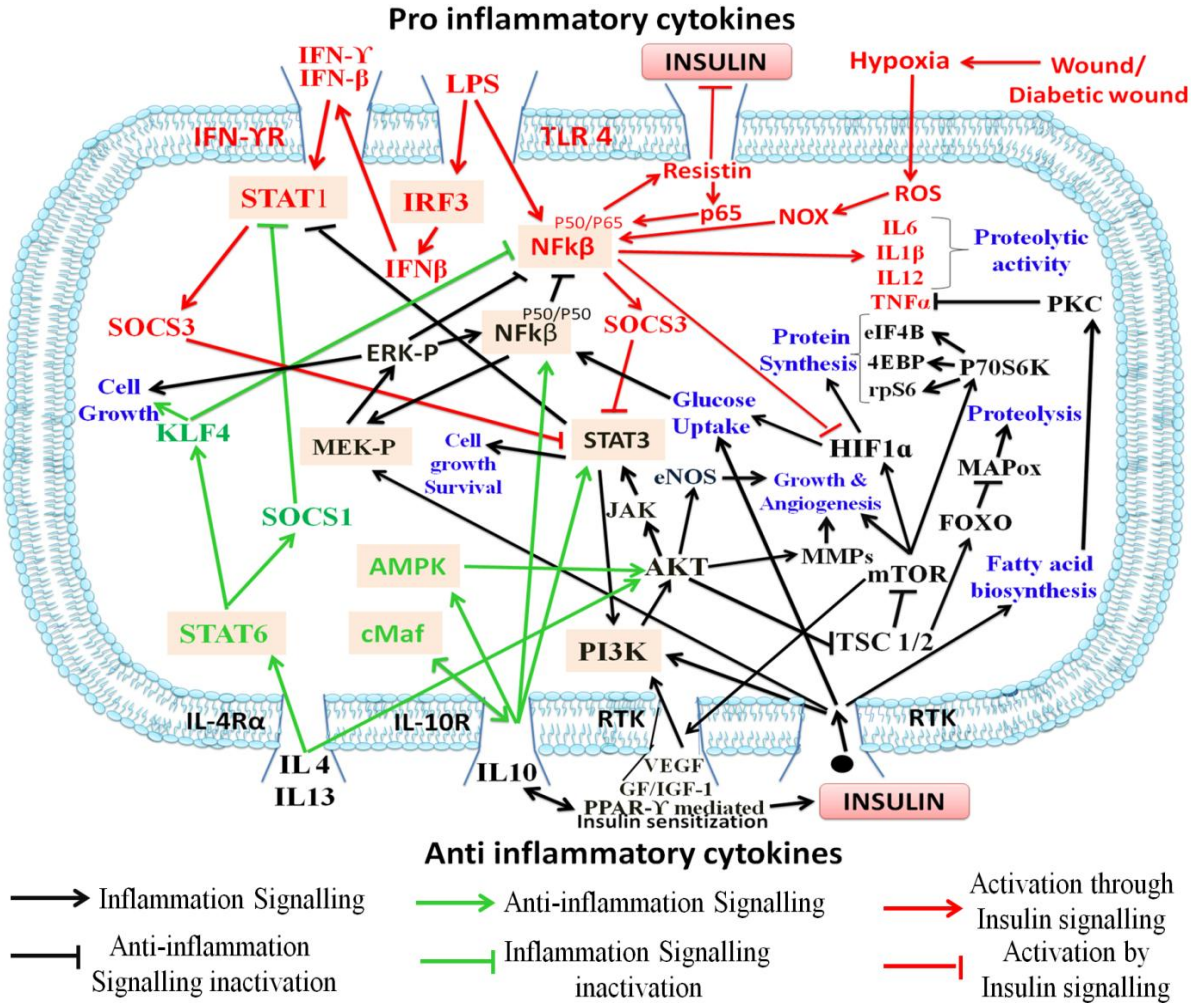

Figure 7: *Molecular pathway for the transition of macrophages i.e. from the M1 to M2 phase. IFN-ϒ and TNF-a generation in wounds activates NFkβ, IRF-3, STAT1 which helps in secretion of IL-10, IL-1β, IL-12, TNF-α, STAT1, and NFkβ$^{P50/P65}$, responsible for inflammation. The transition of M1 to M2 macrophages is necessary for wound healing. IL-4, IL-13, IL-10, IGF, VEGF, and insulin can activate PKC, HIF-α, STAT3, NFkβ$^{P50/P50}$, etc cytokines to produce an anti-inflammatory effect.*

2.2.6. A similar role of C-peptide

C-peptide is a short 31 amino acid peptide, has glycine-rich regions, and acts as a linker between the A and B peptides of proinsulin. C-peptide shows angiogenesis through the ERK1/2 and Akt phosphorylation pathways. This signaling pathway of angiogenesis is similar to the VEGF pathway and ultimately results in the production of NO through eNOS activation. It plays an important role in mitogenesis like insulin, through the same signaling pathway as insulin.[167] C-peptide can bind to the insulin receptor, resulting in the phosphorylation of the intracellular substrate in the Ras/MAPK and the PI3K/Akt signaling

pathways leading to cell division or mitogenesis. In addition to these two functions, C-peptide also shows an anti-inflammatory effect. It shows this activity through the inhibition of the expression of IL-6, IL-8, MIP-1α, and MIP-1β proinflammatory cytokines.[168] C-peptide, like insulin, also prevents complications related to diabetes, like neuropathy, nephropathy, and vascular inflammation, in case of diabetes especially type 1 diabetes mellitus.[169] The blood level of C-peptide also increases during type 2 diabetes, which is due to insulin resistance.[170] During this, endothelial dysfunction gets initiated followed by deposition of C-peptide in the intima of the vessel wall, and leads to increased inflammation in vessels of the aortic arch and atherosclerotic lesions. C-peptide shows this inflammation effect due to its chemotactic behavior towards inflammatory macrophages. Macrophages/T-lymphocytes/monocytes migrate through the vessel wall and release proinflammatory cytokines, IL-6, TNF-α, etc, chemokines and nitric oxide, and activate the intracellular signaling pathway.[171]

2.3. Conclusions

Insulin is a peptide hormone that plays multiple functions in our body such as the control of inflammation, increase in cell differentiation, lipid and protein biosynthesis, etc, in addition to controlling glucose levels in the blood through glucose metabolism. During glucose metabolism, IL-8 and $NFk\beta^{P50/P50}$ get activated causing inactivation of the pro-inflammatory cytokines TNF-α, IFN- ϒ, IL-1β, IL-6 $NFk\beta^{P50/P65}$, NOX, and resistin. Fat metabolism by insulin also inactivates proinflammatory cytokines by inactivating the TNF-α mediated inflammatory pathway. Protein synthesis also gets induced by insulin through the PI3K, Akt pathway which helps in cell survival through the formation of 4EBPI, ribosomal protein S6 (rpS6). This shows that along with anti glycemic activity insulin also exhibits anti-inflammatory action, although the mechanistic aspects of the anti-inflammatory role of insulin remain to be well understood and elucidated. Other than metabolism and biosynthesis pathways, insulin has structural similarities with IGF-I, it can bind to the IGF receptor and show anti-inflammatory activity through PI3K, Akt, etc signaling pathways. Due to structural similarity insulin can bind the IGF receptors and activate the same pathway as GF/IGF-I, necessitating further studies on insulin, IGFs and their role in anti-inflammatory responses (**Figure 8**) About 5% of the world population is diabetic and are at risk of slow recovery/nonrecoverable wound formation. Insulin can promote wound recovery by modulating inflammatory dynamics, therefore novel formulations based on insulin or insulin-like inflammatory modulators (such as IGF) would have a huge potential for the various types

of clinical application including diabetic care, and should be explored for beneficiary purposes.

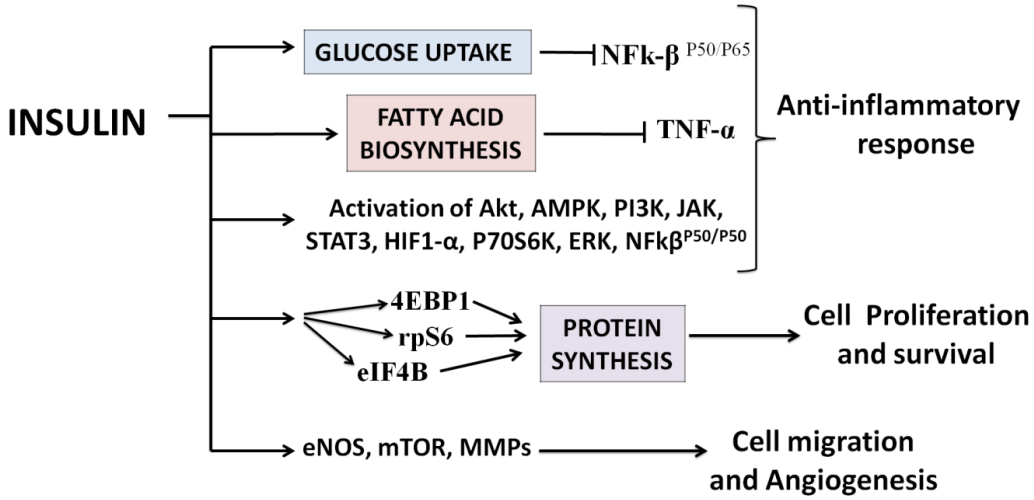

Figure 8: *Insulin plays a role in anti-inflammation and cell survival through metabolic and synthesis pathways. Metabolism of glucose and fats leads to the activation of TNF-a and NFk-β respectively which inactivates the inflammatory signaling. This signaling helps in cell survival and protein synthesis. In addition, insulin can activate the Akt pathway and increase the expression of eNOS, MMPs, mTOR leading to angiogenesis in addition to the anti-inflammatory response. Insulin can also reduce the expression of NFkβ$^{P50/P65}$ through the MEK and ERK pathways such as the glucose uptake pathway.*

CHAPTER 3
INSULIN CAPPED SILVER NANOPARTICLES

3.1. Abstract

The capability of the insulin as a wound healer in normal as well as diabetic condition is merely reported in the literature. In this chapter, we report specific interaction of silver nanoparticles (AgNPs) with insulin by making a ~ 2 nm thick coat around the AgNPs and its potent wound healing efficacy (**Figure 9**). Characterization of the interaction of human insulin with silver nanoparticles showed confirmed alteration of amide-I in insulin whereas amide-II and III remained unaltered. Further, Nanoparticles protein interaction kinetics showed spontaneous interaction at physiological temperature with ΔG, ΔS, E_a, and K_a values -7.48, 0.076, 3.84 Kcal mole^{-1}, and 6 x 10^5 s^{-1} respectively. Insulin loaded AgNPs (IAgNPs) showed significant improvement in healing activity *in vitro* (HEKa cells) and *in vivo* (Wister Rats) in comparison with the control in both normal and diabetic conditions. The underlying mechanism was attributed to a regulation of the balance between pro (IL-6, TNF-α) and anti-inflammatory cytokines (IL-10) at the wound site to promote faster wound remodeling.

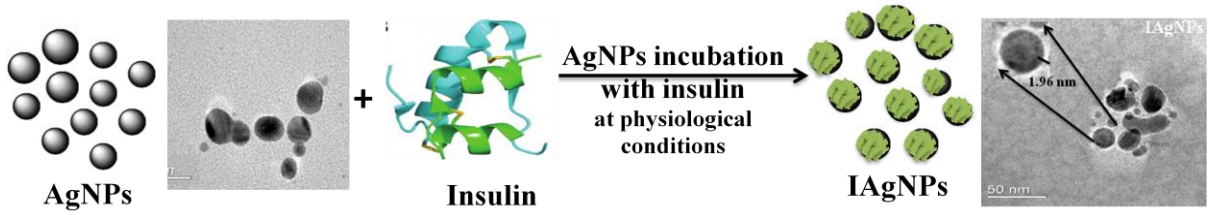

Figure 9: *Schematic representation of insulin silver nanoparticle synthesis (IAgNPs).*

3.2. Introduction

During wound healing inflammation, proliferation and remodeling take place in an orchestrated fashion.[172] Diabetes mellitus, a metabolic disorder, is characterized by loss of insulin functionality that leads to delay in wound healing, a complicated process impeded by various systemic and non-systemic factors.[173,174] Numerous activated dressings have been used to treat the wounds.[18-31] Healing of diabetic wound attained the great attention of investigators but promising therapeutic intervention is still awaited. Insulin is one of the most common and effective therapeutic choices for the treatment of Type-I diabetes. But no report of insulin or other anti-diabetic drugs that either stimulate insulin sensitivity or increase pancreatic insulin release has been reported for their wound healing potential in diabetic conditions.[175-177] A recent report revealed that nanoparticles based insulin delivery enhanced selectivity and sensitivity in comparison to free insulin.[75-78] Present work has emphasized and

investigated the structural changes in human insulin interaction with loosely protected silver nanoparticles (AgNPs). Furthermore, the efficacy of this novel nano-formulation was investigated *in vitro* and *in vivo* for normal and diabetic wound healing activity. The mechanisms of this formulation with respect to inflammatory regulation and wound remodeling were further investigated in laboratory animals.

3.3. Material and methods

3.3.1. Materials

Bovine Serum Albumin (BSA), and molecular biology grade chemicals such as Formaldehyde, Glucose, DMEM-F12 (AL149A (low glucose) and AL219A (high glucose)), 100 X Penicillin-streptomycin mixtures, silver nitrate, Sodium hydroxide, Lead acetate, New born calf serum (RM10437), Phosphate buffered saline pH 7.4 (PBS, TL1099), Ketamine/ Xylazine were purchased from Himedia, India. Rat chows were procured from Ashirwad Industries, Mohali, India. Human recombinant insulin (Huminsulin) was purchased from Eli Lilly and Company Pvt. Ltd., India. *Ocimum tenuiflorum* (Tulsi) leaves were cultivated and harvested from the research field of Thapar University. Human epithelial keratinocyte (HEKa cells, PCS-200-011; ATCC), normal cells were used for *in vitro* studies.

3.3.2. Preparation of silver nanoparticles and insulin protected AgNPs

Aqueous Tulsi (*Ocimum tenuiflorum*) leaf extract (ATE) was prepared by boiling 3 g tulsi leaves in 100 ml water for 2h. After cooling and filtration pH of the solution was adjusted to 7.4 and preserved at 4°C for further experiments. Synthesis of AgNPs was carried out by using ATE as a capping and reducing agent. 240 μM $AgNO_3$ was added in 5000 μl of ATE and was kept under sunlight for 10 min. The color of the solution changed from faint light yellow to brown under the sunlight. After this, AgNPs were incubated with insulin at physiological temperature (37°C) in an incubator for an hour to form insulin protected AgNPs (IAgNPs).

3.3.3. Instrumentation

Surface plasmon of nanoparticles with or without protein was monitored using a UV-Visible spectrophotometer, (JASCO V-630, USA) equipped with Peltier, operated between 600 to 280 nm wavelength ranges at room temperature. Hydrodynamic diameter and stability of bio reduced AgNPs, IAgNPs, and AgNPs + BSA and also IAgNPs + BSA was monitored using Nano book 90 plus, Brookhaven, USA and Malvern v2.3 Zeta potential analyzer, USA. Thermodynamic binding parameters using protein internal fluorescence was studied using

Perkin Elmer PTP-1 LS55 Spectro-fluorometer, and Photon Technology International Fluorescence Spectrophotometer (PTI-FS), equipped with Peltier, USA. To determine the binding affinity of insulin and AgNPs; various particle concentrations of AgNPs (6.2 to 31 pM) were incubated with insulin (5 μM) at different temperatures (37°C, 32°C, and 27°C) and change of Tyrosine intrinsic fluorescence. The inner filter effect was corrected by using equation (i).

$$F_{corr} = F_{max} \text{ antilog } [(A_{ex} + A_{em}) /2] \text{..... (i)}$$

A_{ex} is the absorbance of excitation wavelength (280 nm) and A_{em} is the absorbance at emission wavelength (285 to 350 nm).[178] At different temperatures, Van't Hoff plot, for the analysis of thermodynamic parameters of binding of insulin with AgNPs, ΔG, ΔH, TΔS, and ΔS. The slope of plot ln (K_a) versus 1/Temperature (at 27°C, 32°C, and 37°C) gives ΔH value using Van't Hoff equation (ii).

$$\ln (K_a) = + (\Delta S/R) – (\Delta H/R) \text{..... (ii)}$$

From this plot, −ΔH/R is the slop and ΔS/R is the intercept of the linear fit, from the intercept the enthalpy of the reaction is easily obtained and from equations. (iii) and (iv), Gibbs free energy and entropy were calculated respectively.

$$\Delta G = − RT \ln (K_a) \text{..... (iii)}$$

$$\Delta S = (\Delta H–\Delta G)/T \text{..... (iv)}$$

R is the ideal gas constant. Reaction order and activation energy were determined using the Arrhenius equation (v) by plotting ln K_a versus 1/temperature.

$$\ln K = −E_a/R(1/T) + \ln A \text{..... (v)}$$

Where E_a is the activation energy, K is the rate constant and A is the Arrhenius constant.[179]

Structural changes in insulin protein were observed using Surface-Enhanced Raman Scattering (SERS) spectra (1900-200 cm^{-1}) equipped with laser 785 nm, RamanSys-785Research India. At 37°C thin film of samples ATE control, insulin, AgNPs and IAgNPs were prepared on a glass slide and air-dried. Raman analysis (1900-200 cm^{-1}) was done to check the functional groups and structural motifs involved in interactions. Fourier Transform Infra-Red spectroscopy, 4000-500 cm^{-1} (Cary 680, Agilent, USA) studies were performed using the same samples. The sample pellets were prepared by mixing dried samples with

potassium bromide (KBr). Far Ultra Violet Circular dichroism (Far UV CD) measurements were carried out between the wavelength range from 260 to 200 nm using (model J-815, CD Spectrometer), Jasco, USA performed to identify changes in secondary structures of insulin due to interaction. All the morphological studies like the size of particle and size distribution of the biosynthesized AgNPs and IAgNPs were studied by placing the solution of samples on carbon-coated TEM grids (400 mesh) by using Transmission Electron Microscope (JEOL 2100 TEM), USA. Sodium phosphor tungstate 1% aqueous solution of pH 6 was used for preparing the grids.

3.3.4. Stoichiometry ratio of AgNPs: insulin binding

The stoichiometry ratio was determined by the Bradford protein assay in comparison with BSA standard curve. A different concentration (150 μM to 15 mM) of insulin was incubated at the physiological condition with AgNPs 1.25 nM. After incubation, the samples were centrifuged at 12,000 × g for 10 min, thereafter samples both pellet (bound) and supernatant (unbound) were estimated with Bradford reagent using equation (vi) and (vii).

Amount of total bound protein = OD of control (Y) - OD supernatant (Z) ..... (vi)

$$\text{Number of protein bound to a single AgNP} = \frac{\text{Average number of bound proteins per ml}}{\text{The average number of AgNPs per ml}} \quad \text{.....(vii)}$$

3.3.5. *In vitro* studies

3.3.5.1. Effect of IAgNPs on wound recovery

Microscopy of the biological sample carried by inverted microscope (Cosmo laboratory equipment, Ambala, India). The absorbance of immunological samples was measured by Erba Lisa Scan EM, Transasia Bio-Medicals Ltd. India. Human epidermal keratinocyte cells (HEKa) were cultured at 37°C and 5% CO_2 in DMEM F12 with 10% serum in presence of various glucose concentrations (100, 180, and 360 mg/dl). After 90%-95% confluence, wounds were generated by the scratch method and supplemented with 0 pM, 3 pM, and 60 pM of IAgNPs. Wound diameters were measured at 0h, 12h, and 24h.

3.3.6. *In vivo studies*

An *in vivo* experiment was performed by using Wistar rats and wound healing, anti-inflammatory, and histological changes were observed after treatment with IAgNPs.

3.3.6.1. Animal maintenance and induction of diabetes mellitus

10 week old male Wistar rats (200-220 g) were obtained from the animal house Department of Pharmacy, Amity University, Noida for the study. Animals were cared for and studied as per the standards of CPCSEA, New Delhi, Govt of India and approved protocol of institutional animal ethical committee (Approval Number: CPCSEA/IAEC/AIP/2016/04/13). During the protocol, animals were maintained on a normal day and night cycle in an institutional animal house (temp 20 ± 2°C, relative humidity 60% ± 10%). All animals were provided with food and water *adlibitum*. Diabetes mellitus was induced by a single intraperitoneal injection of Streptozotocin (STZ, 55 mg/kg/once/i.p) dissolved in freshly prepared citrate buffer (pH 4.5).[180]

3.3.6.2. Full-thickness dermal excisional wound formation

First Animals were anesthetized by intraperitoneal administration of ketamine and xylazine (80 mg/kg, 10 mg/kg).[181] Thereafter dorsal area of rats was shaved and rinsed with 10% povidone-iodine solution. Aseptically a round wound of 15 mm diameter was created in the interscapular region of the dorsal part of each animal. Epilated wound areas were then exposed with semi-occlusive nonwoven polyester dressing with a splint.

3.3.6.3. Experimental design of animal experiment

Animals were randomly divided into two groups namely nondiabetic (Group-1) and diabetic (Group-2). Each group was further divided into 4 sub-groups including control, AgNPs, ATE-Insulin, and IAgNPs treatment (A-D), with 6 rats in each. Thereafter animals were treated with topical application of different nano-formulations in combination with Carbapol-980 based gel. Subgroup A received 50 µl saline with Carbapol-980 gel (0.5 mg) topically at the wound site. Subgroup B, C, and D received topical application of Carbapol-980 gel (0.5 mg) along with AgNPs, ATE-Insulin, IAgNPs (50 µl) respectively. Biochemical and histological assays were performed on the 5^{th} and 11^{th} day respectively. The elaborate design of the experiment is presented in **Figure 10**.

Estimation of the epithelization period (EP) Wound diameter of all animals was measured using Vernier caliper on alternate days until complete healing of wound for all sets of animals. EP was measured by calculating the rate of wound contraction. The percentage of wound contraction is expressed as below in equation (viii).

$$\%\text{Wound contraction} = \frac{\text{(Initial wound area - wound area at specific day)}}{\text{Initial wound area}} \times 100 \quad \text{..... (viii)}$$

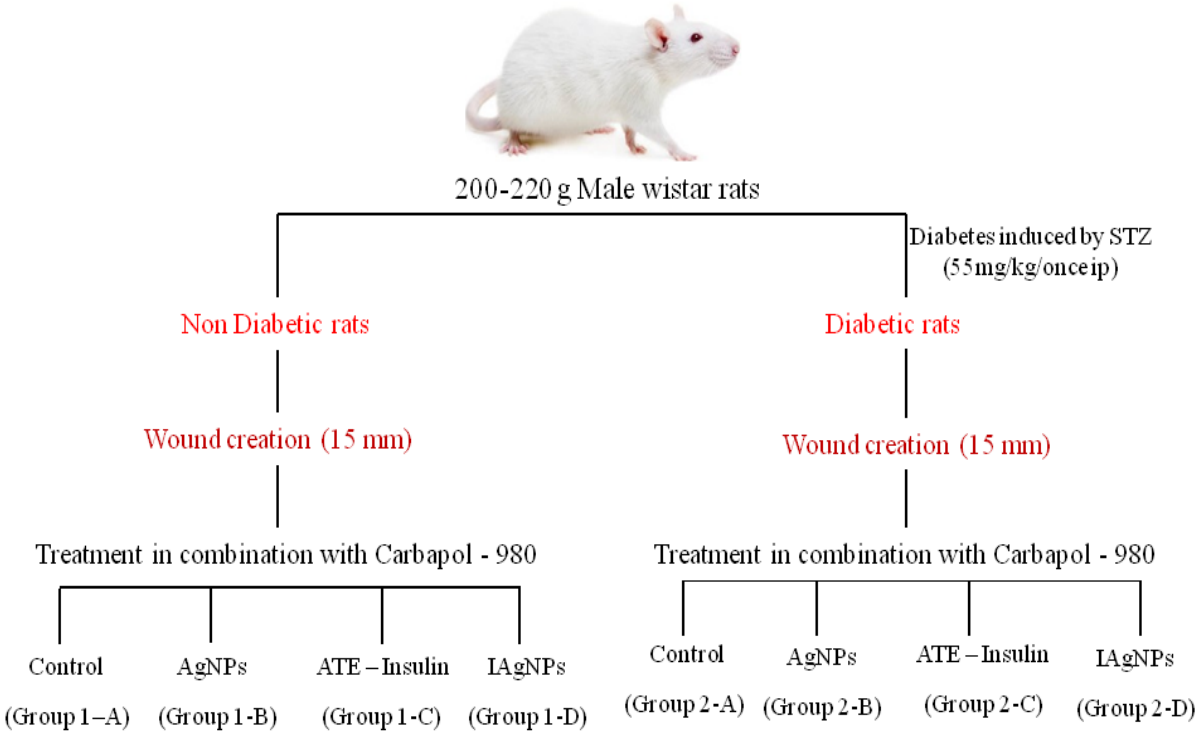

Figure 10: *Male Wistar Rats were divided into two groups including non-diabetic and diabetic rats. These two groups were further divided into 4 sub-groups having control, AgNPs, ATE-insulin, and IAgNPs treatment.*

3.3.6.3.1. Preparation of carbopol 940 loaded nano gel

Carbopol 940 (1.5 g) was soaked overnight with distilled water (25 g) in the refrigerator. Polyethylene glycol (PEG) 400 (2.5 g) was added and mixed. Methylparaben (MP) 0.15 g, propylparaben (PP) 0.03 g, and menthol (2 g) was dissolved in propylene glycol (PG) 2.01 and added to the mixture. Finally, the drug was dispersed in remaining distilled water and added to the gel mixture. Volume was makeup to 50 g and few drops of triethanolamine were added to increase the pH and viscosity of the gel.

3.3.6.3.2. DSC (Differential Scanning Calorimetry)

The required amount of sample (ATE-insulin, IAgNPs, and IAgNPs + Carbopol 940) were taken and placed in a DSC aluminum pan. The prepared samples were evaluated by heating within the range of 40 to 400°C at the rate of 10°C with nitrogen at 2 bar pressure.

3.3.6.3.3. Visual evaluation of nano gel

The physical appearance of nano-formulation containing gel was checked.

3.3.6.3.4. pH determination

The pH of all the nano-gel formulation was also checked.

3.3.6.3.5. Viscosity study

The viscosity of nano gel was determined by using a Brookfield viscometer. 1gm of nano gel was taken in a tube; 10ml of distilled water was added to it and stored overnight. The resulting gel mixture was mixed to an obtained homogenous mixture. The viscosity of nanogel was determined by Brookfield viscometer (model LV DV-II + Pro) using spindle number S64 at 0.5, 1, 2.5, 5, 10, 20, 30, 50, 60, and 100 rpm with increasing then decreasing rpm. Viscosity was measured at 27.7°C. Flow index and Consistency index is determined by using the equation (ix):

$$\tau = Kr^n \text{ ..... (ix)}$$

Taking log on both sides

$$log\tau = logK + nlogR \text{ ..... (x)}$$

Where "τ" is shear stress; "r" is the shear rate; "K" is consistency index; "n" is flow index in equation (x).

3.3.6.3.6. Spreadability test

Nanogel (0.5 g) was placed within a circle of 1 cm diameter on a glass plate over which a second glass plate was placed. A weight of 500 g was allowed to rest on the upper glass plate.

3.3.6.3.7. Histological assessment

Three rats from each group were sacrificed on the 5^{th} and 11^{th} day and wound skin was used for histological studies. Sections were screened for hematoxylin and eosin staining; re-epithelisation, polymorphonuclear leucocytes (PMNL), fibroblasts, and collagen formation in wound skin samples were assessed under a light microscope.[182]

3.3.6.3.8. Estimation of inflammatory cytokines

At the site balance of pro and anti-inflammatory cytokines determines the wound recovery rate. Pro-inflammatory (IL-6, and TNF-α) and anti-inflammatory (IL-10) cytokines were estimated from rat serum samples on the 5^{th} and 11^{th} day by enzyme-linked immunosorbent assay (sandwiched ELISA kit, Ray Biotech, USA) following manufacturer's protocol.

3.4. Statistical analysis

Data were presented as the mean ± SD of at least three independent experiments. By using one-way ANOVA analysis of data was carried out. Then the corresponding *P*-value was measured to check the statistical significance of the data.

3.5. Structural changes in nanoscale due to insulin - AgNP interaction

Sharp absorption single surface plasmon resonance peak at 352 nm (**Figure 11A**) was observed due to the reduction of silver nitrate using ATE under sunlight.

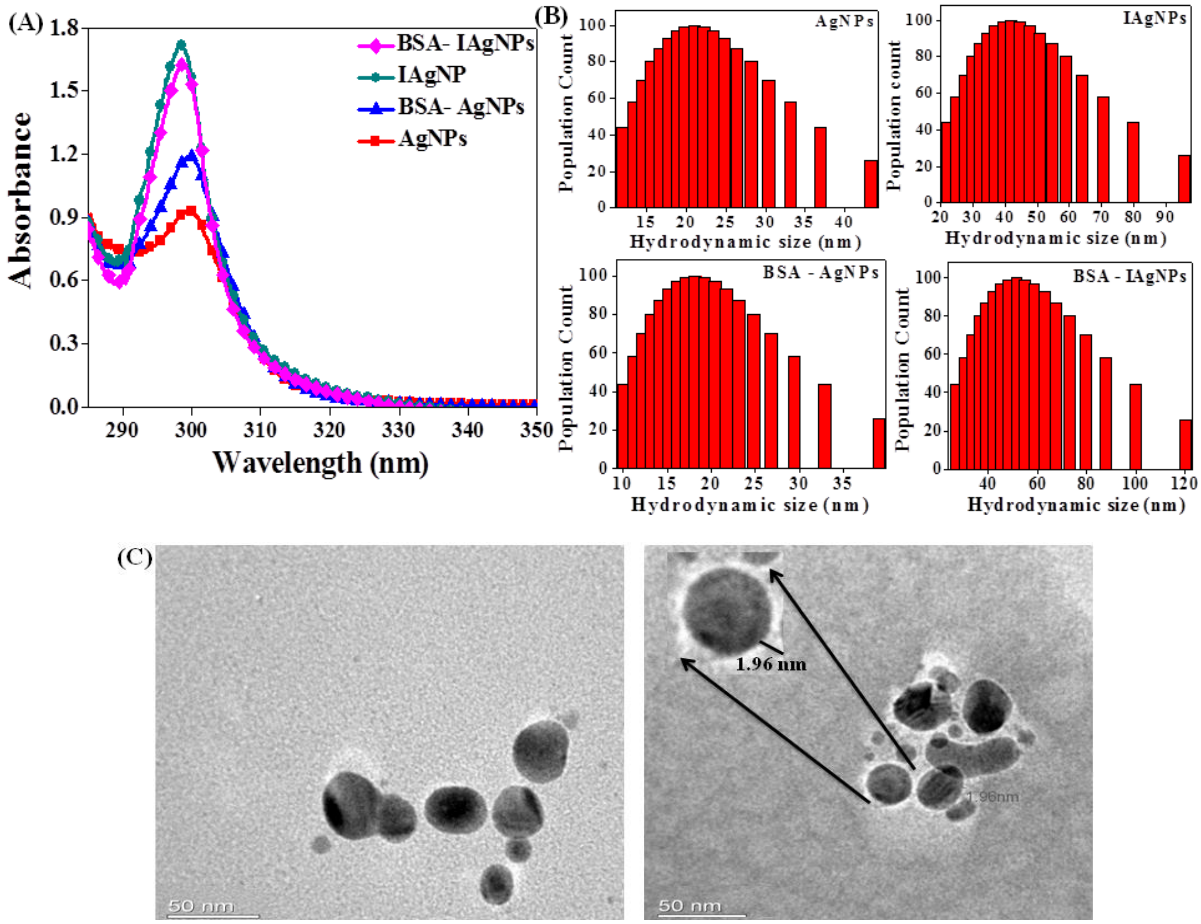

Figure 11: *Study of specificity of interaction of insulin and AgNPs using UV-Visible Absorption spectra of* (A) *AgNPs, IAgNPs, and control protein i.e. BSA, DLS spectra showing the hydrodynamic radius of* (B) *AgNPs, IAgNPs, AgNPs with BSA and AgNPs with BSA and Insulin. TEM of* (C) *AgNPs and IAgNPs show AgNP is of size around 22 ± 2 nm and with insulin protein the coating is approximately 1.96 ± 0.1 nm. Scale bar 50 nm.*

Upon incubation, with insulin 3 nm blue shift with almost double the intensity was observed and λmax was obtained at 349 nm (**Figure 11A**) due to the formation of mono-dispersed IAgNPs. No significant changes in SPR were observed after incubation of AgNPs with BSA, as control (**Figure 11A**). Even no further changes in SPR have been observed in

the case of BSA incubated with preformed IAgNPs suggesting specificity of interaction of insulin and AgNPs (**Figure 11A**). The hypothesis of interaction specificity was further supported by DLS (**Figure 11B**). The hydrodynamic diameter approximately 22 ± 2 nm and 42 ± 2 nm was observed for bio-reduced AgNPs and IAgNPs respectively (**Figure 11B**). Whereas there are no significant changes in hydrodynamic diameter was observed due to incubation of AgNPs or IAgNPs with BSA (**Figure 11B**). The zeta potential studies showed an increase in potential value from -12.4 mV to -15.1 mV due to the formation of IAgNPs from AgNPs. The shape, size, and diameter of the insulin capping on AgNP was further confirmed by TEM studies. TEM micrographs suggest that both AgNPs and IAgNPs are spherical. AgNPs have size ranges between 20 ± 4 nm, further it received a cap of 2 ± 0.5 nm when coated with insulin (IAgNPs) (**Figure 11C**). The Bradford assay shows that the average 475 ± 15 insulin proteins bind with a single AgNP.

3.6. Conformational changes at the protein level due to insulin-AgNPs interaction

To determine the structural changes in protein level spectroscopic studies involving CD, FTIR and Raman were performed. In CD studies around 13% increase in ellipticity was observed in the between case 205 to 215 nm of insulin due to interaction with AgNPs (**Figure 12A**) whereas no significant changes were observed in the case of control serum proteins (BSA) suggesting specificity of insulin-AgNPs interaction (**Figure 12B**).[180] The conformational changes also observed using FTIR and Raman spectroscopy.

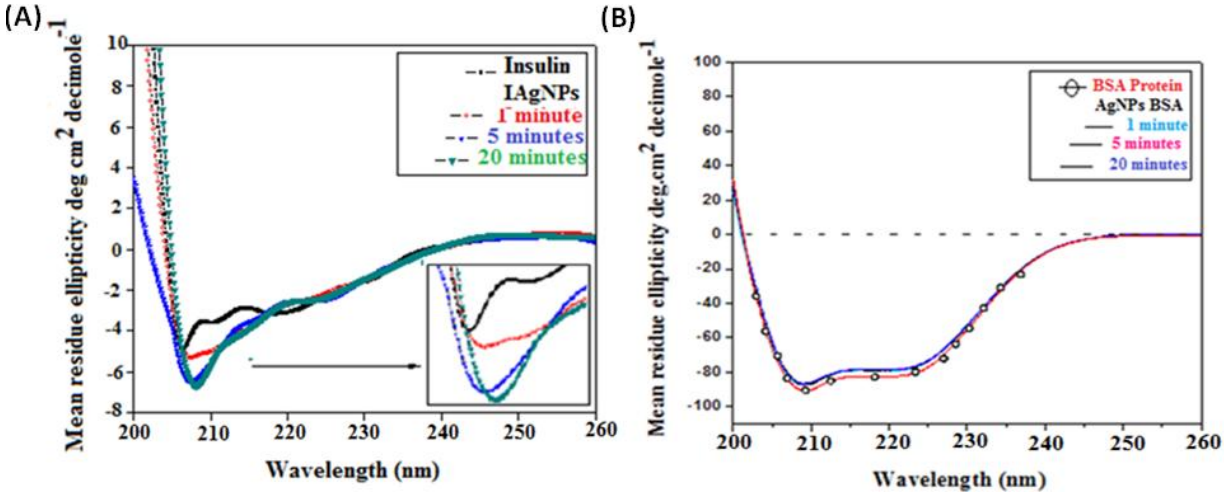

Figure 12: *UV-CD spectra of* (A) *Insulin with AgNPs &* (B) *BSA with AgNPs (20-minute incubation) show secondary structure changes.*

FTIR spectra of IAgNPs showed a shift in prominent transmission peak of insulin form 2939 cm^{-1} to 2886 cm^{-1}, responsible for amide-B stretching (Aliphatic C-H stretch) (**Figure**

13A).[183,184] Amide-I due to C-O stretch shifts in insulin from higher wave number 1658 cm^{-1} to 1653 cm^{-1} in IAgNPs.[185] In insulin amide-II at 1539 cm^{-1} appears at 1546 cm^{-1} in IAgNPs due to the changes in N-H bending and C-N stretching, and the most prominent peak of an amide-III functional group at 1236 cm^{-1}, which differ from control insulin at 1228 cm^{-1}, and also C-N weak stretch broadband present in insulin but show peaks at 1111 in AgNPs.[185-187] Amide-A broadband at 3397 cm^{-1} is present only in IAgNPs and AgNPs at 3428 cm^{-1} which is absent in insulin.[188] Similarly, Prominent peaks of C=S at 550 cm^{-1} and C-S at 682 cm^{-1} in IAgNPs and unlike broadband in insulin indicates its involvement in insulin AgNP interaction.[189] Vibrational changes between AgNPs and IAgNPs observed during FTIR studies are also compared and is represented in (**Figure 13A**). In comparison with AgNPs, the peak of amide-A appears at 3428 cm^{-1} which is at 3397 cm^{-1} higher wavelength in IAgNPs but absent in case of insulin.[188] Peaks of C-H stretch are at 2909 cm^{-1} in AgNPs but in IAgNPs at 2939 cm^{-1}.[183,184] Other shift observed during FTIR studies were from 1458 cm^{-1} of insulin to 1049 cm^{-1} in IAgNPs other 2844 cm^{-1} in AgNPs to 2886 cm^{-1} in IAgNPs.

Raman spectral analysis showed in **Figure 13B-E**. In insulin amide-I, C-H (bend), C-S, and S-S bond. C-O-C peak position shifts from 357 to 361 cm^{-1} in IAgNPs.[190] Amide-I peak of insulin at 1655 cm^{-1} shift towards higher wavelength 1666 cm^{-1} after binding of insulin with AgNPs.[191] Peaks at 1516 and 1519 cm^{-1} of insulin due to C-C stretch clubbed together at 1508 cm^{-1}.[190] Further C-H bend shows slight changes from 1359 similarly peak at 1310 cm^{-1} responsible amide-III (random coils) in insulin shows a slight shift to 1331 cm^{-1} in insulin to 1316 cm^{-1} after interaction with AgNPs.[192] The peaks responsible for amide-III (α-helix) bond at 1256 cm^{-1} in insulin showed a stokes shift towards lower wave number 1254 cm^{-1} due to interaction with AgNPs.[190] The peak of C-S (stretch) shifts at 725 cm^{-1} in IAgNPs. A similar shift of peak position was observed in the case of S-S from 538 cm^{-1} (in free insulin) to 541 cm^{-1} in IAgNPs.[190] The peaks at 1710, 1449, 936, and 763 cm^{-1} responsible for C=O (stretch), amide-II, C-O-C, and O-C-N (bend) functional group vibrations remain unaltered.[193] The stoke shift towards lower wave number of insulin peak at 1529 cm^{-1} to 1525 cm^{-1} after AgNPs addition responsible for C-C (stretch). Formation of the sharp peak at 294 cm^{-1} responsible for Ag-S interaction was observed suggesting a strong interaction of insulin with AgNPs.[194] C–C (bending) peaks shifted from 226 cm^{-1} of insulin to 223 cm^{-1} after its interaction with AgNPs.[191] Also Peaks of C-O-C at 357 cm^{-1} in AgNPs but 361 cm^{-1} in IAgNPs.[189] Similarly, IAgNPs shows vibrational peak shifts in comparison to AgNPs, C-C bend at 223 cm^{-1} in IAgNPs but at 220 cm^{-1} in AgNPs.[191] Some vibrational peaks are present in IAgNPs but not in AgNP, IAgNPs show some vibrational peaks of the C-S bond at 711 and 718 cm^{-1} but

absent in AgNPs.[192] The spectral changes data after the interaction of insulin with AgNPs are represented in tabular form in **Table 1**.

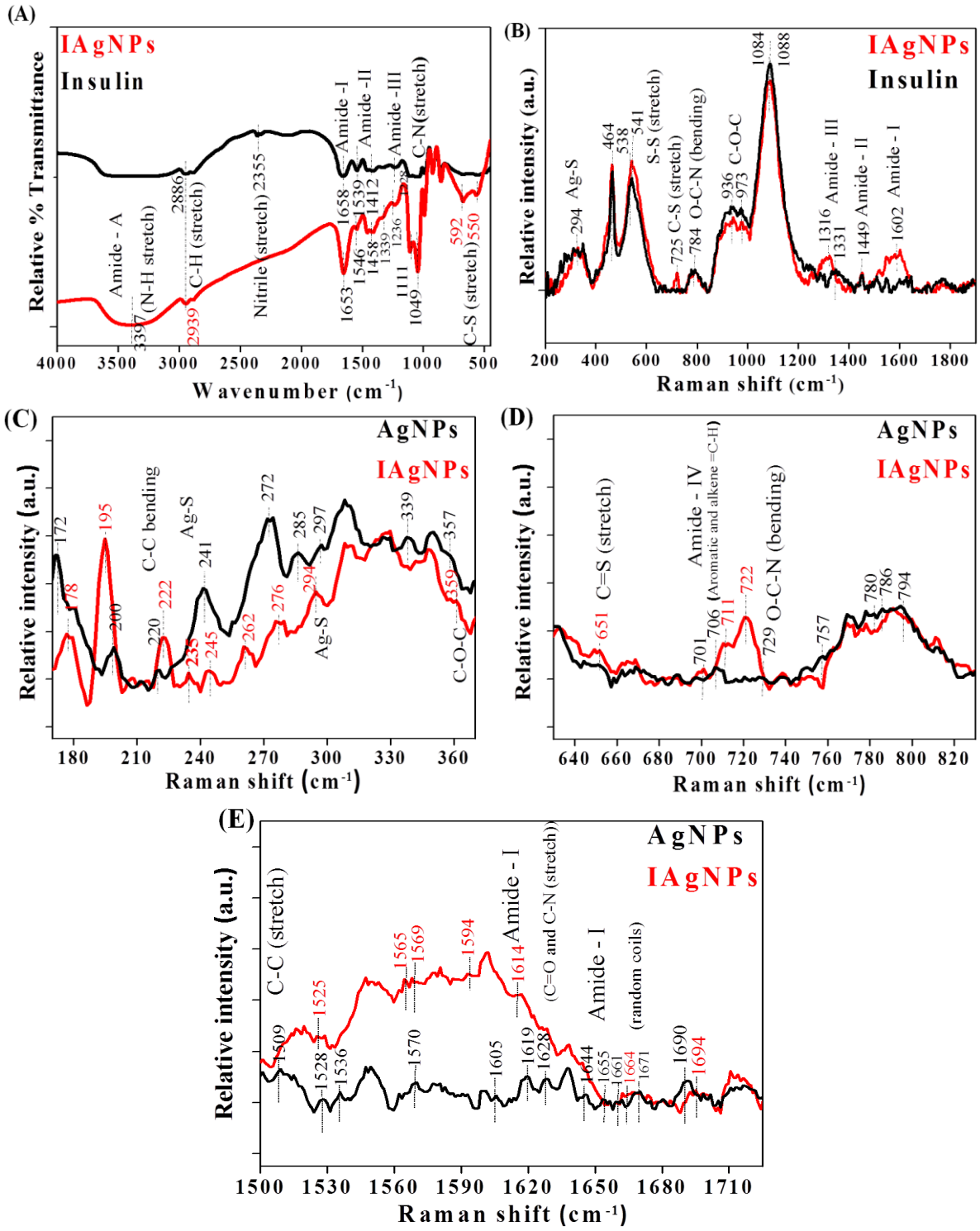

Figure 13: *AgNPs and insulin show different functional group are involved in adsorption on insulin on silver nanoparticles. FTIR spectra* (A) *4000-450 cm*$^{-1}$*and Raman spectra of* (B) *200–1800 cm*$^{-1}$, (C) *170-370 cm*$^{-1}$, (D) *630-830 cm*$^{-1}$, *and* (E) *1500-1720 cm*$^{-1}$.

Table 1: *Comparative table of Raman and FTIR spectra of IAgNPs and insulin showing changes in the Raman shift and wavenumber (cm^{-1}) after insulin interaction with AgNPs.*

Raman shift (cm^{-1})			**Wavenumber (cm^{-1})**		
Functional groups	**IAgNPs**	**Insulin**	**Functional groups**	**IAgNPs**	**Insulin**
C=O (stretch)	1710	1710	**Amide - A**	3397	-
Amide - I	1602	1605	**Amide – B (C-H stretch)**	2939	2886
C-C (stretch)	1509 1525	1528	**Nitrile (stretch)**	-	2355
Amide - II	1449	1449	**Amide - I**	1653	1658
C-H (bend)	1359	1360	**Amide - II**	1546	1539
Amide – III (random coils)	1316	1331	**Amide - III**	1236	1228
Amide – III (α – helix)	1256	1254	**C-N (weak stretch)**	1111	-
C-O-C	936	936	**C-S (stretch)**	Broad band	592
O-C-N (bend)	763	763	**C-S (stretch)**	,,	550
C-S (stretch)	725	-	**Other peaks**	1458	1412 1399 1049
S-S (stretch)	538	541			
Ag-S	294	-			
C-C (bending)	226	223			
Other peaks	1610, 1610 1386, 1395 1293 668, 672, 642,357,318	1607, 1614 1380, 1390 1294 663, 648 361, 308 223, 243			

The internal fluorescence of insulin was monitored from 300 nm to 400 nm after excitation at 280 nm. Almost 20% decrease of intrinsic fluorescence was observed which came to saturation within 20 minutes of incubation. Detailed procedure and obtained Scatchard plot at various temperatures are presented in **Figure 14A**, **B**, **C**, **D**, **E**, and **F**. At 27°C (**Figure 14D**), 32°C (**Figure 14E**) and 37°C (**Figure 14F**) temperatures the calculated association rate constant was (K_a) 33.1126, 68.0272 and 70.4225 µM and dissociation rate constant (K_d) were 0.0302, 0.0147 and 0.0142 µM respectively. These results indicate that the stability of interaction increases with an increase in temperature.

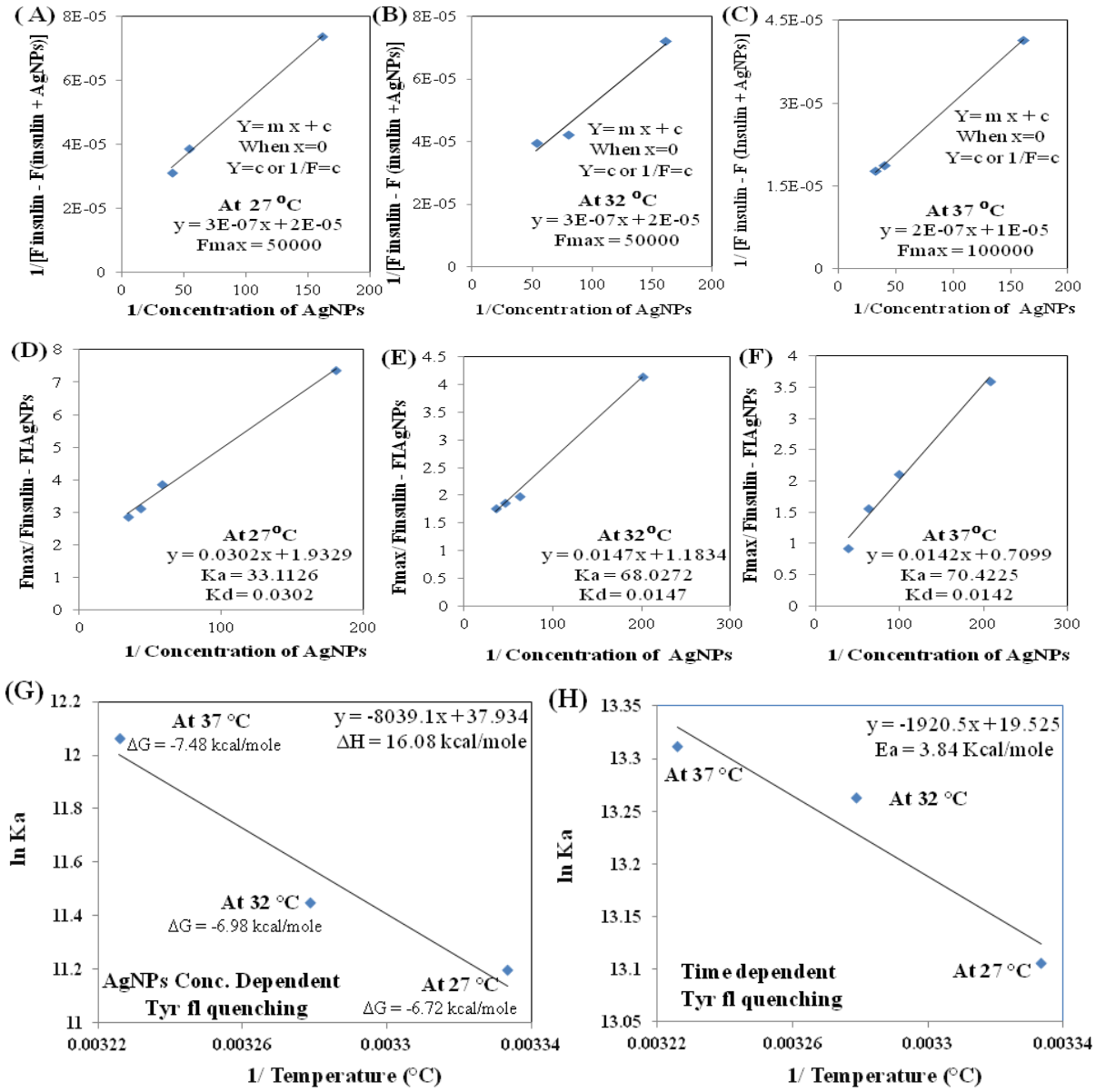

Figure 14: *Tyrosine internal fluorescence quenching studies to determine the binding parameters. Van't Hoff plot at different temperatures* (A) *27°C,* (B) *32°C, and* (C) *37°C to calculate thermodynamic parameters. Scattered Plots of quenching of fluorescence of*

tyrosine amino acid present in insulin, (D) *at 27°C, &* (E) *at 32°C,* (F) *37°C and to find out* F_{max}*,* K_a*, and* K_d *(R = Binding sites occupied by Ligand and Lf = Free ligand).* (G) & (H) *Arrhenius plot to find Activation energy.*

The plot of ln K_a versus 1/T gives ΔH value is 16.08 kcal mole-1 (ΔH>0) shows that the net enthalpy change is positive and insulin-AgNPs interaction is endothermic. Calculated ΔG values were -6.72, -6.98, and -7.48 kcal $mole^{-1}$ at 27°C, 32°C, and 37°C temperatures respectively which indicates the forward reaction was favorable and at the physiological temperature, it attends the highest affinity (**Figure 14G**). The calculated ΔS value was 0.076 kcal $mole^{-1}$ K^{-1} showed that the reaction was entropically driven and a positive value indicates that the solvation entropy was favorable. The time-dependent insulin fluorescence quenching indicated the reactions were of first order with rate constant 604500, 576000, and 492000 s^{-1} at 37°C, 32°C, and 27°C respectively and the E_a was 3.84 kcal $mole^{-1}$ (**Figure 14H**) showed the reaction was endothermic as shown by the ΔH value. The tabular form of the thermodynamic values is represented in **Table 2**.

Table 2: *Tabulation of the thermodynamic parameters at different temperatures (37°C, 32°C, and 27°C) was observed using the van't Hoff and Arrhenius plot.*

Temp (°C)	**Fmax (10^4)**	**Ka (μM)**	**Kd (μM)**	**ΔG (Kcal/mol)**	**TΔS (Kcal/mol)**	**ΔS (Kcal/mol. K)**	**ΔH (Kcal/mol)**
27	5	33.1126	0.0302	-7.48	23.56	0.076	16.08
32	5	68.0272	0.0147	-6.98	23.1	0.076	16.08
37	10	70.4225	0.0142	-6.72	22.8	0.0759	16.08

3.7. *In vitro* cell migration assay

IAgNPs induced higher HEKa cell migration in comparison to control in experimental sets containing glucose concentration 100, 180, and 360 mg/dl. The extent of migration increased with the increase of time and IAgNPs concentration (**Figure 15A**). After 24h, IAgNPs treated HEKa cells (**Figure 15B**) for normal glycemic (100 mg/dl) and moderate hyperglycaemic conditions (180 mg/dl) showed an increased migration of almost 25% and 27% respectively (**Figure 15C**) whereas 360 mg/dl glucose concentration (**Figure 15C**) showed almost 31% faster cell migration compared to vehicle-treated control, indicating higher wound healing

activity in higher hyperglycaemic condition. The statistical significance of the data shown with "*": ** P<0.001, ** P<0.01, and * P<0.05.

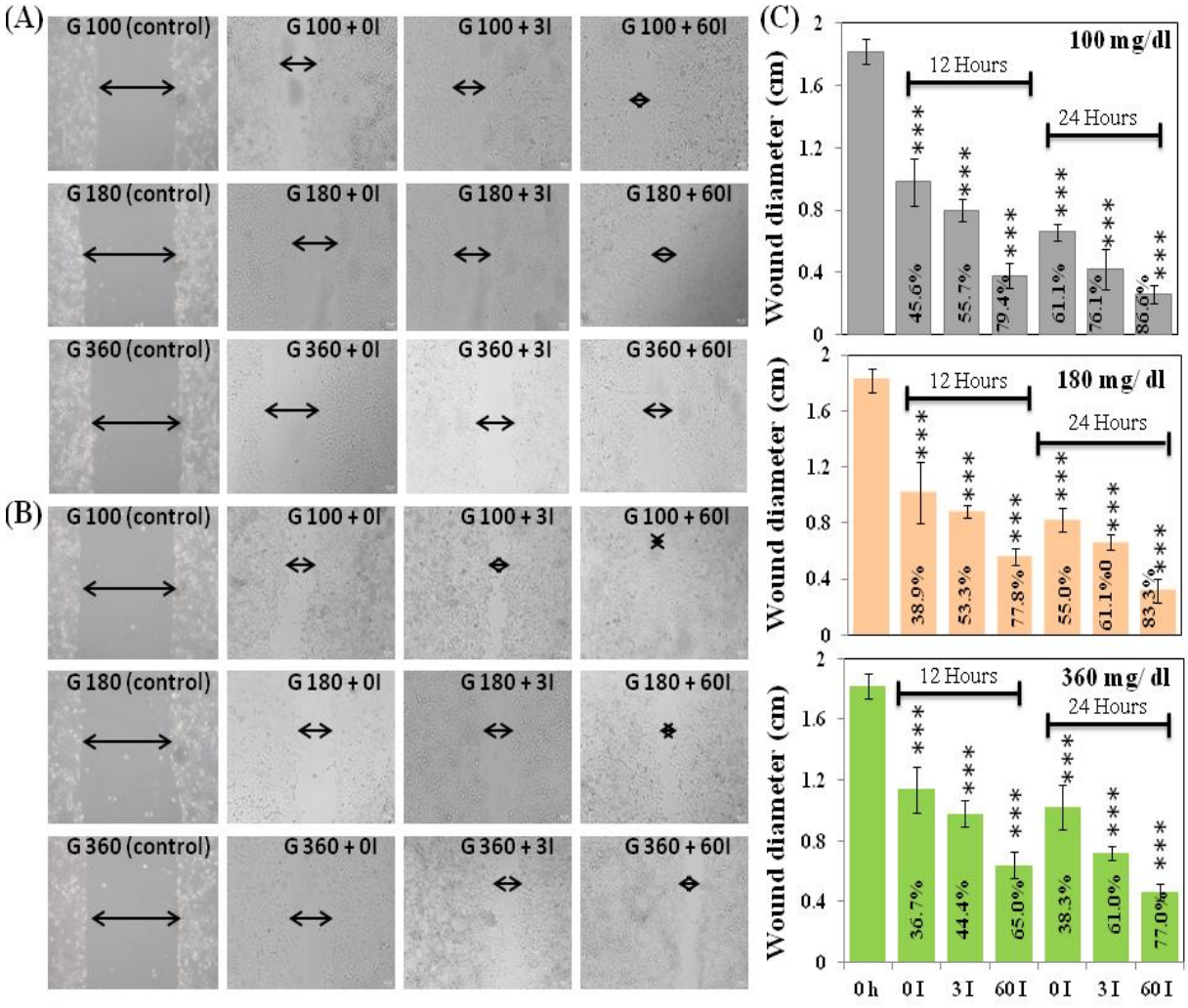

Figure 15: *HEKa epithelial cell migration* (A) *after 12h &* (B) *24h and Bar graphs* (C) *showing cell migration (in cm) at 12h and 24h with different Glucose and IAgNPs concentration (G = Glucose in mg/dl and I = Molar Concentration of IAgNPs in pM). The statistical significance of the data shown with "*": *** P<0.001, ** P<0.01, and * P<0.05.*

3.8. DSC (Differential Scanning Calorimetry)

The DSC thermogram of ATE-Insulin shows the peak in the region of 50-70°C. For sample B, the DSC thermogram shows three distinct peaks in the region of 50-70°C and 100-150°C. In thermogram B the first peak from the left corresponds to the peak of insulin. The rest of the two peaks were obtained due to the formation of IAgNPs. In DSC thermogram C there was no new peaks were found that indicate that sample consisting of a mixture of IAgNPs and Carbopol-940 is a mixture only and no new compound was formed (**Figure 16)**.

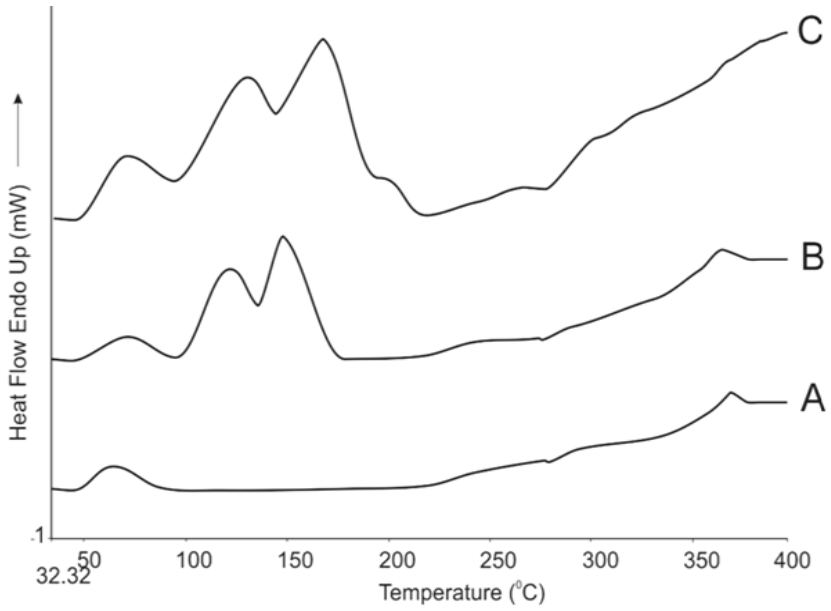

Figure 16: *The DSC thermogram of the* (A) *formulation A (ATE-insulin),* (B) *IAgNPs and* (C) *IAgNPs + Carbapol -940.*

3.9. Visual evaluation of nano gel

The physical appearance of nano-formulation containing gel was reddish-brown. The homogeneously dispersed mixture of the sample showed uniform consistency and smooth texture.

3.10. pH determination

The pH of all the nano-gel formulation was found to be 6.5.

3.11. Viscosity study

The viscosity of nanogel was determined by using a Brookfield viscometer. At 30 rpm, the maximum value of viscosity was 20,056 centipoises at 100%. However, when rpm was increased the viscosity and % torque also increased. Flow index and consistency index of optimized nano gel formulation were determined from the log plot of shear stress v/s log of shear rate (**Figure 17A**), the slope of the plot representing flow index, and antilog of the y-intercept indicating consistency index was calculated. The consistency index of the formulation was found to be 15.11. The flow index n represents the measure of the deviation of a system from Newtonian behavior (n = 1). A value of n<1 indicates pseudoplastic flow or shear-thinning while n>1 indicates dilatant or shear-thickening flow. The gel showed a flow index of 0.3177, indicating pseudoplastic flow behavior. Flow index confers an idea of the flowability of the formulation from the container. Generally, the thicker the base, the lower is

the flow index. The rheogram of nano gel was obtained by the plot of shearing stress versus the rate of shear which confers the thixotropic behavior as a hysteresis loop was obtained (**Figure 17B**).

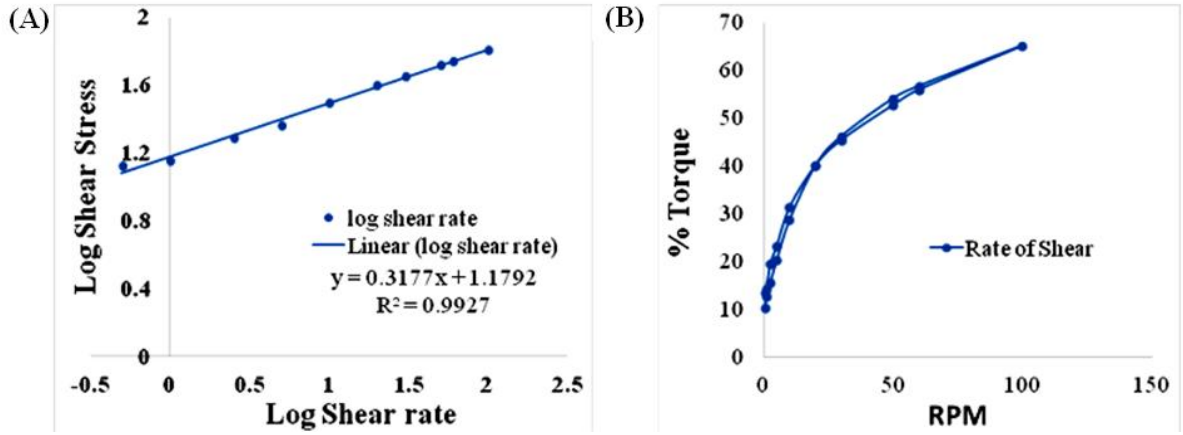

Figure 17: (A) *Plot for Flow index and Consistency index and* (B) *Rheogram of Formulation.*

3.12. Spreadability test

The increase in the diameter due to the spreading of the nanogel was noted. Spread ability of Nano-gel was in the range of 4.9 cm/sec. The values of spreadability indicate that the gel was easily spreadable by the small amount of shear.

3.13. Assessment of wound recovery *in vivo*

Full-thickness excision wound of diameter 15 mm was created initially in all animals (**Figure 18A**) and treated non-diabetic and diabetic animals showed significant variation in initiation and completion of wound closure in comparison with control. Early and later phases of healing on the 5^{th} and 11^{th} days respectively, indicating important phases of healing, were chosen to measure further biochemical and histological parameters simultaneously.

The % closure of the wound, measured until the full closure of wound obtained, in treated diabetic and non-diabetic groups along with vehicle-treated control groups is expressed graphically in **Figure 18B** which indicate the accelerated rate of wound healing in different treatment groups both in nondiabetic as well as diabetic condition compared to respective control groups. Precisely, on the 5^{th} day, the percentages of wound healing in non-diabetic and diabetic rats were significantly improved (20% and 12% respectively) by topical application of IAgNPs treatment in comparison to normal and diabetic control groups (3.33%) (**Figure 18C**). A slightly higher wound healing was observed with AgNPs treatment

(6.67% and 8.67% in normal and diabetic groups) or insulin-ATE treatment (4.67% and 7.27% in normal and diabetic groups) in comparison to control (3.33%) (**Figure 18C**). No significant difference was observed between healing in non-diabetic and diabetic control group animals on the 5th day. A similar pattern was observed on the 11th day of treatment (**Figure 18D**). IAgNPs showed significantly higher wound closure in both normal and diabetic rats (73.33% and 60.0% respectively) in comparison to normal and diabetic controls (40% and 33.33% respectively). AgNPs showed sub-moderate (46.67% and 40.0% in normal and diabetic groups) and Insulin-ATE showed moderately better (53.33% and 46.67% in normal and diabetic groups) wound healing efficacy compared to respective control groups (**Figure 18D**).

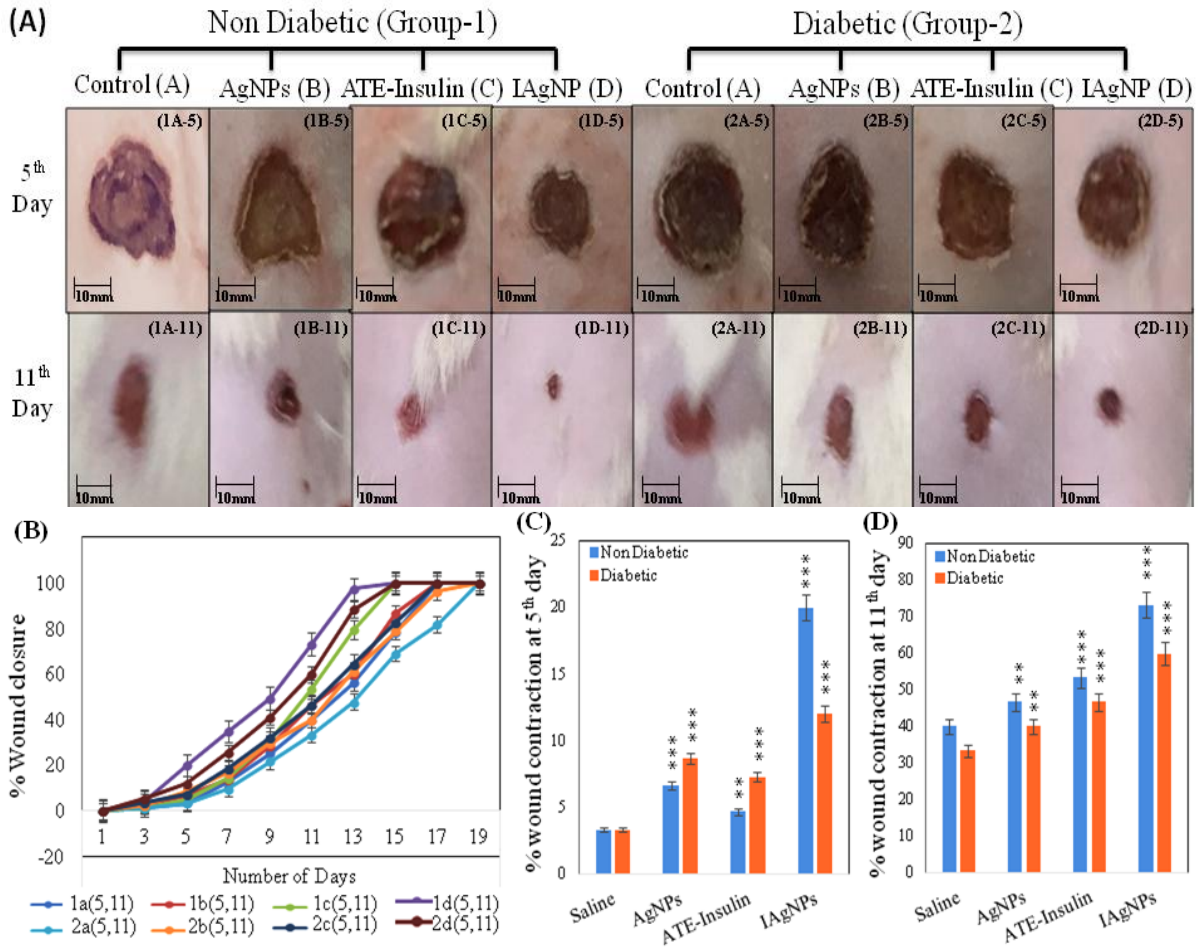

Figure 18: *Healing rate of the wound by AgNPs, ATE-insulin, and IAgNPs treatment in both diabetic and non-diabetic animals on the 5th and 11th day.* (A) *Physical observation of wound contraction in various groups of treatment and control* (B) *% wound closure in different treatment groups (AgNPs, ATE-Insulin, and IAgNPs) and respective controls in diabetic and non-diabetic animals.* (C) *Represents the % wound contraction on the 5th day* (D) *on the 11th*

day in all four subgroups of diabetic and nondiabetic animals. All values are represented by an average ± SD of 6 rats in the group. The statistical significance of the data shown with "": *** P<0.001, ** P<0.01, and * P<0.05.*

3.14. Evaluation of histology and assessment of inflammatory cytokines

The histological section of non-diabetic animals on the 5th day showed a significantly increased level of lymphocytes cells and initiation of collagen deposition near the excision line of the wound. Exudates formation is responsible for leukocyte infiltration which slows down the healing of the wound. The demarcation line represents the complete separation of exudates and re-epithelization was completely absent in 5th day non-diabetic controls. The histological section of diabetic animals showed a higher accumulation of exudates as compared to non-diabetic animals which confirm the initiation of inflammatory events (**Figure 19A**). Commencement of collagen deposition significantly favors strengthening of surrounding muscles to fast closure of the wound, a featured that was found delayed in diabetic groups (**Figure 19A**). On the 5th day, the re-epithelization was insignificant in all groups of diabetic animals compared to non-diabetic ones. Although, AgNPs, ATE-Insulin, and IAgNPs treatment in both groups caused a significant reduction of exudates accumulation compared to saline-treated controls (**Figure 19A**). Photomicrographs of the 11th day showed complete re-epithelization in non-diabetic animals whereas partial re-epithelization was observed in diabetic animals (**Figure 19B**). However, the treatment of IAgNPs in diabetic animals showed complete re-epithelization that was similar to the non-diabetic control group (**Figure 19B**). Additionally, individual treatment of AgNPs, ATE-Insulin, and IAgNPs has shown substantial improvement in collagen deposition in both groups in comparison with corresponding matched controls (**Figure 19B**). Histological data showing good remodeling in treated groups prompted us to evaluate different pro-inflammatory and anti-inflammatory cytokines in the wound milieu. Following IAgNPs treatment quantification of serum IL-6, TNF-α, IL-10 levels were performed in all groups of animals (**Figure 19C**, **D,** and **E**). On the 5th day, a 25% higher level of serum IL-6 (**Figure 19C**) and 2-fold higher levels of serum TNF-α (**Figure 19D**) concentration were evaluated in diabetic rats compared to non-diabetic control. IAgNPs treatment showed 50% inhibition in both groups (**Figure 19C** and **D**). Treatment with AgNPs and insulin-ATE also showed moderate to high reduction in these pro-inflammatory cytokines levels in both groups of animals (**Figure 19C** and **D**). Furthermore, the increase of concentration of the anti-inflammatory cytokine IL-10 increased by 70% and 50% in normal and diabetic animals respectively by IAgNPs treatment on the 5th

day (**Figure 19E**). AgNPs showed only a slight increase in serum IL-10 level whereas insulin-ATE also showed almost 45% and 30% increased anti-inflammatory cytokine concentration as compared with normal and diabetic controls (**Figure 19E**).

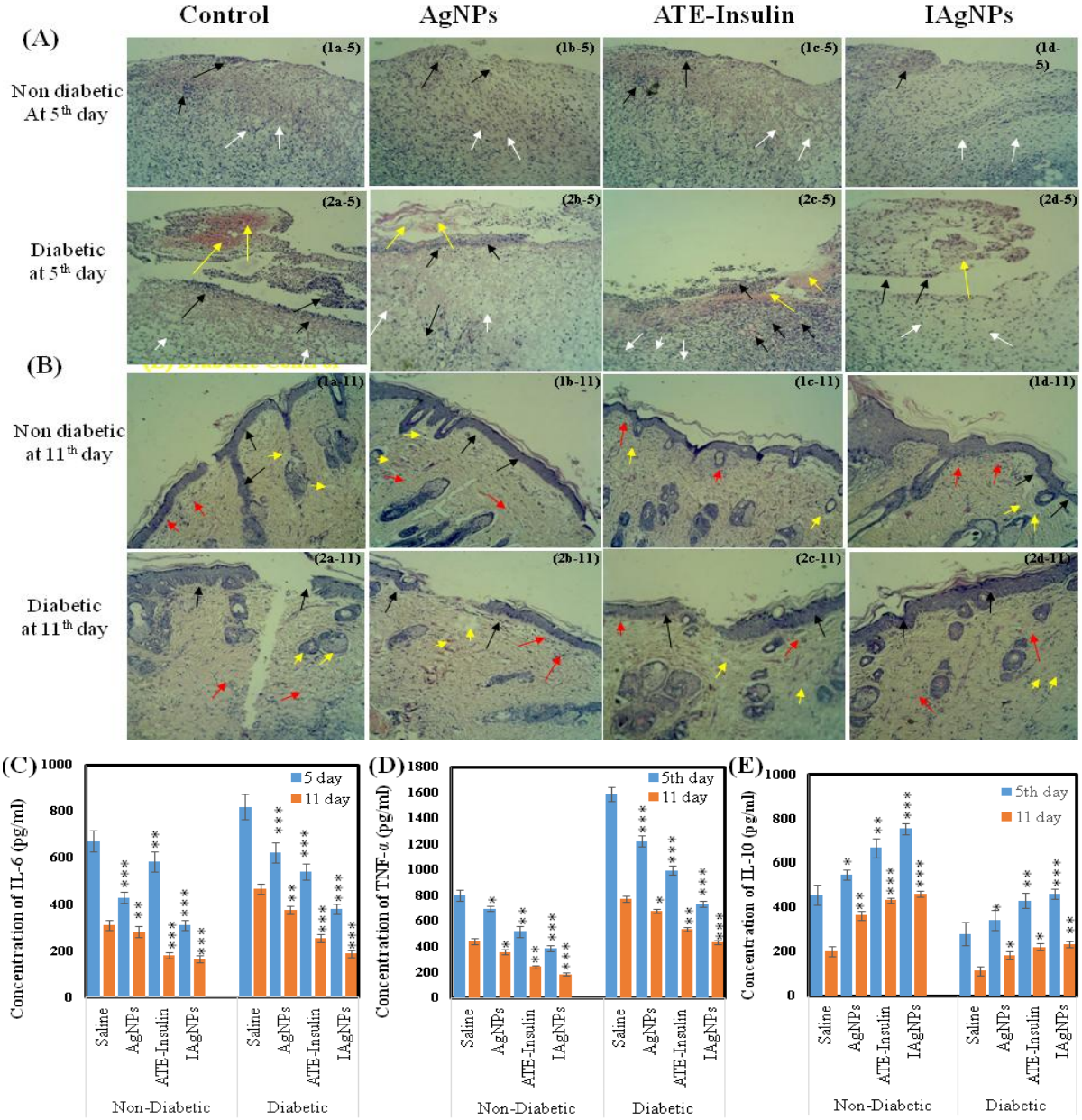

Figure 19: *Histological evaluation at the wound site of different groups (40X) on the 5th* (A) *and* (B) *11th day of post-treatment; Leukocyte infiltration, collagen deposition, and exudates formation are denoted by red, white and yellow arrows respectively.* C, D, *and* E *represent the concentration of pro-inflammatory (IL-6 and TNF-a) and anti-inflammatory cytokines (IL-10) in all subgroups of diabetic and nondiabetic animals on the 5th and 11th day. Results show a significant reduction of proinflammatory cytokines (IL-6 and TNF-a) and increased level of anti-inflammatory cytokines (IL-10) by IAgNPs treatment as compared to control and*

AgNPs and ATE-Insulin treated animals of both sets on 5th and 11th day respectively. All values are represented by an average ± SD of 6 rats in the group. The statistical significance of the data shown with "": *** P<0.001, ** P<0.01, and * P<0.05.*

Even on the 11th day of treatment, diabetic control animals had a higher level of IL-6 and TNF-α (30% and 50% respectively) as compared to non-diabetic controls. However, the treatment of IAgNPs significantly reduces their level (about 45% of IL-6 and 45% of TNF-α) in both sets of diabetic and non-diabetic. Additionally, a moderate reduction in both pro-inflammatory cytokines was observed in diabetic and non-diabetic animals by individual treatment of AgNPs (IL-6, 10% and TNF-α, 10%) and ATE-Insulin (IL-6, 40%, and TNF-α, 30% respectively). Both individual treatment (AgNPs and ATE-Insulin) also increased anti-inflammatory cytokines (IL-10) by about 45% and 50% respectively in diabetic and non-diabetic animals. However, the treatment of IAgNPs showed a higher potential to upsurge the level of IL-10 in both sets of non-diabetic and diabetic animals (65% and 50% respectively). Overall, pro-inflammatory and anti-inflammatory cytokines decreased in the case of all animals on the 11th day showing the neutralization of the inflammatory stage. A faster neutralization was observed with IAgNPs in comparison with respective control groups (**Figure 19C**, **D,** and **E**).

3.15. Conclusions

Immediately after homeostasis of normal wound injury, the inflammatory phase sets in the injured tissue resulting in the release of growth factors, cytokines, and chemoattractants and attracting neutrophils, macrophages, and lymphocytes to the wound site. Growth factors promote the migration of fibroblasts that proliferate along with endothelial cells. Fibroblasts secrete collagen, glycosaminoglycans, and proteoglycans to build up extracellular matrix (ECM). This re-epithelialization phase is a long-term process that gets extended with the physiology of the individual. Features of chronic wound include prolonged inflammatory phase with overabundant leukocyte infiltration with impaired function, high susceptibility to infections, and decreased fibroblast proliferation and signalling.[195-197]In diabetic wounds; the early inflammatory stage is highly extended resulting in delayed recovery. Modulating the balance of pro and anti-inflammatory cytokines is the key to accelerate the inflammatory phase that further determines the rate of remodeling phase characterized by fibroblast accumulation, collagen deposition, and formation of granulation tissue.[198] In the present work, we formulated novel insulin nanoformulation IAgNPs and evaluated wound healing efficacy with respect to their modulation of inflammatory phase and resultant remodeling in

diabetic wounds. Our results showed insulin at physiological condition specifically interacted with AgNPs which induced moderate structural changes at amide-I regions in the protein. In vitro, the wound-healing assay showed enhanced cell migration in both non-diabetic and diabetic conditions compared to controls. Further significantly faster wound healing was observed in normal and diabetic animals with topical application of these formulations, IAgNPs showing the best result among all formulations. In both controls, the persistent higher level of IL-6 and TNF-α was observed on both the 5th and 11th day. A slow increment in serumIL-10 was observed in respective control groups. In contrast, a rapid decrease of pro-inflammatory cytokines and an increase in anti-inflammatory cytokines were observed in IAgNPs treated animals.[199] **Figure 20** shows the synthesis of IAgNPs its anti-inflammatory and wound healing activity.

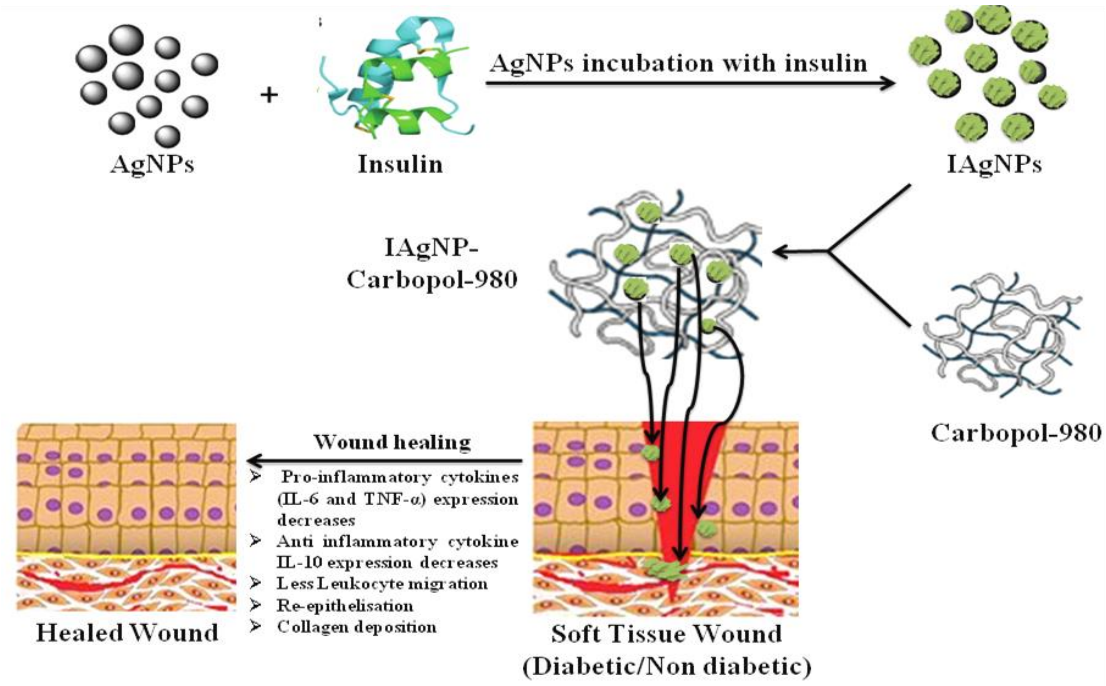

Figure 20: *Shows the mechanism of wound healing by nano-insulin formulation (IAgNPs). IAgNPs accelerated wound healing in diabetic conditions by inhibiting pro-inflammatory cytokines and activating anti-inflammatory cytokines.*

Histological evaluations on the 5th and 11th day showed a significant decrease in the level of leukocytes infiltration by IAgNPs treatment compared to controls and other treatment groups. Also in IAgNPs treated groups, faster deposition of collagens and rapid re-epithelization were observed in comparison with other sub-groups or controls.[200] AgNPs have proven efficacy to reduce contamination load, thereby helping in faster wound recovery.

Insulin-ATE showed moderately higher wound healing in comparison to control by regulating inflammation. Therefore, accelerated wound healing potency of IAgNPs may be attributed to a synergistic effect of both of these phenomena as indicated by increased localized availability of insulin, effective decontamination, and modulation of cytokines resulting in the faster re-epithelialization process both in diabetic as well as in normal animals. As about 5% of the world population is diabetic, therefore this novel and effective formulation has huge potential for future clinical application in diabetic wound healing. Moreover, plausible derivatives of this formulation hold strong promise to be explored in different chronic non-healing wounds including burn, fractured, and radiation-induced wounds in near future.

CHAPTER 4
AMORPHOUS INSULIN ZINC QUANTUM CLUSTERS

4.1. Abstract

Quantum clusters with target specificity are suitable for tissue-specific imaging. In the present work, amorphous zinc insulin quantum clusters (IZnQCs) had been synthesized to promote and monitor wound recovery (**Figure 21**). Easy synthesis, biocompatibility, stability, enhanced quantum yield, and solubility made the cluster suitable for preclinical/clinical exploration. Zn^{2+} is known for its binding to insulin hexamer. Here we report the reformation of the structure in a quantum cluster form in the presence of Zn^{2+}. The formation of IZnQCs was confirmed by the change in zeta potential from -25.6 mV to -17.9 mV and also the formation of protein metal interaction was confirmed in FTIR bands at 450, 480, and 613 cm^{-1} for Zn-O, Zn-N, and Zn-S, respectively. HRTEM-EDS and SAED data analysis showed an amorphous nature of the cluster. The binding of IZnQCs to the cells has been confirmed using confocal microscopy. IZnQCs showed a synergistic effect in wound recovery than insulin or Zn^{2+} alone. Further due to high fluorescence this recovery process can be monitored under an appropriate setup. Wound healing promotional activity, target specificity, and fluorescence properties make the IZnQCs ideal to use for bioimaging along with promoting and monitoring of wound recovery agent.

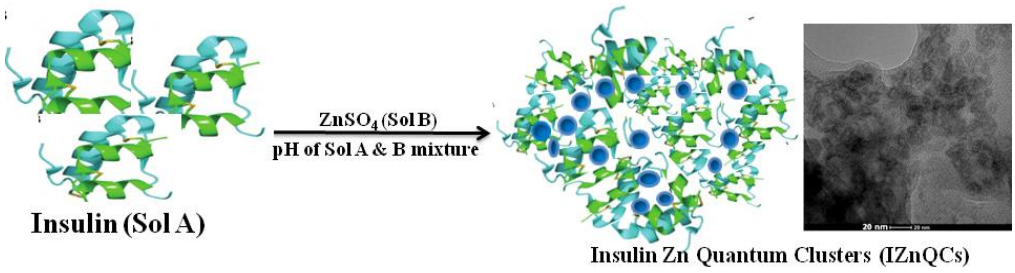

Figure 21: *Schematic presentation of the formation of amorphous insulin zinc quantum clusters (IZnQCs).*

4.2. Introduction

Progress monitoring of recovery of internal injuries like surgical wounds always remained a matter of challenge. Some of the technologies that are used for this purpose include a near-infrared optical scanner (NIROS), diffuse reflectance spectroscopy (DRS), multispectral imaging (MSI), laser speckle imaging (LSI), laser Doppler imaging (LDI), hyperspectral imaging (HSI), and spatial frequency domain imaging (SFDI), etc.[201,202] But some of the major challenges that remained associated with these technologies include technical

complexity, low detection level, low penetration depth, detection depth, and expense.[203-210] Other than these techniques metal-organic frameworks (MOFs) or bioMOFs showing luminescence properties can be used for bioimaging purposes.[211-213] Recently metal (Cu, Ag, and Au) protein quantum cluster has caught the attention of the researchers for targeted delivery and efficient bioimaging.[214-215] Quantum clusters (QCs) are luminescent (fluorescent or phosphorescent) clusters that may associate with crystalline quantum dots (QDs) of 1-10 nm size or amorphous hetero atoms.[216] Quantum clusters have high emission rates, large Stokes shift, and photo-stability.[217,218] The QCs can be synthesized by using any reducing agent such as $NaBH_4$, alkyl thiol, or glutathione or can be prepared by using proteins, peptides, amino acids, DNA, and dendrimers, etc.[219-221] At basic pH the aromatic groups of amino acids of the protein start donating electrons helps in reducing the metal and disulfide bonds present in protein can stabilize the nucleated cluster.[219,222]

Further, the use of nano-clusters and a variety of quantum dots for bioimaging and wound recovery activities have been reported by many groups, for example, Das NK and co-workers in 2015 prepared glutathione-Cu nanoclusters having nontoxic behavior and bind particularly with the nuclear membrane and emit blue fluorescence and tested its bio-imaging properties against human cell lines.[223] Researchers have also developed quantum dots on the insulin platform and used those for various biological activities like bio-imaging and wound healing. In 2011, Liu CL and co-workers have synthesized biocompatible and bioactive fluorescent Insulin-Au quantum clusters and then used that formulation for bio-imaging on brain cells and C2C12 myoblast cell lines. They also showed its' utility to maintain the blood glucose level *in vivo*.[224] Amorphous fluorescent particles have recently caught the eye of researchers for their excellent, biocompatibility, solubility, and stability, for example, amorphous luminescent bovine serum protected gold clusters hosted on nanofibres prepared by Subramanian V and co-workers in 2017 and explored for the detection of trinitrotoluene in trace amount.[225] In 2018, Amorphous carbon dots self-passivated in bulk quantity synthesized by Siddique AB and co-workers and used to detect 2,4,6-trinitrophenol (TNP), an explosive in trace amounts.[226] Polymorphic crystalline copper iodide clusters with bright green emission were prepared by Benito Q and co-workers (2014) and studied their mechano-chromic luminescence properties in which Cu_4I_4 shows Cu-Cu intermolecular distance shortening through the disruption in crystal packing.[227] Yang H and co-workers (2017) synthesized heterojunctions of iron oxyhydroxide/g-C3N4 amorphous nanosheets for enhanced photocatalytic activity.[228] Wang G and co-workers (2020) synthesized metastable crystalline dual phased ZnSb-based films and explored their Insulator-metal transition (IMT)

properties.[229] Amorphous (ZnS) nanoparticles conjugated with BSA synthesized by Cao Y and co-workers (2011) to check its inhibition effect on the growth of tumor cells.[230] Xie J and co-workers used Amorphous and crystalline protein metal clusters for the bioimaging purpose of the brain cells.[231] In the case of an amorphous arrangement, metal protein clusters constitute atoms that do not have the ordered or regular pattern means the arrangement of the constituents i.e. atoms in such cases has only short-range or over a short distance.[232]

The insulin receptor (IR) exists on the membrane of all mammalian cells.[233] The number of receptors varies from 40 for erythrocytes to 200~300 X 10^3 for adipocytes and hepatocytes and in cancerous cells; the content of IR is much higher than normal cells.[234-237] The target-specific binding of insulin to IR or IGFR-I plays an important role in the wound repair or regeneration and works through the transition of M1 pro-inflammatory cytokines (IL-6, IL-1β, IL-12, TNF-α, STAT-1, and NFkβ$^{P50/P65}$) to (Akt, STAT-3, IL-10, IL-4, IL-13, and NFkβ$^{P50/P50}$) anti-inflammatory M2 cytokines. The nanoforms of insulin such as insulin Ag (silver) nanoparticles (IAgNPs) showed promising wound recovery in diabetic as well as in nondiabetic rat models through changes in proinflammatory cytokine level and a significant decrease in the infiltration of leukocyte, faster collagen deposition, and re-epithelization with IAgNPs and insulin in comparison to the respective controls.[238] Similar to insulin metals also act as wound healing agents like Zn (Zinc) can enhance cell division, control inflammation, enhance proliferation, angiogenesis, remodeling of tissue, and formation of the scar.[239] It shows mitogenic pathways through the release of different growth hormones responsible for cell growth and differentiation such as GH (Growth Hormone) and IGF-1 (Insulin-like Growth Factor-1) by influencing their gene expression through transcription factors.[240,241] Zn supplements alone have been given to diabetic patients for treating diabetes.[242] The presence of Zn insulin undergoes conformational changes and it leads to enhancement of insulin binding with the insulin receptor and helps insulin in performing its activity.[243-245] It has also been reported that Zn, in the absence of insulin, can cause phosphorylation of tyrosine present on IR (insulin receptor) upon prolonged exposure and plays a similar role as insulin.[246] Due to this effect binding effect of Zn, it can also activate a similar wound recovery pathway as insulin and can control pro-inflammatory cytokine activity, enhances the anti-inflammatory cytokine level and various other GFs, and helps in the recovery of the wound.[247,248] Batool M and co-workers have synthesized Zinc oxide particles and Han B and co-workers prepared Zinc sulphide for skin regeneration or wound healing.[249-251]

In this work, we are reporting the application of novel amorphous metal-protein quantum clusters for their receptor-targeted *in vitro* wound healing activity for the first time. Here, novel amorphous insulin zinc quantum clusters (IZnQCs) have been synthesized using the one-pot synthesis technique. This study also shows the unprecedented synergistic effect of insulin and zinc for wound recovery when applied in the IZnQCs form. Internal wounds after invasive surgery are very delicate and proper healing is needed to maintain the life quality of the patient. Due to the unavailability of the internal wound recovery monitoring system, many times surgical wounds need to be reopened for the treatment purpose which increases the health care cost and compromises the life quality of the patient. Since the newly developed system has a dual property for wound recovery and targeted fluorescent bio-imaging, these findings will open a new opportunity for better wound management. Further intervention is needed to monitor the recovery of the post-surgical internal wounds in laboratory-based small animal models.

4.3. Material and methods

4.3.1. Chemicals and Cell line

Formaldehyde (Sigma Aldrich, USA), Hydrochloric acid (HCl, SD fine chem. Limited, Mumbai), Human recombinant insulin (Huminsulin obtained from Elli Lilly and company Pvt., Ltd., India), Sodium hydroxide (NaOH, Avantor performance Materials India limited, Gujarat India) and Zinc sulfate solution ($ZnSO_4$, Sigma Aldrich, USA). Molecular biology grade chemicals like Formaldehyde, DMEM-F12 media (AL219A), New born calf serum (RM10437), and Phosphate buffered saline pH 7.4 (PBS, TL1099), 100 X Penicillin-streptomycin mixture, were purchased from Himedia, India. HEKa cells (PCS-200-030; ATCC) were cultured at 5% CO_2 and 37°C in an incubator.

4.3.2. Preparation of Zinc Insulin Quantum Clusters

The synthesis of Insulin metal quantum clusters synthesis was performed by using insulin and $ZnSO_4$ salt solution of 1.82 µM concentration in an aqueous medium. The insulin pH was adjusted to basic (10.5) using NaOH solution which makes SOLUTION A and placed in the dark. In another tube 18.2 µM solution of $ZnSO_4$ (SOLUTION B) was taken. After preparing both the solutions, the insulin was added to the metal salt solution in 1:1 volume, after mixing both the solutions the pH was adjusted to 7.4 (physiological pH) by using the HCl (0.1 N) and then dialyzed. The resulting solution of metal insulin was kept in an incubator at 37°C for 12h at slow stirring (240 rpm).[224,232,252]

4.3.3. Instrumentation

UV absorption spectra of prepared insulin linked Zn metal quantum clusters ($ZnSO_4$) was performed by using UV-2600 Shimadzu spectrophotometer and operated between the ranges from 200 nm to 800 nm. The absorption spectra of the $ZnSO_4$ salt and insulin were measured to check the interactions between Zn metal and insulin protein.

The fluorescence spectrophotometer (Perkin Elmer LS55, USA) was to detect the binding of protein insulin with metal quantum clusters using the IZnQCs sample in comparison with the control insulin. The fluorescence spectroscopy was performed by using a 272 nm excitation wavelength, coupled with excitation and emission slit of 10 mm and observed at emission scan from 280-800 nm. The percentage increase in the intrinsic fluorescence; the fluorescence intensities of IZnQCs and insulin were compared using the following equation (xi)

$$= \frac{\text{F.I. (IZnQCs) - F.I. (insulin)}}{\text{F.I. (insulin)}} \times 100\% \quad \text{..... (xi)}$$

The quantum yield of human recombinant insulin and insulin protected quantum clusters of IZnQCs was evaluated using the standard tyrosine fluorescence quantum yield by the following equation (xii).

$$Q.Y.(S) = \frac{Q.Y.(Tyr)\times I(S)\times 1\text{-}10^{-Al}(Tyr)\times n^2(S)}{I\,(Tyr) \times 1\text{-}10^{-Al}\,(S) \times \eta^2\,(Tyr)} \quad \text{..... (xii)}$$

Here, Q.Y. is Quantum Yield, I is Integrated Emission Intensity, η is Refractive Index of Solvent, A is the Absorbance at Excitation Wavelength, *l* is the length of absorption cell, Tyr is Tyrosine (reference), and S is Sample.[253]

High-resolution transmission electron microscopy (HR TEM) Talos F200S G2, Thermo Scientifics, and selected area electron diffraction (SAED) were used to find out the arrangement or distribution pattern of different elements present in the IZnQCs. To perform HRTEM, the sample was centrifuged at low rpm around 240 rpm for 10 to15 min, after that the sample was washed for removing the impurities. The electron dispersive X-ray spectroscopy (EDAX) after dialysis of pH 7.4 and 10.4 insulin and IZnQCs were performed, analyze the percentage of zinc metal in different samples. FTIR Spectrophotometer (Agilent Cary 600 series) was performed for the detection of different functional groups present in IZnQCs. Before doing FTIR the sample was washed for removing the impurities and a scan was performed between 4000 cm^{-1} to 400 cm^{-1}.

4.3.4. *In vitro* studies

The biocompatibility, effect of IZnQCs on cell viability and cell migration was determined by using the HEKa cell line.

4.3.4.1. Cell viability

The viability of the cells was checked out on HEKa (Normal human epidermal keratinocyte) by using MTT (3-(4, 5-dimethylthiazol-2-yl)-2, 5-diphenyltetrazolium bromide) assay. HEKa of density 1 X 10^4 (per well density) has been seeded in 96 well plates and was allowed to 70-75% confluent. The cells after that were incubated with different percentages (1.5, 7.5, 30, and 60 μM) of IZnQCs, insulin, Zn salt, and the mixture of insulin and Zn salt. After treating the cells were incubated at 37°C in the incubator for 24h. After 24h the MTT (2 mg/ml in 5% ethanol) was added for 3h. After 3h the MTT along with media was removed and 200 μl dimethyl sulphoxide (DMSO) was added to dissolve the formazan crystals. The absorbance was checked at 570 nm. The inhibition % was calculated by using the following equation xiii.

$$\% \text{ inhibition} = [1 - (A_t/A_s) \times 100] \% \quad \text{..... (xiii)}$$

A_t is the test substance absorbance and A_s control solvent absorbance. For every three independent readings were taken [254,255]

4.3.4.2. Confocal bioimaging

IR is present on the cell surface, and therefore, to perform receptor-targeted cellular imaging confocal microscopic studies had been carried out. To achieve that HEKa cells were treated with IZnQCs (18.2 nM; protein) along with control insulin (18.2 nM) for 2h at physiological conditions in DMEM medium supplemented with 10% fetal bovine serum respectively. After the incubation cells were washed twice with 1 X PBS and fixed and permeabilized with methanol (95%) for 5 mins. Thereafter, the fixed cells were treated with 10 μg/ml RNase A at 37°C for 3h for removal of the RNA present inside the cell. After that to stain the cellular nucleus 1 μg/ml propidium iodide (PI) was added and incubated for 30 mins. The cells were imaged under the Zeiss LSM 510 Meta confocal microscope [25-258]

4.3.4.3. Effect of IZnQCs on Wound Recovery using phase contrast and fluorescence imaging

IZnQCs induced more cell migration in the HEKa cell line. The cells were cultured in high glucose DMEM-F12 FBS free medium with 5% CO_2 at 37°C. After the cells get 80-85% confluent, a wound was generated by a cell scratch method and treated with different concentrations (1.5, 7.5, 30, and 60 μM) of IZnQCs, insulin, Zn salt, and the mixture of

insulin and Zn salt (I + Zn). Time-lapse images were taken and changes in the width of the scratch were measured at 6h, 12h, and 24h using after respective treatment. Further, time-lapse images were also taken for cellular fluorescence for monitoring wound recovery. All the images were taken using a Dewinter fluorescence inverted microscope.

4.3.4.4. Determination of combination index (CI) of Zinc-insulin

A combination index (CI) is a quantitative measure that provides the effect of the dose of a single drug and combined drug treatment. A combination effect can be less than 1 (CI <1) when different drugs are administrated together may work together for the enhancement of each other's activity called a synergistic effect. CI equal to1 (CI=1) may do not get in the way of each other effective response or more than 1 (CI >1) called additive effect in which may inhibit each other activity called antagonistic effects. For calculating the CI the migration of the treated Heka cells was determined and then CI calculated using the equation xiv.

$$CI = (D)_1/(D_x)_1 + (D)_2/(Dx)_2 \quad \text{..... (xiv)}$$

$$\text{Where } D_x = D_m [f_a/f_u]^{1/m} \text{ ..... (xv)}$$

D_1 and D_2 are the Zn salt and insulin dose respectively. $(D_x)_1$ and $(D_x)_2$ are the single drug concentrations giving the same effect; determined using the median effect equation (xv) and f_a and f_u represent the affected and unaffected cell fractions are the median dose and equal to $10^{(\text{-y-intercept})/m}$, m is the slope median in the median effect plot of log (D) vs log (f_a/f_u).[257,259]

4.4. Statistical analysis

All data were presented as the mean ± SD of at least three independent experiments. By performing one-way ANOVA the corresponding *P*-value was measured to check the statistical significance of the data.

4.5. Absorbance spectra and fluorescence spectra

A sharp single Sharp resonance peak of insulin and after 48h incubation of insulin with Zn metal salt the peak found at 272 nm (**Figure 22A**) was observed due to the formation of metal protein quantum clusters. The fluorescence or emission spectra were obtained between 280 nm to 550 nm with an emission maximum at 303 nm and 385-527 nm (inset is showing a trailing of fluorescent from 385 nm onwards) after excitation at 272 nm. 66.7 ± 13.6% increases in intrinsic fluorescence of insulin take place after incubation with $ZnSO_4$ after 48h

incubation at standardized conditions (**Figure 22B**). The quantum yield of insulin was found to be 0.021 and that of IZnQCs comes out to be 0.112.

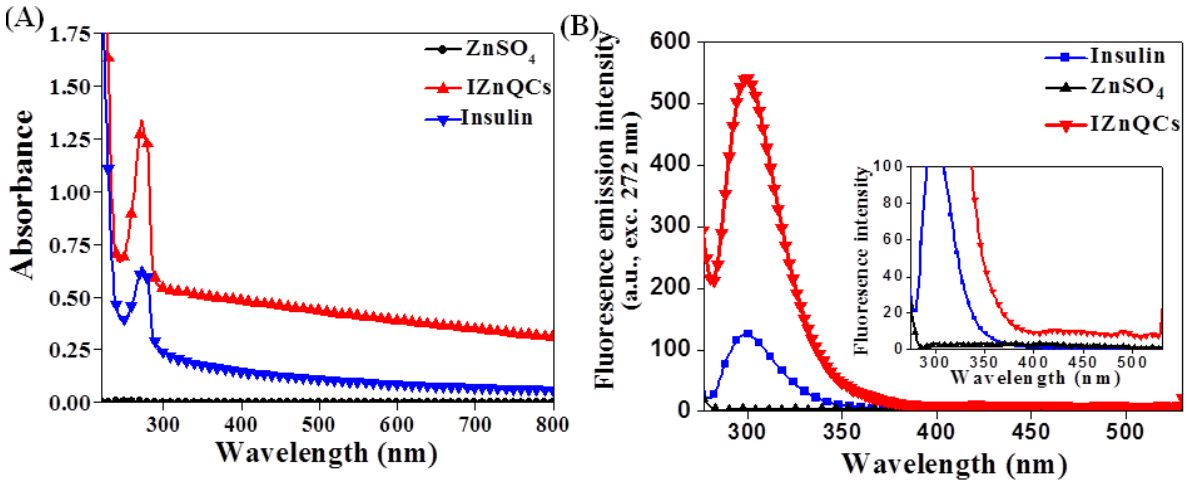

Figure 22: *Physical characterization of IZnQCs. In physical interaction studies* (A) *absorption spectra show the peak of insulin and after insulin incubation, with Zinc (IZnQCs) at 272 nm. Emission spectra of IZnQCs* (B) *after excitation at 272 nm. The emission peak was observed at 303 nm. Inset is showing a trailing of fluorescent from 385 nm onwards. 66.7±13.6% increases in the intrinsic fluorescence of insulin due to the formation of IZnQCs.*

4.6. Structure and composition of metal insulin clusters

The DLS average size of the clusters is 154 ± 43 nm and the zeta potential of insulin changes from -25.6 mV to -17.9 mV after cluster formation. The arrangement of Zinc quantum clusters in images HRTEM **Figure 23A** on a 20 nm scale and **Figure 23B** 100 nm showed the dark spots indicate the formation of localized clusters of Zinc.

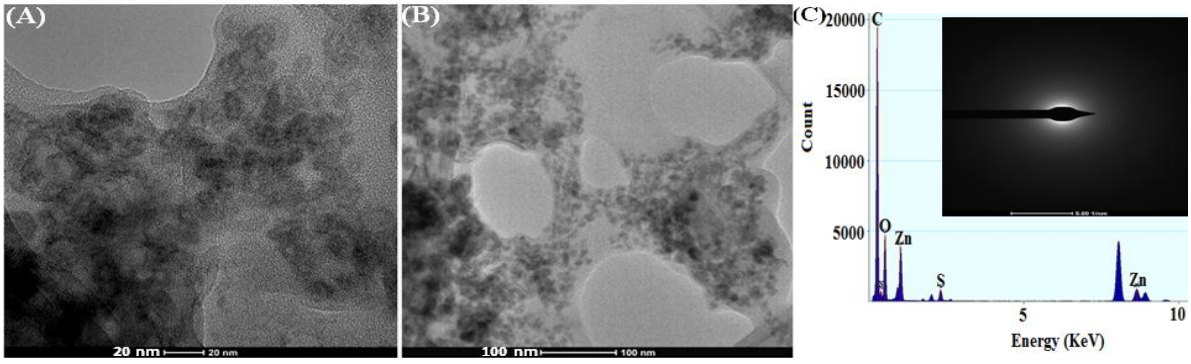

Figure 23: *A micrographic study using HRTEM* (A) *on a 20 nm scale and* (B) *100nm showed the distribution of Zn atom in IZnQCs.* (C) *Selected Area electron diffraction studies showed the amorphous nature of the materials with the presence of Zn. Inlet is showing the Selected Area Electron Diffraction (SAED) pattern.*

Figure 23C shown as a top inset, selected area electron diffraction (SAED) pattern, shows a diffused halo devoid of rings, which is mainly in the case of the amorphous sample. In this arrangement cluster constituting atoms does not have the ordered or regular pattern means the arrangement of the constituents i.e. atoms in such cases have only short-range or over a short distance. These amorphous zinc clusters are nearly spherical. HRTEM-SAED showed the presence of a 1.24 ± 0.03 atomic percentage of Zn metal in protein quantum clusters.

4.7. FTIR spectra

The comparative spectrum of FTIR measurement of $ZnSO_4$, insulin, and IZnQCs was carried.

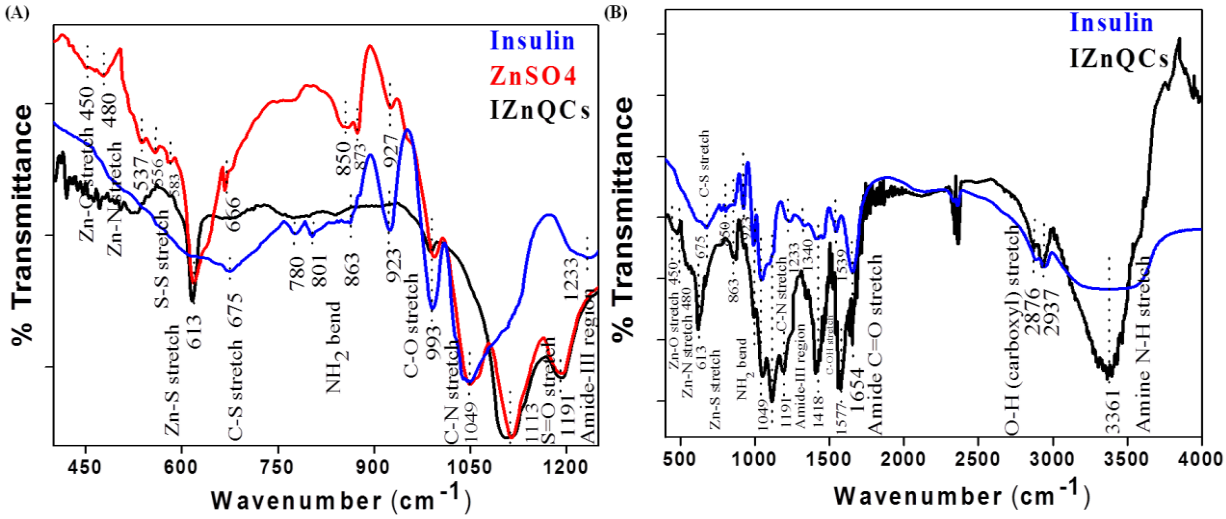

Figure 24: *FTIR spectroscopic studies to coin the interactions between zinc metal and insulin. Spectroscopic interaction studies* (A) *FTIR spectra between $ZnSO_4$, insulin, and IZnQCs show comparative studies between the ranges of 1250 to 400 cm^{-1} showing the formation of Zn-O, Zn-N, and Zn-S new bonds in IZnQCs,* (B) *spectra range from 4000 to 400 cm^{-1} indicates the involvement of different functional groups in interaction with Zn.*

The interactions involved in the binding of metal with protein ranges from 1200 to 400 cm^{-1} and is represented in **Figure 24A**. Due to the intermolecular interactions between insulin and metal salt, the peak appears at 450 cm^{-1} for the Zn-O[258] bond, Zn-N at 480 cm^{-1}.[260] No S-S bond peaks were found in insulin but IZnQCs the peaks of S-S stretching vibrations at 537, 556 and 583 cm^{-1} indicate some linkage between metal and protein.[261] NH_2 bend peak at 780, 801, and 863 cm^{-1} in insulin but 850 and 873 cm^{-1} in IZnQCs show some linkage between metal and insulin.[262] Further the peak position of Zn-S at 613 cm^{-1} same for both $ZnSO_4$ and IZnQCs but broad in the case of quantum clusters.[263] C-S bond shows the shift from 675 cm^{-1}

in insulin to 666 cm^{-1} in IZnQCs.[217] Similarly, C-O stretching peak in insulin at 923 cm^{-1} shifts to 927 cm^{-1} in IZnQCs.[263] There is no change in C-N and S=O bond (1049 and 1049 cm^{-1} respectively) found after the formation of quantum clusters of protein.[263,264] Furthermore, conformational changes in insulin protein structure due to the interaction of ZnDs were represented in FTIR from 400-4000 cm^{-1} in **Figure 24B**.

Table 3: *Comparative table showing the FTIR peak position of different functional groups present in $ZnSO_4$, insulin, and IZnQCs showing the formation of Zn.*

Wavenumber (cm^{-1})			
Functional Groups	**Insulin**	**IZnQCs**	**$ZnSO_4$**
Zn-O stretch	----	450	----
Zn-S stretch	----	480	----
S-S stretch	----	556 583	----
Zn-S stretch	613	613	----
C-S stretch	675	666	----
NH_2 bend	780 863	850 873	----
C-O stretch	923	927	----
C-N stretch	1049	1049	----
S=O stretch	----	1113	1113
C-OH stretch	1418	1418	
Amide C=O stretch	1539	1577 1654	----
CH_3 symmetric stretch	2876	2876	----
CH_3 asymmetric stretch	2937	2937	----
Amine N-H stretch	3361	3361	----

4.8. *In vitro* studies

4.8.1. Cell viability

The MTT result for cell viability depends upon the cell's mitochondrial activity. Cell division activity or viability on HEKa (**Figure 25**) using 1.5, 7.5, 30, and 60 µM different amounts of

controls (Zn salt, insulin, I + Zn) and IZnQCs. Zn + I treated cells shows 1.5 µM (107.31 ± 7.29%), 7.5 µM (116.849 ± 5.98%), 30 µM (131.466 ± 22.05%), and 60 µM (148.762 ± 24.66%) cell viability. Insulin shows 1.5 µM (102.38 ± 12.8%), 7.5 µM (129.19 ± 3.94%), 30 µM (133.05 ± 6.65%), 60 µM (148.11 ± 3.32%). The cells exposed to Zn salt also showed more cell viability in 1.5 µM (104.08 ± 13.49%), 7.5 µM (123.18 ± 8.88%), 30 µM (126.71 ± 8.67%) and 60 µM (131.51 ± 1.811%). Cell division after IZnQCs treatment showed the more significant changes in 1.5 µM treatment (132.24 ± 7.29%), 7.5 µM (175.94 ± 5.64%), 30 µM (186.07 ± 22.81%) and 60 µM (188.71 ± 16.95%) in comparison to treated and untreated controls. The results (**Table 4**) suggested that these quantum clusters have the potential to enhance cell division and can help in wound healing. The IZnQCs shows 32.26 ± 7.29% more division in 1.5 µM concentration, in 7.5 µM, 30 µM and 60 µM 75.92 ± 5.64%, in 86.07 ± 22.81% and 88.71 ± 16.94% respectively more division in comparison to control. The measurements were statistically significant.

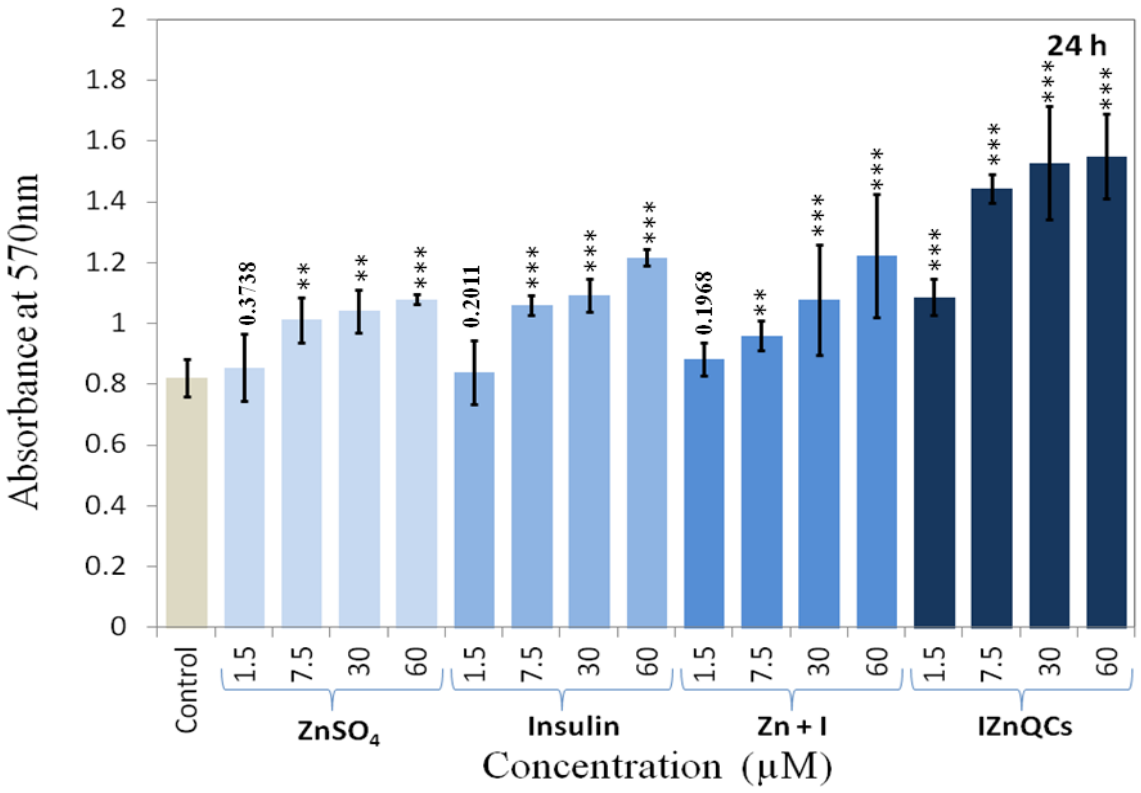

Figure 25: *MTT assay on HEKa using controls (Zn salt, insulin, I + Zn) and IZnQCs shows that the cell viability increases after treatment (1.5, 7.5, 30, and 60 µM) in comparison to untreated cells. The significant changes in cell division are observed in the case of 7.5, 30, and 60 µM of IZnQCs in comparison to untreated and treated controls. The statistical significance of the data shown with "*": *** P<0.001, ** P<0.01, and * P<0.05.*

Table 4: *MTT assay to determine cellular metabolism rate of HEKa cells were treated with 1.5 - 60 µM concentration of controls (Zn salt, insulin, I + Zn) and IZnQCs for 24h and data were plotted as mean value ± SD of three independent experiments.*

% of the change in mitochondrial reductase activity				
Dose	**IZnQCs**	**Zn + I**	**Insulin**	**$ZnSO_4$**
1.5 µM	132.24 ± 5.52%	107.31 ± 7.29%	102.38 ± 12.8%	104.08 ± 13.49%
7.5 µM	175.94 ± 5.64%	116.849 ± 5.98%	129.19 ± 3.94%	123.18 ± 8.88%
30 µM	186.07 ± 22.81%	131.466 ± 22.05%	133.05 ± 6.65%	126.71 ± 8.67%
60 µM	188.71 ± 16.95%	148.762 ± 24.66%	148.11 ± 3.32%	131.51 ± 1.811%

4.8.2. Confocal bioimaging

Confocal imaging was performed to confirm the cellular imaging application of insulin metal quantum clusters. In HEKa cell lines, the IZnQCs treated cells showed fluorescence of bright blue color due to the binding of IZnQCs with the insulin receptors present on the surface of cells. Insulin and IZnQCs treated HEKa cells (**Figure 26A-H**) are showing bright blue fluorescence in **Figure 26E** due to IZnQCs whereas in **Figure 26B** no fluorescence was observed due to the non-binding of insulin. **Figure 26B** and **F** are showing PI nuclear staining for the HEKa cell lines. Phase images of the cells shown in **Figure 26C** and **G** and merged images in **Figure 26D** and **H** of the insulin control and IZnQCs treated HEKa.

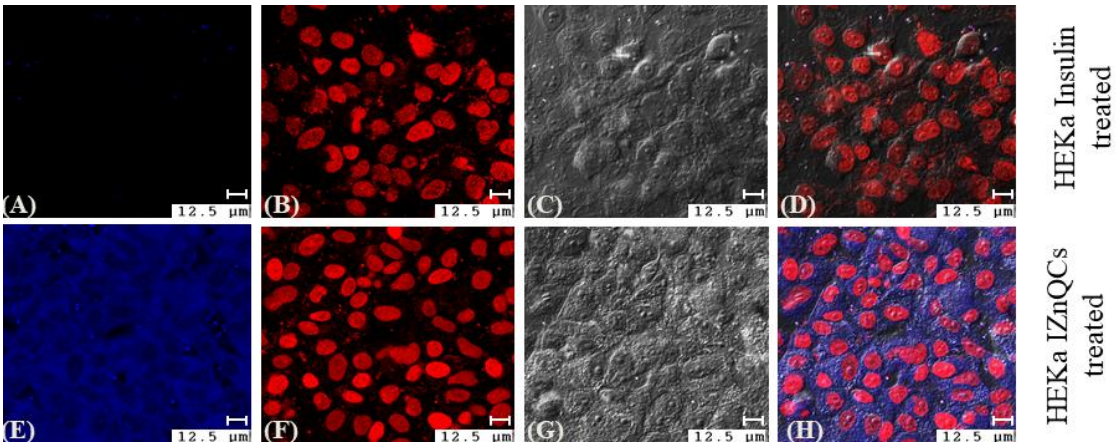

Figure 26: *Confocal bioimaging of HEKa cells using IZnQCs. HEKa cells* (A-D) *were treated with insulin and (E-H) with IZnQCs.* (E) *Showing blue fluorescence of IZnQCs in BP 360/51 channel whereas only insulin (A) did not show any signal.* (B, F) *showed a stained nucleus with Propidium iodide.* (C, G) *showed phase images of the treated cells and* (D, H) *showed all channel merge images.*

Cells showed blue fluorescence on the cell surface which suggests that IZnQCs binds to the cell membrane. As, the quantum yield 0.021 and 0.112 for insulin and IZnQCs respectively, a bright blue fluorescence was observed in the IZnQCs cells which makes it ideal for exploring as receptor-targeted bio-imaging material.

4.8.3. Cell migration assay

IZnQCs induced HEKa cell migration in comparison to treated (Zn salt, insulin, I + Zn) and untreated controls. The extent of cell division and migration increased with the increase in concentration and time.

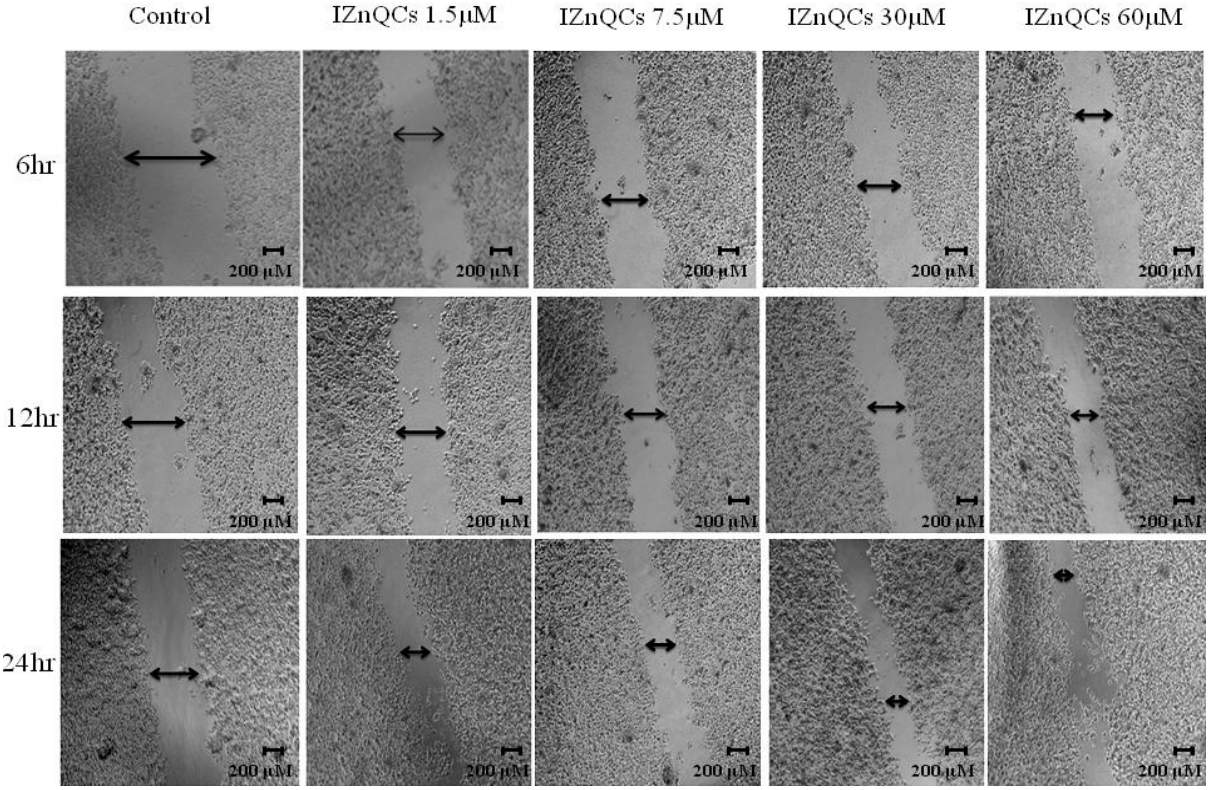

Figure 27: *Promotion and monitoring of wound healing in under phase contrast and fluorescence microscopy using IZnQCs. HEKa treatment using 1.5, 7.5, 30, and 60 µM different concentrations of IZnQCs show the decrease in wound diameter at different hours 6, 12, and 24h with respect to control. At 1.5µM concentration, after 6, 12, and 24h the changes in wound diameter are less in comparison to control but more significant changes are observed in 7.5, 30, and 60 µM concentration.*

Cells treated with IZnQCs for 6, 12 and 24h shows 39.49 ± 1.29%, 27.58 ± 3.72% and 43.02 ± 1.62% at 1.5 µM **Figure 27D-F** and 52.88 ± 0.83%, 46.86 ± 1.46% and 67.81 ± 0.83% for 60 µM **Figure 27G-J** cell migration respectively in comparison to untreated

control scratch diameter **Figure 27A-C**. The fluorescence imaging using Dewinter was performed shows fluorescence on the cells as performed by using a confocal microscope. In addition to these concentrations, the cells were also treated with 7.5 µM and 30 µM concentrations of IZnQCs. Cells show 42.03 ± 3.04%, 34.08 ± 1.57% and 46.51 ± 3.38% migration after treatment with 7.5 µM IZnQCs and 45.25 ± 2.14%, 36.32± 1.63% and 58.60 ± 0.72% at 30 µM concentrations of IZnQCs at 6, 12 and 24h respectively (**Figure 27**). Along with IZnQCs treatment; the cells also treated with Zn salt, insulin, I + Zn, show significant migration in comparison to control. With 1.5 µM Zn salt addition to cells, 21.18 ± 3.72%, 0.224 ± 0.030% and 18.60 ± 2.49% migration, at 7.5 µM Zn salt 22.88 ± 1.27%, 12.11 ± 0.59% and 35.58 ± 0.76% enhancement in cell growth, with 30 µM 45.25 ± 2.56%, 26.01 ± 3.49% and 39.07 ± 2.86% wound closure and after 60 µM treatment 49.97 ± 4.69%, 33.86 ± 1.96% and 45.81 ± 5.09% more cell migration at 6, 12 and 24h respectively in relation to control (**Figure 28**).

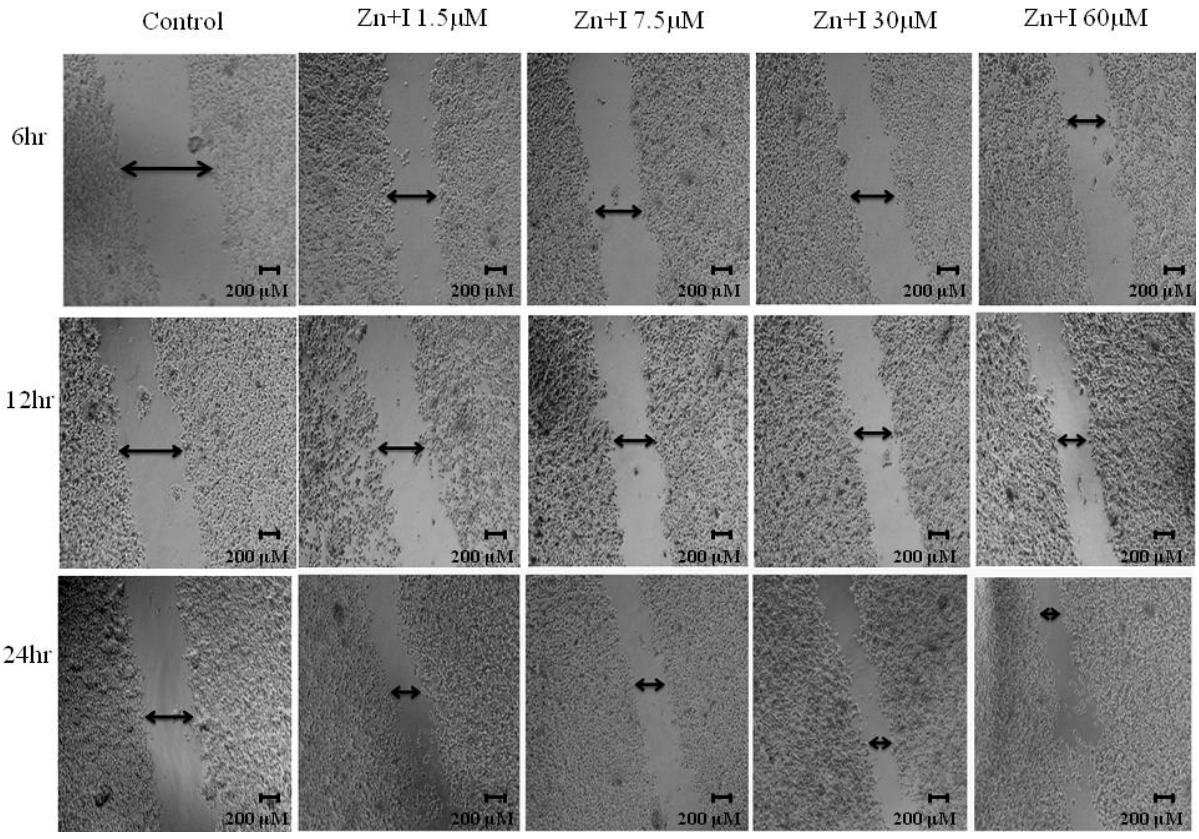

Figure 28: *Changes in wound diameter after Zn + I treatment on HEKa using1.5, 7.5, 30, and 60 µM different concentrations of Zn + I at 6, 12, and 24h with respect to control shows at 60µM concentration significant changes in wound diameter takes place in comparison to 1.5, 7.5 and 30 µM concentration.*

Similarly, cells treated with insulin, 1.5 µM insulin treatment, 39.49 ± 1.6%, 20.18 ± 1.29% and 29.30 ± 1.28% and migration, with 7.5 µM insulin concentration 42.03 ± 1.35%, 24.89 ± 5.17%, and 41.26 ± 2.03% cell growth enhancement, with 30 µM 45.25 ± 2.50%, 32.51 ± 0.38% and 51.39 ± 3.22%, closure of the wound and after 60 µM treatment 52.88 ± 0.83%, 45.067 ± 7.07% and 63.72 ± 1.66% more migration of cell at 6, 12 and 24h respectively in relation to untreated control (**Figure 28**).

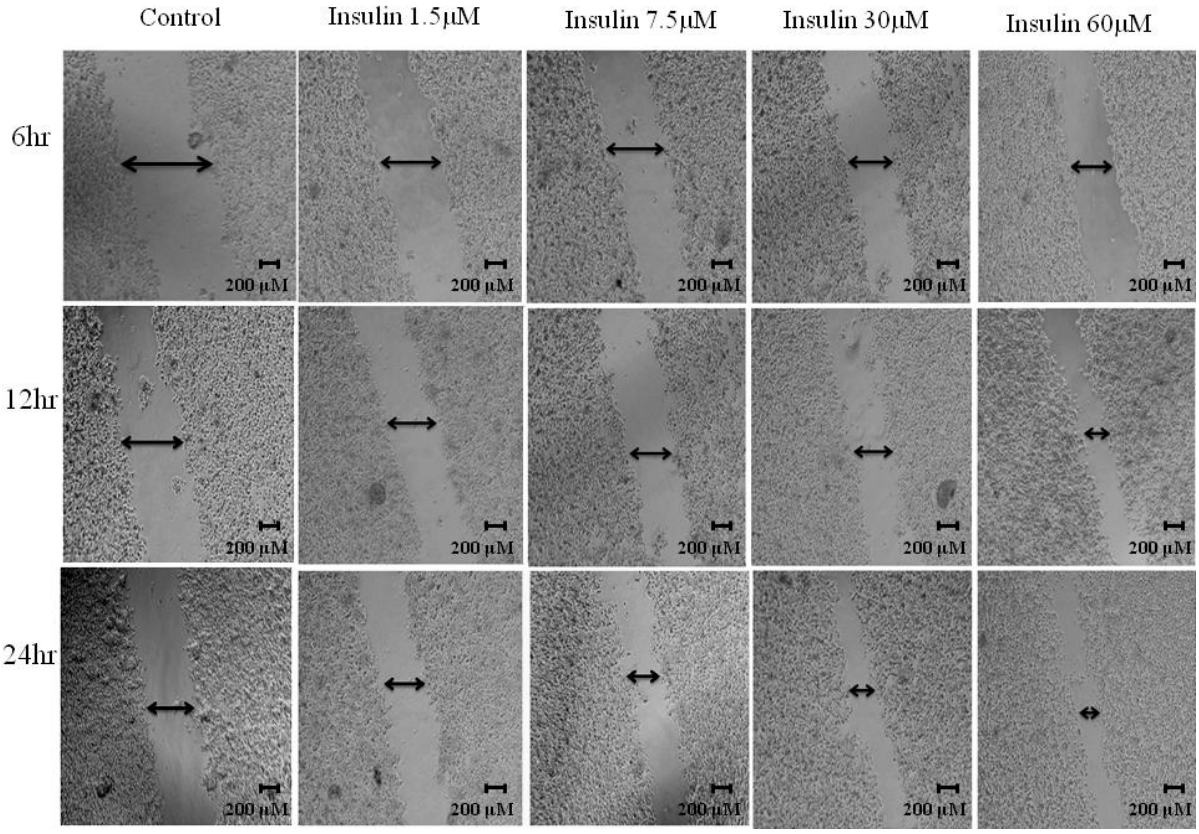

Figure 29: *Insulin treatment for different hours 6, 12, and 24h on HEKa using different concentrations 1.5, 7.5, 30, and 60 µM. The results show that the maximum decrease in wound diameter takes place at the highest concentration (60 µM) of insulin in comparison to the other concentrations.*

With only Zn + I treatment, 1.5 µM concentration treatment, 40.3 ± 1.04%, 26 ± 3.5% and 29.3 ± 3.8% migration, with 7.5 µM Zn + I concentration 44.3 ± 0.74%, 33 ± 0.39% and 43.3 ± 4.83% cell growth enhancement, with 30 µM 46.8 ± 1.1%, 35.9 ± 2.42% and 51.4 ± 2.21% closure of the wound and after 60 µM treatment 48.5 ± 0.76%, 45.1 ± 2.36% and 65.6 ± 1.52% more cell growth enhancement at 6, 12 and 24h respectively in relation to untreated control (**Figure 30**).

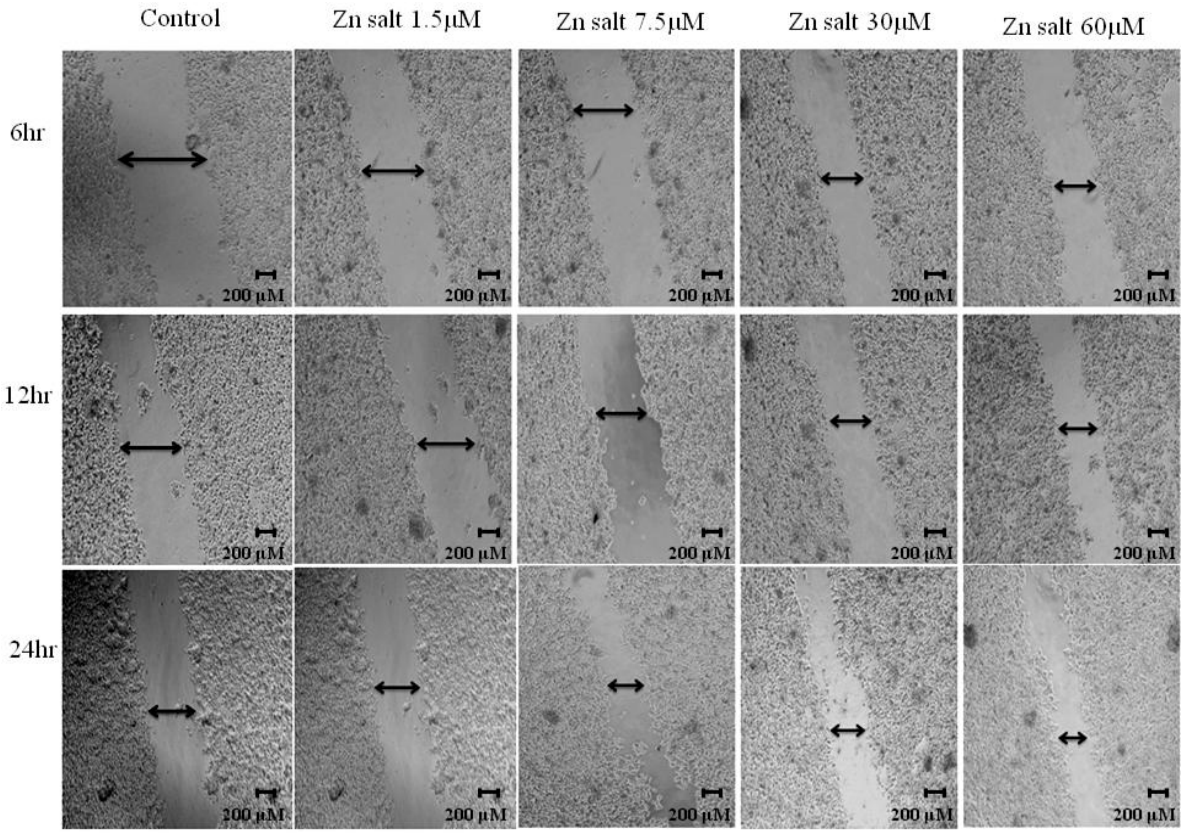

Figure 30: *The wound diameter changes after treatment with Zn salt (7.5, 30, and 60 µM concentrations and 6, 12, and 24h) shows that the Zn salt behaves as a growth factor and helps in enhancing the cell division and maximum decrease in wound diameter takes place at higher concentration of salt.*

At 6h insignificant significant differences were observed in cell migration at any concentrations of IZnQCs in comparison with controls (insulin and Zn) and I + Zn combination. With an increase in time, the effect of migration became more prominent and at 24h a faster wound recovery rates were prominent. At lower concentrations, the difference in wound recovery in comparison with various controls (insulin, zinc, and Insulin + Zn) was distinguished significantly. At 1.5 µM concentrations of IZnQCs about 14% faster healing of the wound was obtained in comparison with insulin or zinc alone or a combination. Insulin, I + Zn combination, and Zn. At 7.5 µM 5% better wound recovery in comparison to insulin and 3% in insulin in combination with Zn were obtained. Similarly, at 30 µM 5% faster recovery and takes place in comparison to insulin whereas no significant change was observed in comparison with I +Zn. At 60 µM IZnQCs treatment 4% firster recovery took place in comparison to insulin and 2% in comparison to I + Zn in combination. The reason for the reduced difference at higher concentrations may lie in the fact that both insulin and

Zinc work through the same pathway and supplement each-others work and therefore, at higher concentrations the cellular signaling strength and recovery rate might have reached saturation. The results are shown in **Figure 31** and **Table 5**.

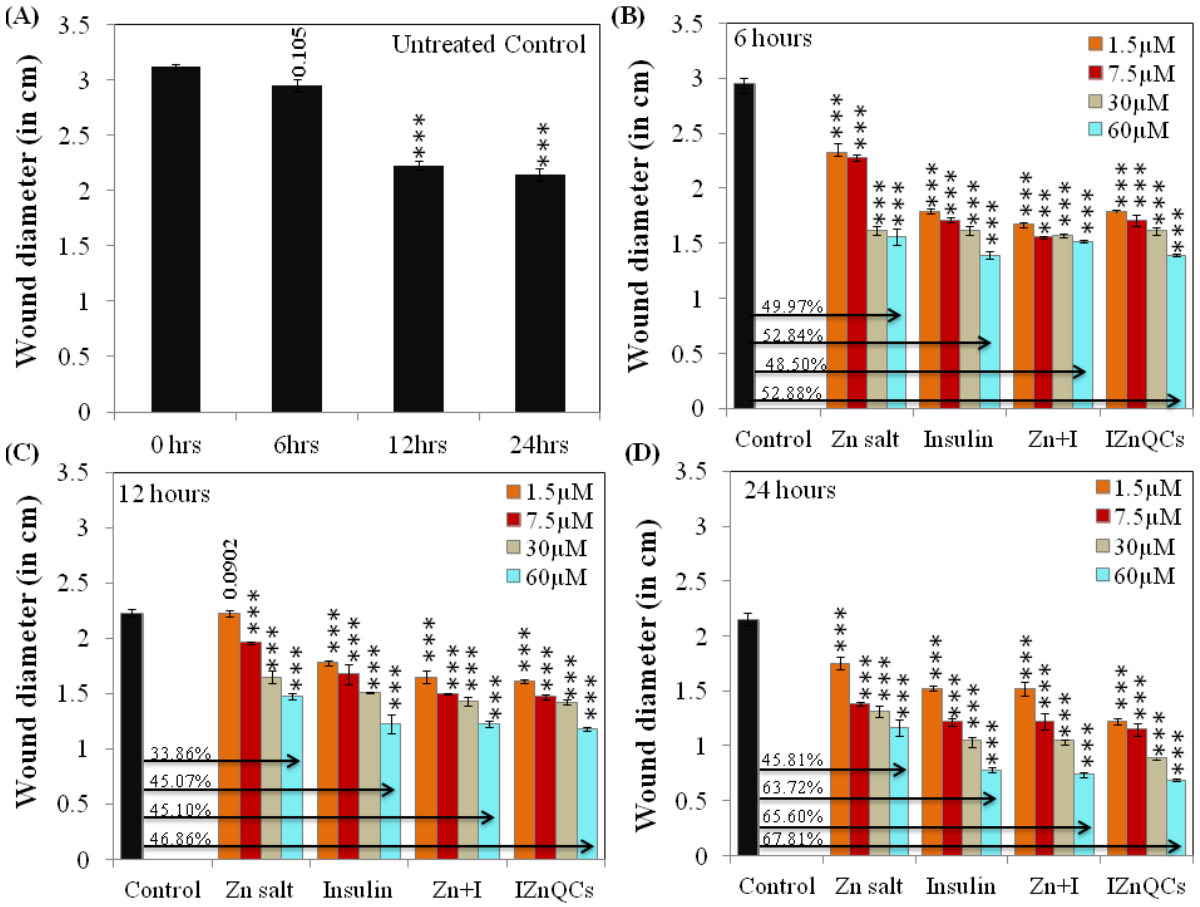

Figure 31: *The wound diameter changes after treatment with Zn salt, Insulin, Zn+I, and IZnQCs (7.5, 30, and 60 µM concentrations and 6, 12, and 24h). The statistical significance of the data shown with "*": *** P<0.001, ** P<0.01, and * P<0.05.*

Both insulin and zinc are known for their wound healing activity by altering the inflammatory dynamic. Insulin binding to IR and phosphorylate the tyrosine kinase receptor for its activity. Zinc is also known to work through the same pathway and in the absence of insulin, the prolonged exposure of Zn leads to the tyrosine phosphorylation present on IR and plays a similar role as insulin. Since both works through IR phosphorylation, a synergistic effect in presence of Zinc in combination with insulin and IZnQCs has been obtained, which leads to faster wound healing.

Table 5: *In vitro time-dependent cell migration/wound recovery assay. After 70-80%, confluence wounds were created in cultured HEKa cells and thereafter were treated with*

IZnQCs along with Zn and insulin control alone or in combinations for 24h, and wound diameter change was calculated from microscopic images. The data represented as mean value ± SD of change in cell migration/wound recovery of three independent experiments.

% of the change in cell migration/wound recovery												
Dose	6 hours				12 hours				24 hours			
	$ZnSO_4$	Insulin	Zn + I	IZnQCs	$ZnSO_4$	Insulin	Zn + I	IZnQCs	$ZnSO_4$	Insulin	Zn + I	IZnQCs
1.5µM	21.18 ± 3.72	39.49 ± 1.61	40.3 ± 1.04	39.49 ± 1.29	0.224 ± 0.030	20.18 ± 1.29	26 ± 3.5	27.58 ± 1.07	18.61 ± 2.49	29.3 ± 1.28	29.3 ± 3.8	43.02 ±1.62
7.5 µM	22.88 ± 1.27	42.03 ± 1.35	44.3 ± 0.74	42.03 ± 3.04	12.11 ± 0.59	24.89 ± 5.17	33 ± 0.39	34.08 ± 1.57	35.58 ± 0.76	41.26 ± 2.03	43.3 ± 4.83	46.51 ±3.38
30 µM	45.25 ± 2.56	45.25 ± 2.50	46.8 ± 1.1	45.25 ± 2.14	26.01 ± 3.49	32.51 ± 0.38	35.9 ± 2.42	36.32 ± 1.63	39.07 ± 2.86	51.39 ± 3.22	51.4 ± 2.21	58.6 ±0.72
60 µM	49.97 ± 4.69	52.84 ± 2.49	48.5 ± 0.76	52.88 ± 0.83	33.86 ± 1.96	45.067 ± 7.07	45.1 ± 2.36	46.86 ± 1.46	45.81 ± 5.09	63.72 ± 1.66	65.6 ± 1.52	67.81 ±0.83

4.8.4. Fluorescence imaging

The fluorescence imaging using Dewinter was performed shows fluorescence on the cells as performed by using a confocal microscope (**Figure 32**).

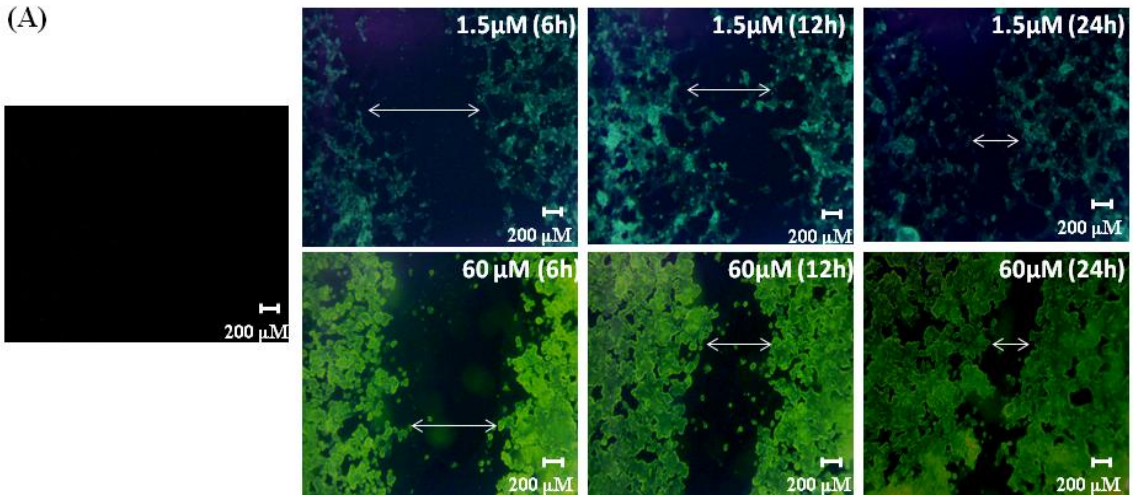

Figure 32: *Promotion and monitoring of wound healing in under phase contrast and fluorescence microscopy using IZnQCs (60 µM).*

4.8.5. Combination index (CI)

To calculate CI; D_m is calculated using m and y from **Figure 33**.

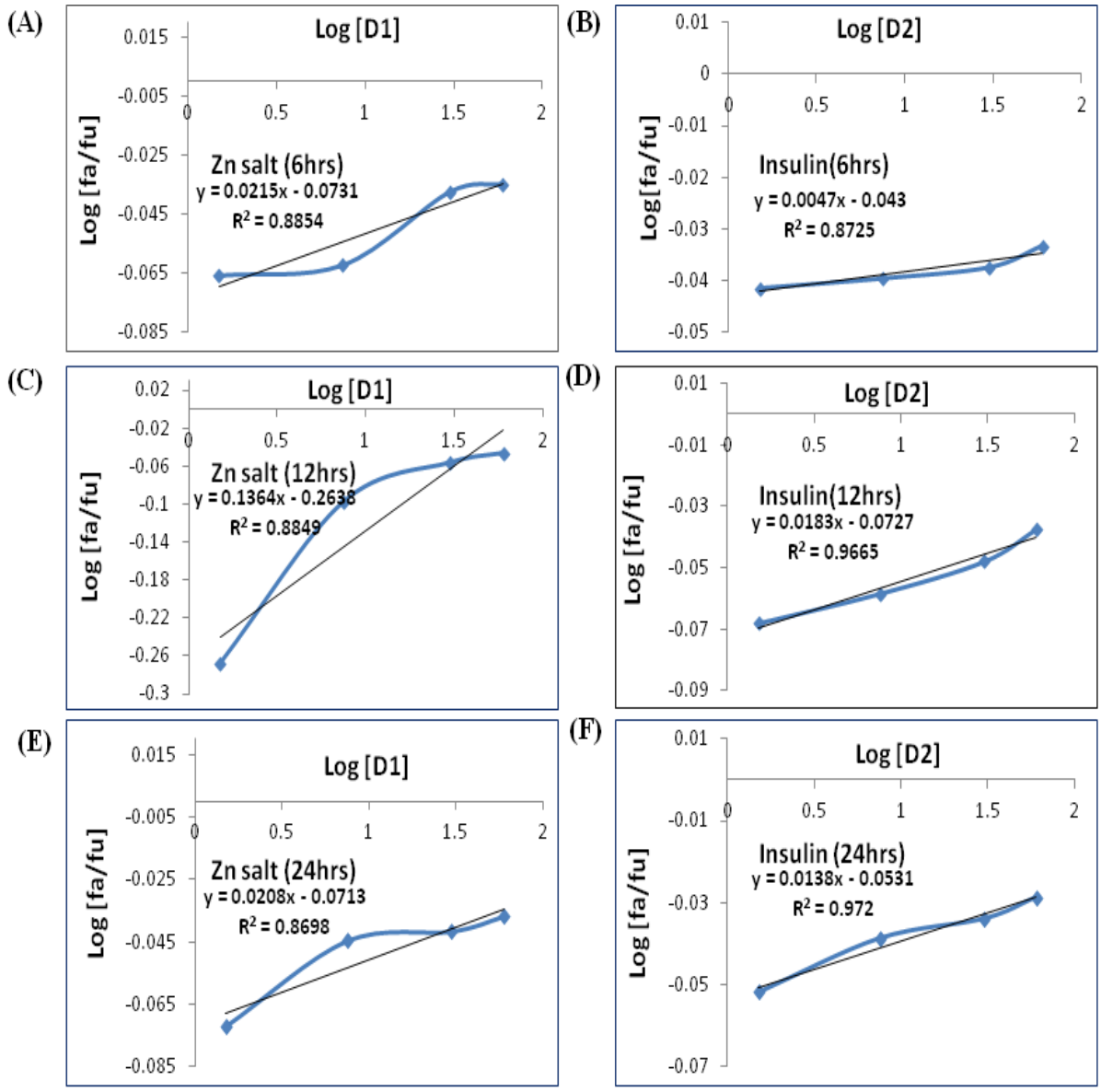

Figure 33: *Median plots of* (A) *Zn salt,* (B) *insulin at 6h,* (C) *Zn salt,* (D) *insulin at 12h and* (E) *Zn salt,* (F) *insulin at 24h for finding y-intercept and m values to calculate* D_m.

As the results of cell viability and cell migration show the faster wound healing by IZnQCs, the calculated CI values of different combinations of insulin and Zn salt are also less than 1 which shows that both behave synergism in which two drugs (insulin and Zn) work together and helps each other in enhancing their activity shown in **Table 6**.

Table 6: *Combination Index (CI) values for cell migration for the different combinations of insulin and Zn salt. The values are less than 1 which shows that both behave synergism in which two drugs work together and helps each other in enhancing their activity.*

	The concentration of Zn salt and insulin	**$(D_x)_1$ (Zn salt) = $D_m[f_a/f_u]^{1/m}$**	**$(D_x)_2$ (insulin) = $D_m[f_a/f_u]^{1/m}$**	**CI = $(D)_1/(Dx)_1$ + $(D)_2/(D_x)_2$**
6 hours	1.5 µM	509.4143	-55394	0.002917
	7.5 µM	430.4253	-39647.8	0.017235
	30 µM	154.0116	-27411.7	0.193696
	60 µM	139.6461	-13706.9	0.42528
12 hours	1.5 µM	3.54E+20	1005.052	0.001492
	7.5 µM	22316.58	591.5453	0.013015
	30 µM	392.042	349.0659	0.162466
	60 µM	117.3233	217.0042	0.614857
24 hours	1.5 µM	3.54E+20	1005.052	0.001492
	7.5 µM	22316.58	591.5453	0.013015
	30 µM	392.042	349.0659	0.162466
	60 µM	117.3233	217.0042	0.614857

4.9. Conclusions

In the case of complicacy in recovery, the surgeon needs to reopen the surgical wounds to monitor the condition which decreases the life quality and increases the healthcare expense. Therefore, the development of a suitable tool is necessary which will selectively bind to the wound site and will help to monitor the progress of wound recovery. Insulin not only reduces blood glucose concentration but also modulates inflammation and thereby promotes cellular growth. Therefore, a significant increment of insulin-like growth factor-1 receptor (IGFR-1) is has been observed at the various wound sites.[268,269] This allows specific targeting of the insulin-like growth factor or insulin or their formulations to the wound site.[270] Recently the Zinc oxide nanoparticles (ZnONPs) and metal quantum dots have gained attention for their easy synthesis procedure, biocompatibility, stability, and wide range of applications including antibacterial and rapid wound healing activities.[271,272] This work demonstrates the role of Zn-insulin quantum clusters in the promotion of recovery of the wound and allows monitoring of the same as well. In IZnQCs both insulin and zinc showed a synergistic effect through

targeting IR and phosphorylating the same. Although, at all concentrations, the synergism is present the most prominent effect was observed at 1.5 µM, IZnQCs dose. The phenomenon perhaps may explain by the fact that prolonged exposure of Zn, in the absence of insulin, can cause phosphorylation of tyrosine present on IR (insulin receptor) and plays a similar role as insulin (**Figure 34**). Therefore, at low dose influence of IZnQCs are much larger than insulin or zinc alone or in combination but at higher doses both insulin as well Zn alone may generate a response for healing up to saturation. Wound healing promotional activity, target specificity, and fluorescence properties make the IZnQCs (**Figure 34**) ideal to use as wound recovery promoting as well as a monitoring tool. Further, the investigation is needed to translate this formulation into pre-clinical and clinical models.

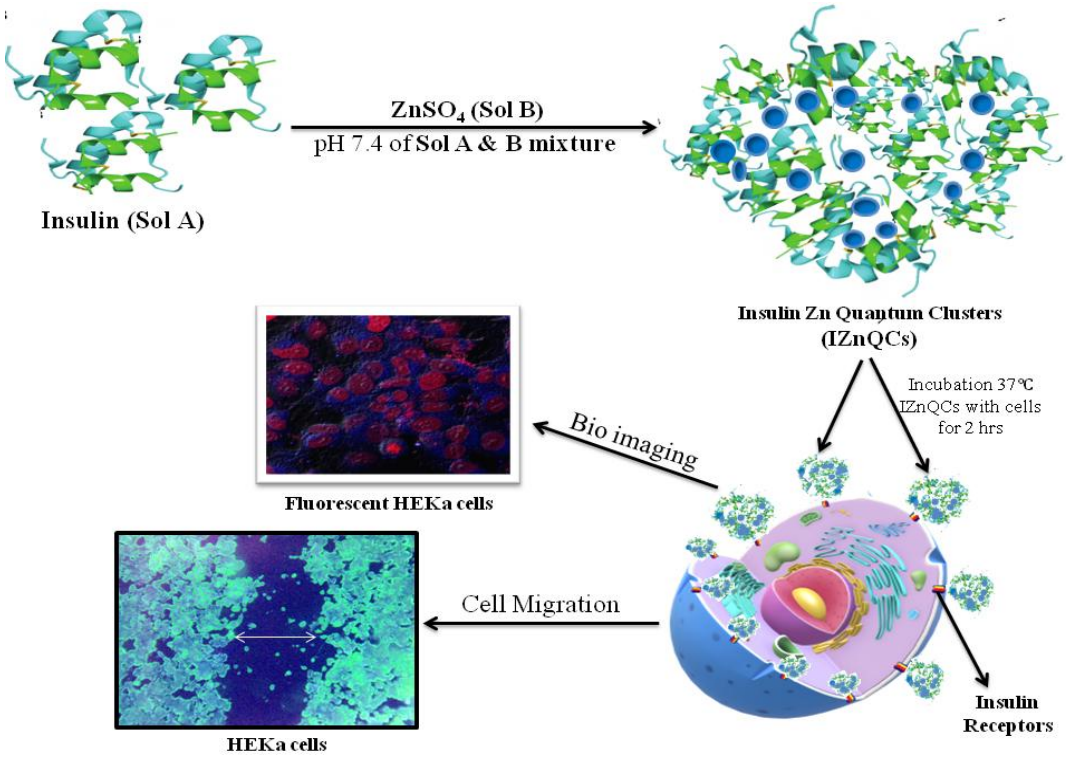

Figure 34: *Shows the binding of insulin zinc quantum (IZnQCs) with the insulin receptors present on the cell membrane. IZnQCs accelerate cell migration, helps in wound healing, and also monitoring the migration of the cells.*

CHAPTER 5
CRYSTALLINE INSULIN COPPER QUANTUM CLUSTERS

5.1. Abstract

Protein embedded fluorescence quantum clusters (QCs) have received a great amount of interest among researchers because of their high aqueous solubility, stability, cost efficiency, and target specificity. Considerable advancement has happened in making functional quantum clusters with target specificity. This work reports the simple synthesis of insulin protected copper quantum clusters (ICuQCs) and their receptor-targeted bioimaging applications (**Figure 35**). The preparation of copper quantum clusters (CuQCs) was done simply by a one-pot synthesis method by changing the pH of the insulin protein firstly to 10.5 basic pH than physiological pH. At physiological pH, the mixture incubated in oven 37C at 240 rpm has been developed to process initially polydisperse, non-fluorescent, and unstable CuDs into monodispersed (~2 nm), highly fluorescent, and extremely stable ICuQCs in the same phase (aqueous) using insulin as protein. HRTEM images show a uniform distribution of CuDs within the protein matrix. Metal ion binding site prediction and docking server (MIB) results show that chain B of insulin contains 3 templates contains 5 amino acid residues which bind with Cu^{2+} metal ion. Groove 1 contains GLY8 and HIS10 bind has the highest binding potential towards Cu metal ions. Because of the protein protection, coupled with direct synthesis and easy functionalization, this hybrid QC protein system is expected to have numerous optical and bioimaging applications in the future.

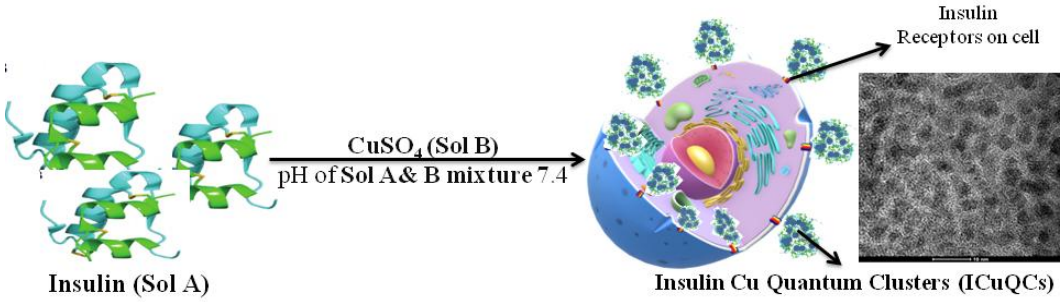

Figure 35: *Schematic presentation of the formation of crystalline insulin copper quantum clusters (ICuQCs).*

5.2. Introduction

Metal quantum clusters have attracted research interest for their one of a kind part in connecting the "missing gap" amongst nuclear and nanoparticle conduct in metal.[273,274] These QCs are comprised of just a couple to a few many atoms with a size littler than 1−10 nm,

have risen as an intriguing sort of luminescent nanomaterials.[275,276] Contingent on the number of atoms present in the QCs when their sizes wind up practically identical to the Fermi wavelength they show optical, electric, charge properties, and tunable fluorescence wavelength.[277,278] The QCs have enhanced photo-stability; large Stokes shift, as well as high emission rates, and strong luminescence.[279,280] The QCs may be synthesized by using a reducing agent like $NaBH_4$ and by changing the pH at basic pH the amino acids having aromatic groups donate electrons for the reduction of metal and the disulfide bonds play important role in stabilizing the nucleated cluster.[281,282]

Different metal quantum clusters have been prepared using various proteins (e.g. egg white, Human serum albumin, Trypsin, insulin, etc) and metal (e.g. Au, Ag, Fe, Pt, Cu, etc) and been explored for their applications such as ion sensing and quantification, redox sensing, bioimaging, etc.[283-298] H. Wei and coworkers, H. Kawasaki and coworkers, and J.M. Liu and coworkers have used various proteins (such as Lysozyme, Pepsin, Trypsin, Bovine Serum Albumin) to prepare metallic quantum clusters showed the use of gold-protein quantum clusters of Au for the sensing of Hg^{2+}, Cu^{2+}, Pb^{2+}.[283-286] D. Joseph and coworkers, H. Shi and coworkers, Y. Chen and coworkers and P.L. Xavier and coworkers have used proteins like ovalbumin, papain to prepare protein-metal quantum clusters to sense metal ions like Hg^{2+}, cupric ions respectively and egg white used for making quantum clusters. [288-290] Lactotransferrin @ AuQCs has been used for metal ions such as Cu^{2+}, Ag^{+}, Ca^{2+}, Ni^{2+}, Co^{3+}, Fe^{3+} and Zn^{2+}.[291] Horseradish peroxide-Au quantum cluster has been used for H2O2 sensing.[292] Human Serum Albumin-Au quantum cluster has been used for Nitric Oxide (NO) sensing.[293] Bovine Serum Albumin (BSA) in combination with various metal ions such as Ag, Au, and Cu has been used for bioimaging applications both in vitro and in-vivo imaging.[294,295] Insulin gold quantum clusters were prepared to find the increased in the number of receptors when myoblast cells transformed from undifferentiated to differentiated myoblast cells.[296,297] Nanoclusters of gold Insulin were prepared and used for super-resolution microscopy, to detect the fluorescence and stimulated emission depletion properties of gold nanoclusters.[298]

One of the most attractive features is its great biocompatibility and amazing photostability, combined with low toxicity levels. Due to lower levels of harmfulness and excellent photostability, the QDs become attractive in bio-imaging testing. Here in this chapter, we synthesized ICuQCs using the simplest method[299] to check the binding of Cu @ insulin QCs with the insulin receptor. The procedure was performed by blending the metal particle antecedent with insulin and changing it to soluble pH. It is accounted for those

fragrant amino acids that give electrons to diminish metal particles of Cu while broken disulfide bonds assume a real part in balancing out the nucleated bunch. Utilizing this simple synthesis we can process polydisperse Copper sulfate ($CuSO_4$) into great degree fluorescent metal quantum-clusters, stable in aqueous medium connected with insulin as layout.[300] Colloidal stability was determined by analyzing the Zeta potential of the system. The interactions between Cu and insulin have been was determined by FTIR studied and modeled using the bioinformatics tool. The interactions of the protein with metals largely depend on the structure and the sequence (available interacting groups) of the protein. Also, the interactions may modulate the physiological activity of the protein it binds to. Hence, there is a requirement to predict the site of interaction of metal ions in a protein to determine the ultimate possible role in the protein function. Metal ion binding site prediction and docking server (MIB) is an online docking server tool that is used to predict the binding site of various transition metal ions.[301] It is based on the principle of fragment transformation method and focuses on aligning the target protein with various templates containing metal ion binding sites in the database and hence assigning the docking score to each amino acid of the protein as well as the different grooves for metal ion binding.[302] The alignment of the target protein with different templates is compared using the similarity between the structures and their sequences. The structural similarity between them is determined by the BLOSUM62 Substitution matrix and the sequence similarity is determined using the root mean square deviation of the C-alpha of the two structures.[303] This online tool provides an approach with much accuracy of 94.9 % and a sensitivity of 85.6% for Cu^{2+}.[301] In case the binding score is more than the threshold, then that particular residue is known to the binding site for the metal ion. Hence, the binding site of the metal ion was determined.

5.3. Material and methods

5.3.1. Materials

Human recombinant insulin was purchased from Elli Lilly 70/30 human insulin, France. Molecular Biology grade Copper Sulphate was purchased from Sigma Aldrich, USA. Ham's F12 (AL106A), DMEM-F12 media (AL219A), New born calf serum (RM10437), and Phosphate buffered saline pH 7.4 (PBS, TL1099), 100 X Penicillin-streptomycin mixture, were purchased from Himedia Lab, India. All the other chemicals including Sodium hydroxide, Hydrochloric acid, Sodium bicarbonate, etc were of molecular biology grade and were purchased from, Loba Chemie, India. Human cervical carcinoma cell line (HeLa;

ATCC CCL-2) and human lung non-small epithelial carcinoma (A549; ATCC CCL-185) were purchased from ATCC and used for *in vitro* studies.

5.3.2. Preparation of insulin quantum clusters with the copper metal

For Insulin copper quantum cluster preparation, 3.47 M fresh insulin was taken and then converted to 1.82 μM and the pH was adjusted to 10.5 using Sodium Hydroxide (SOLUTION A). The Copper Sulphate salt solution of similar molarity (1.82 μM) was prepared (SOLUTION B) and then these two solutions were mixed and the pH was adjusted to physiological pH 7.4 using 0.1 N Hydrochloric Acid. The resulting solution was kept for incubation in a hot air oven at 37°C and 240 rpm for 12h.[304-306]

5.3.3. Instrumentations

After synthesis of insulin linked metal quantum clusters ($CuSO_4$), UV–visible absorbance was measured using (UV 2600 spectrophotometer, Shimadzu) and 4000 μl quartz cuvette with 1 cm path length; it was operated from 200 to 1100 nm. Measurements were observed for a salt solution ($CuSO_4$); insulin metal quantum clusters with incubation and insulin metal quantum clusters without incubation were measured to study the interactions between Insulin and metal quantum clusters. HRTEM (Talos F200S G2, Thermo Scientific) was used for finding the morphology and elemental analysis was performed to detect the elements present in the sample. It was performed by centrifuging the samples at 240 rpm for 10−15 min, later the pellet was thoroughly washed to remove any kind of impurities or unbound metal salt associated with the sample. The pellet was investigated to analyze the elemental constituents in the samples. In addition to HRTEM Electron Dynamic Scattering (HRTEM-EDS) was performed to analyze the percentage of different elements present in the samples. FTIR Spectrophotometer (Agilent Cary 600 series, Australia) was exploited for analyzing the functional groups of the CuQCs. The sample was washed before use and was air-dried onto a glass slide at 37°C. The pellets were formed by mixing the samples with Potassium bromide (KBr). The scan was observed from 4000 cm^{-1} to 400 cm^{-1}.

Fluorescence spectrophotometer Shimadzu RF-6000, Spectro-fluorometer was exploited to determine the binding of insulin to the metal quantum clusters using the CuQCs sample. The fluorescence intensity was measured at an excitation wavelength of 272 nm, coupled with an emission scan from 260 to 520 nm with an excitation and emission slit of 5 mm. The percentage increase in the intrinsic fluorescence; the fluorescence intensities of

ICuQCs and Insulin were compared using the procedure as mentioned in 4.2.3. section of chapter 4.

5.3.4. *In vitro* assay

The biocompatibility, effect of ICuQCs on cell viability and cell migration was determined by using the HeLa cell line.

5.3.4.1. Cell viability

The viability of the cells was checked out on HeLa by using MTT (3-(4, 5-dimethylthiazol-2-yl)-2, 5-diphenyltetrazolium bromide) assay. HeLa of density 1 X 10^4 (per well density) has been seeded in 96 well plates and was allowed to 70-75% confluent. The cells after that were incubated with different percentages (1.5, 7.5, 30, and 60 μM) of ICuQCs, insulin, Cu salt, and the mixture of insulin and Cu salt. After treating the cells were incubated at 37°C in the incubator for 24h. After 24h the MTT (2 mg/ml in 5% ethanol) was added for 3h. After 3h the MTT along with media was removed and 200 μl dimethyl sulphoxide (DMSO) was added to dissolve the formazan crystals. The absorbance was checked at 570 nm. The inhibition % was calculated by using the formula (xvi).

$$\% \text{ inhibition} = [1 - (A_t/A_s) \times 100] \% \text{..... (xvi)}$$

A_t is the test substance absorbance and A_s control solvent absorbance. For every three independent readings were taken [254,255]

5.3.4.2. Bioimaging studies

Laser confocal images were visualized under a (Zeiss LSM 510 Meta, Germany) confocal microscope. To confirm the application of insulin-based quantum cluster for cellular imaging confocal microscopy was performed. Insulin specifically interacts with its cell surface receptor; therefore ICuQCs should also interact with the same cell surface receptor. To confirm that confocal imaging was performed using A549 human lung non-small epithelial carcinoma cell line (CCL-185, ATCC, USA) and HeLa, human cervical cancer cell lines (CCL-2, ATCC, USA). Both A549 and HeLa cells were cultured and maintained Ham's F12 and DMEM media respectively supplemented with 10% serum and antibiotics. After achieving 60–70% confluence the cells were inculcated with 1% ICuQCs or Insulin (in control) for 2h in normal culture conditions. After incubation cells were thoroughly washed with 1X PBS and fixed with methanol. Thereafter cells were treated with RNase A for 3h at 37°C. Thereafter cells were incubated with 1 μg/ml of propidium iodide (PI) before imaging.

Dewinter fluorescence microscope. For taking the images, the A549 (Lung cancer cell line) cells were treated with ICuQCs and fixed with 2% formaldehyde. The cells were examined in white light and fluorescent light.

5.3.4.3. Statistical analysis

By using one-way ANOVA statistical analysis of data was carried out using MS Excel. Then the corresponding *P*-value was measured to check the statistical significance of the data. Data were presented as the mean ± SD of at least three independent experiments.

5.3.5. Bioinformatics

MIB is an online docking server tool that is used to predict the residues of binding sites in various transition metal ions using the fragment transformation method. In the fragment transformation method, the metal ion-containing template protein structure (T) of length m extracted from the protein data bank (PDB) and query protein (S) of length n residues were aligned, based on this alignment the metal ion binding template can be transformed into the query protein structure. For these protein structures, some parameters were applied. The important parameter was template must contain residues bound with Mg^{2+}, Ca^{2+}, Mn^{2+}, Zn^{2+}, and Fe^{3+} metal ions. Secondly, the protein structures which did not possess polypeptide are excluded and the length of the polypeptide chain must be 50 residues.[307] The residues of query template and metal ion binding triplets can be represented by N-Cα-C backbone atoms and are given by (xN, xCα, xC) and (yN, yCα, yC); x and y are the coordinates of PDB. In terms of triplets, S and T can be represented as (τ1, τ2.. τm) and (σ1, σ2..σm). For the m x n dimensions of S and T, residues matrix was constructed forms a transformed matrix Mij means σi = τj or Mijσi = τj. Different Mij has three translations and rotations along the x, y, and z Cartesian axes. The third parameter is that the distance between the metal center and PDB coordinates was within 3.5°A and the template must contain at least two metal ion binding residues. The Cartesian distance between the S and T (τl and Mij.σk respectively) was represented by Dkl ij which provides the similarity in the orientation of S and T residues. If the distance between two triplets (σi, τj) and (σk, τl) is less than Do (3.5°A) only then alignment was possible.[308] The other parameter was the binding score of the residue denoted by Ci must be higher than the specified threshold value, the binding score is assigned to all the residues of the target protein-based based on structural conservation of the protein as well as the sequence of the target protein with the help of root mean square deviation of C-alpha carbons of structural local alignment as well as BLOSUM62 substitution matrix. If the

binding score is more than the threshold, then that particular residue is known to the binding site for the metal ion.[302,309] Hence, the binding site of the metal ion was determined using the bioinformatics tool. This user-friendly online tool provides an approach with much accuracy of 94.9% and a sensitivity of 85.6% for Cu^{2+} based on the fragment transformation approach. Human Insulin protein was extracted from the PDB database (PDB ID: 4EWW). This polypeptide contains 2 chains. In this tool, the Cu^{2+} metal ion was docked with both the chains of human insulin independently. Different metal ion binding templates are compared with the target protein. Different metal ion-binding templates are compared with the target protein.[303]

5.4. Absorbance spectra and fluorescence spectra

Single Sharp resonance peak of insulin appears at 284.7 nm without $CuSO_4$ having absorption maxima 0.0926. After 48h of incubation of insulin with a metal salt, the absorption peak at 285.7 nm with absorption maxima 0.1985 (**Figure 36A**) was observed due to the formation of quantum clusters of Cu-metal. Further different characterizations were performed to confirm the synthesis of ICuQCs.[310] The changes in internal fluorescence of insulin were monitored by using Shimadzu RF-6000, Spectro-fluorometer, at 272 nm excitation wavelength. The spectral changes were monitored from wavelength 260-520 nm. Approximately 250.4% increase in intrinsic fluorescence of insulin takes place after incubation with $CuSO_4$ after 12h incubation at standardized conditions shown in **Figure 36B**.

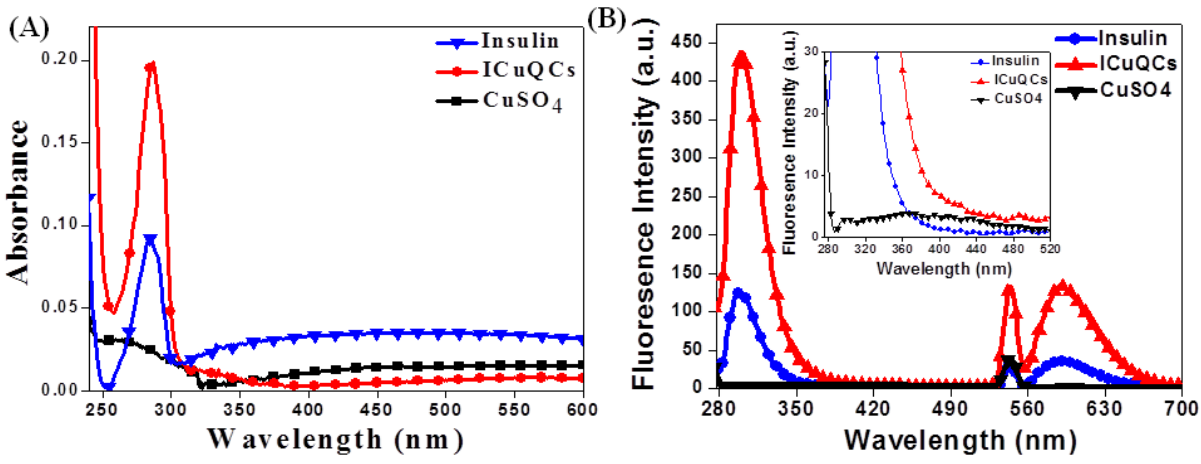

Figure 36: *Absorption spectra show the broader peak of insulin at 272 but after incubation* (A) *ICuQCs show absorption spectra with a maximum at 272 nm.* (B) *Shows the fluorescence spectra after excitation of Insulin, $CuSO_4$, and ICuQCs wavelength 272 nm and emission spectra after excitation at 272 nm show fluorescence intensity at 300 nm.*

5.5. Structure and composition of metal insulin clusters

The DLS sizes show the hydrodynamic diameter of insulin capped quantum clusters (ICuQCs), which is 146.5±100 nm. Transmission electron microscopic images of ICuQDs show the formation of CuDs which are spherical and the selected area electron diffraction (SAED) confirming the presence of copper in the ICuQDs **Figure 37**.

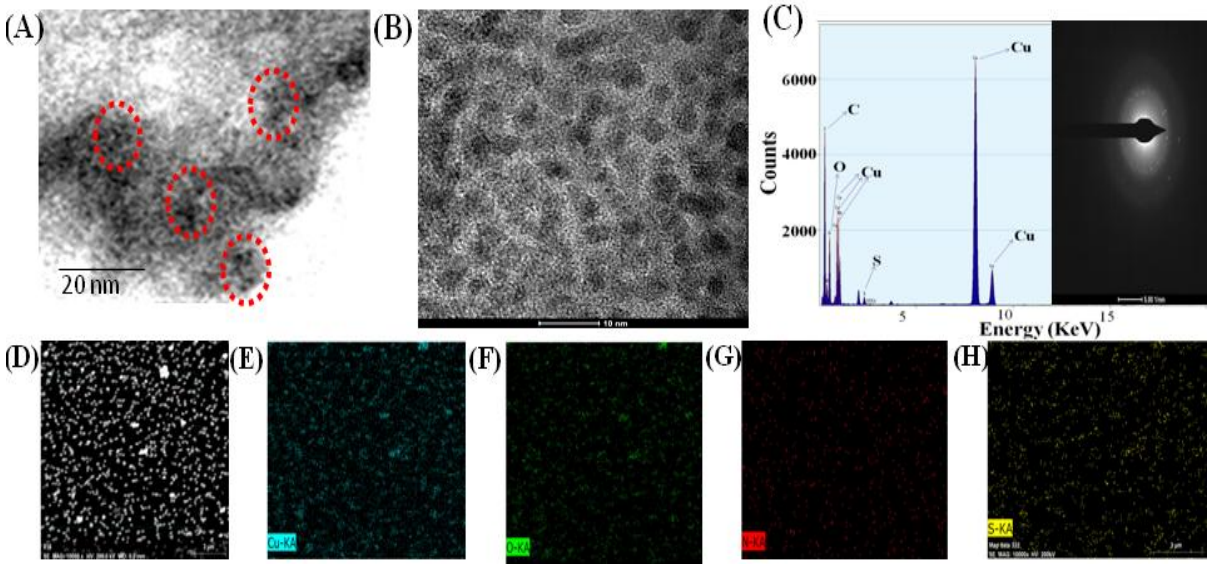

Figure 37: (A) *TEM micrograph indicating the formation of Cu-insulin quantum clusters,* (B) *HRTEM images on 10 nm scale showed the ~2 nm size of ICuQCs,* (C) *HRTEM-EDS indicates the presence of Cu in the quantum clusters and the selected area electron diffraction (SAED) confirming the presence of copper in the ICuQDs,* (D) *shows the area used for elemental analysis,* (E–H) *showed the presence of different elements in the sample.*

Figure 37A. Although the CuDs are distributed all over the protein matrix they are arranged in small clusters. In some of the CuDs are marked in red circles. High-Resolution Transmission electron microscopic images (HRTEM) of the same sample show the cluster size of ~2−3 nm **Figure 37B**. HRTEM-EDS indicate the presence of a significant amount of Cu in the quantum clusters (**Figure 37C**). The diffraction pattern in the selected area electron diffraction (SAED) confirmed the presence of Cu in the ICuQDs (**Figure 37C**). Elemental mapping of area (**Figure 37D**) showed the presence of different elements like Cu, O, N, and S in **Figure 37E-H**. **Figure 37B** is showing low-resolution images of the ICuQDs whereas the inset is showing the EDS spectral pattern of the sample. **Figure 37E-H** Elemental mapping of the cluster showed even distribution Cu in the sample and association of the protein as well.

5.6. FTIR spectra

An FTIR measurement of $CuSO_4$, control insulin, and ICuQCs was carried out to find out interactions involved in metal-protein. The comparative plot is represented in **Figure 38A**.

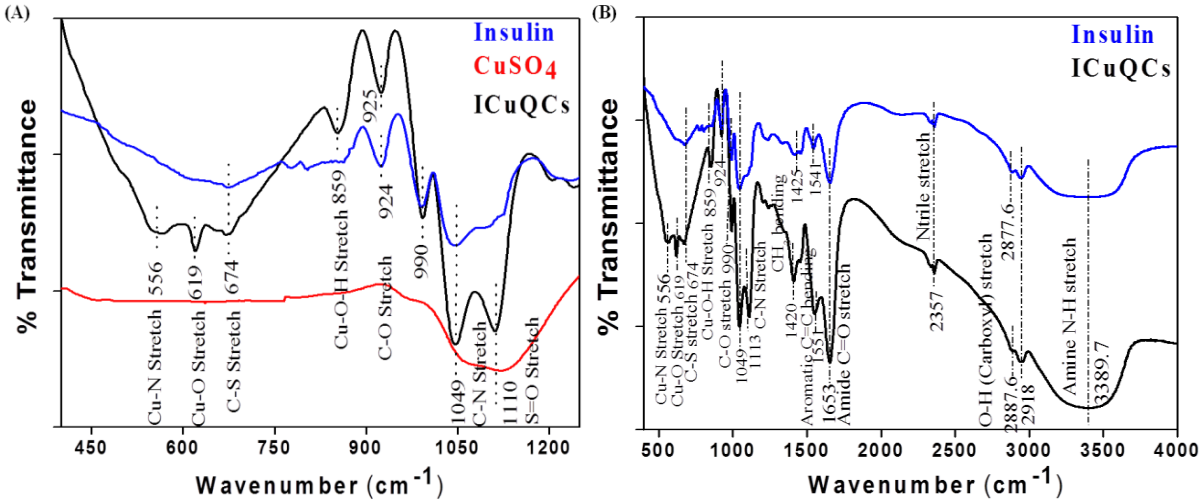

Figure 38: *Comparative FTIR peaks between $CuSO_4$, insulin, and ICuQCs* (A) *in the range of 1250-400 cm^{-1} showed the formation of Cu-N, Cu-O, and Cu-OH bonds in ICuQCs after the formation of quantum clusters.* (B) *Comparative spectra between insulin and ICuQCs.*

Here the peaks due to intermolecular interaction between Cu with insulin the peaks appeared at 619 cm^{-1} and 859 cm^{-1} for Cu-O and Cu-OH respectively.[311] In addition to these two peaks formation of 556 cm^{-1} peaks confirmed interactions of Cu-N in ICuQCs.[312,313] Further for both insulin and ICuQCs band appeared at 674 cm^{-1} for C-S stretch.[315] C-O appeared at 924 cm^{-1} for insulin and at 920 cm^{-1} for ICuQCs. The amide C=O showed peaks of 1653 cm^{-1} ICuQCs is similar to insulin.[314] Furthermore, conformational changes in insulin protein structure due to the interaction of CuDs were monitored using FTIR from 400−4000 cm^{-1} and represented in **Figure 38B**. The peak at 1425 cm^{-1} and 1420 cm^{-1} appeared due to CH_3 bending and at 1541 cm^{-1} and 1551 cm^{-1} because of aromatic C-C bending in insulin and ICuQCs respectively.[316] No shift in peak position was observed at 2355 cm^{-1} for nitrile stretch.[317] Carboxyl O-H stretch peaks formed at 2918 cm^{-1} and 2877.6 cm^{-1} in insulin got shifted to 2918 cm^{-1} and 2887.6 cm^{-1} in ICuQCs. No shift of amine N-H stretch (3389.7 cm^{-1}) was observed in both in both ICuQCs and insulin.[316] The C-N stretch peak at 1049 cm^{-1} is common in both ICuQCs and insulin and similarly, $CuSO_4$ salt solution and ICuQCs show the common peak of S-O stretch at 1110 cm^{-1} shown in **Figure 38A**.[318] The comparative wave number values are represented in **Table 7**.

Table 7: *Comparative table showing the peak position of different functional groups present in $CuSO_4$, insulin, and ICuQCs.*

Wavenumber (cm^{-1})			
Functional Groups	**Insulin**	**ICuQCs**	**$CuSO_4$**
Cu-N stretch	----	556	----
Cu-O stretch	----	619	----
C-S stretch	674	674	----
Cu-O-H stretch	----	859	----
C-O stretch	924	925	----
C-N stretch	1049	1049	----
S=O stretch	-----	1110	1110
Amide C=O stretch	1653 1541	1653 1551	----
Nitrile stretch	2357	2357	----
CH_3 symmetric stretch	2877.6	2887.6	----
CH_3 asymmetric stretch	2918	2918	----
Amine N-H stretch	3389.7	3389.7	----

5.7. Metal ion binding residue templates

The metal ion binding site was determined using the Metal Ion-Binding site prediction and docking server. The server generates templates that contain residues that bind with metal-ion. In the case of chain A insulin receptor, no templates were generated which signifies that the chain does not contain the copper-binding site. On the other hand, chain B contains 3 templates containing 5 amino acid residues which bind with Cu^{2+} metal ion. **Figure 39** shows various local structures that contain residues binding with metal ions within a radius of 3.5Å from the center of the metal ion. Groove 1 contains metal ion binding with GLY8 (glycine) and HIS10 (histidine). Groove contains metal ion binding with HIS5 and HIS10, Groove 3 contains metal ion binding with HIS5, CYS7 (**Figure 39A-C**). These different grooves have different binding potential with groove 1 showing more binding potential, groove 2 having the intermediate binding potential, and groove 3 having the lower binding potential among all (**Figure 39D**, **E** and **F**). In addition to this, the difference in the binding potential was found to be closely related to the distance between the amino acid residue in the groove and the metal ion. In groove 1, the distance between the metal ion and GLY8 and HIS10 was 2.64 Å and 2.07 Å respectively. In groove 2, the distance between the metal ion and ASN3 and HIS5 was found to be 6.38 Å and 5.31 Å respectively. In groove 3, the distance of metal ion from

amino acid residues HIS5 and CYS7 were found to be 4.78 Å and 5.77 Å respectively (**Figure 39E-G**).

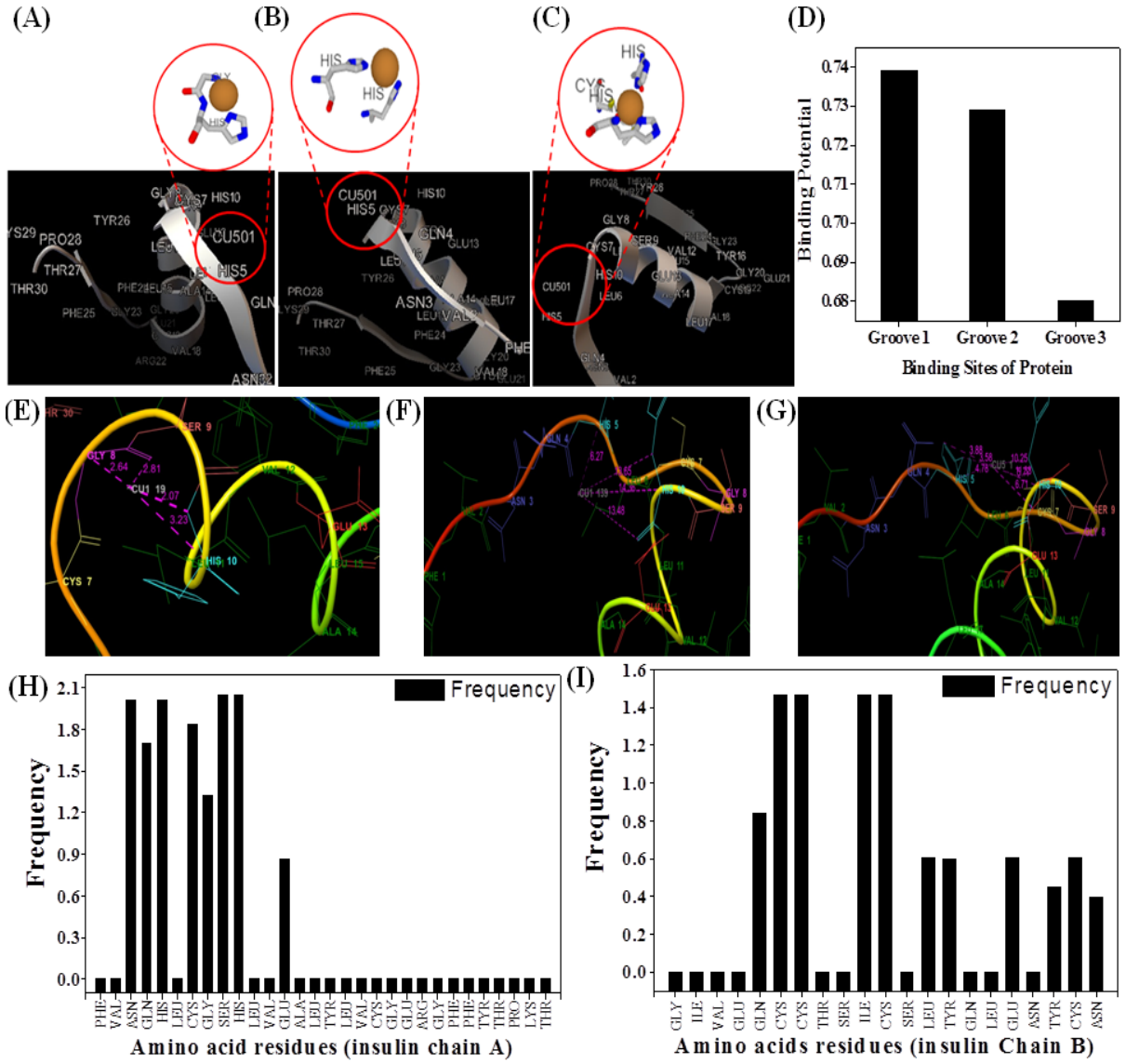

Figure 39: *Metal ion binding residues depicts different binding sites of Cu in insulin chain B along with the amino acid residues within 3.55 Å diameter* (A) *in Groove 1,* (B) *Groove 2, and* (C) *Groove 3, and* (D) *Binding potential of each groove with the Cu-ion.* (E-G) *Showed the distance of Cu-ion from each functional group of amino acid residue.* (H) *and* (I) *shows amino acid binding score more than the threshold value in chain A and chain B of insulin respectively.*

5.8. *In vitro* studies

5.8.1. Cell viability and fluorescence imaging

Figure 40 shows the non-toxic behavior of Insulin Copper Quantum clusters (ICuQCs). The insulin behaves as a growth factor and helps in cell proliferation. Similarly, Cu promotes cell growth helps in cell division. 5% concentration of ICuQCs showed an almost double increase in the growth of cells in 24h when these were compared to control (blank, insulin and insulin+Cu salt) indicates the cell growth-promoting effect of ICuQCs

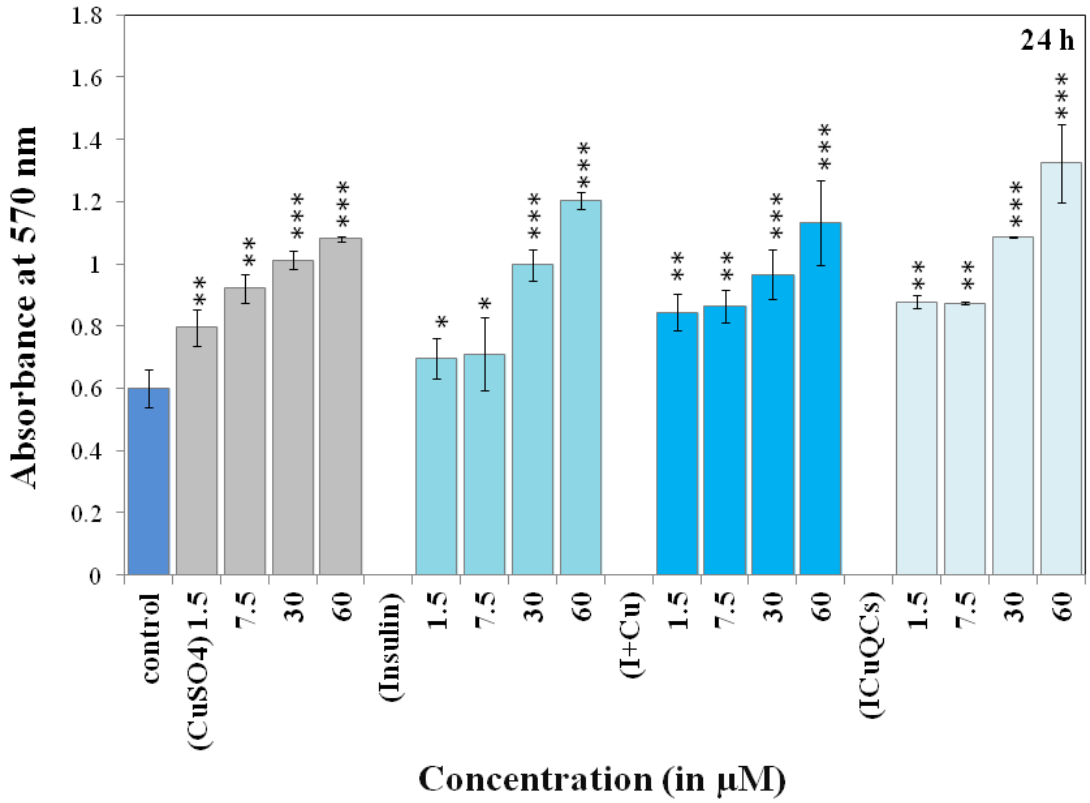

Figure 40: *HeLa cell viability/ proliferation in the presence of Cu salt, insulin, insulin Cu salt, and ICuQCs shows the nontoxic effect of all samples. Further insulin is known for growth-promoting activity which is true for Cu as well. Therefore, in the presence of insulin, Cu or combination showed higher cell proliferation. The statistical significance of the data shown with "*": *** P<0.001, ** P<0.01, and * P<0.05.*

Figure 41 showing the images are for fluorescence imaging using the A549 cell line. To check the fluorescence of ICuQC cells were treated as before. After treatment, the cells were washed with 1X PBS buffer and fixed using 2% formaldehyde. After fixing the cells were observed under the Dewinter inverted fluorescence microscope. **Figure 41** is showing blue fluorescence only on the cell surface which suggests the specificity of the ICuQCs for the cell surface receptor. The picture was taken by keeping the focus only on the cell membranes. **Figure 41B** is showing the same field focusing on the whole cells.

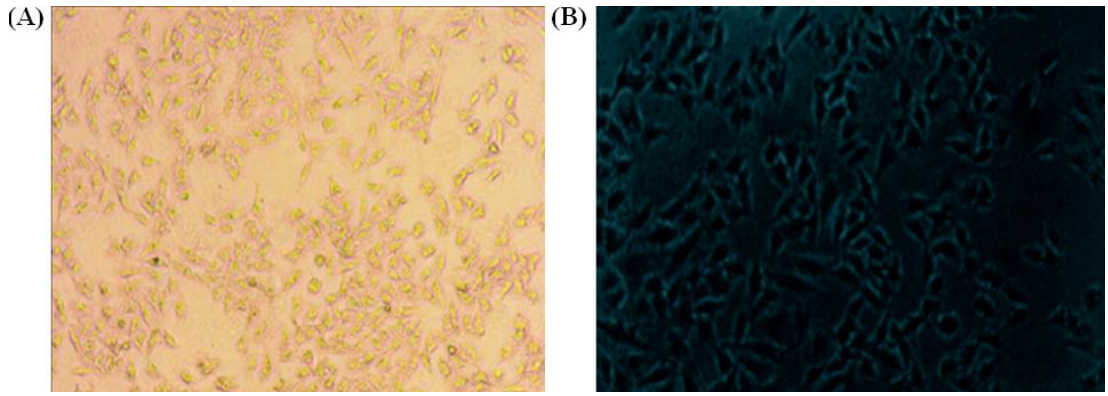

Figure 41: *Fluorescence images on A549 cell line 100X magnification* (A) *show phase image and* (B) *show the presence of fluorescence only the cell membrane.*

5.8.2. Confocal imaging

To confirm the application of insulin-based quantum cluster for cellular imaging confocal microscopy was performed using A549 and HeLa cells.

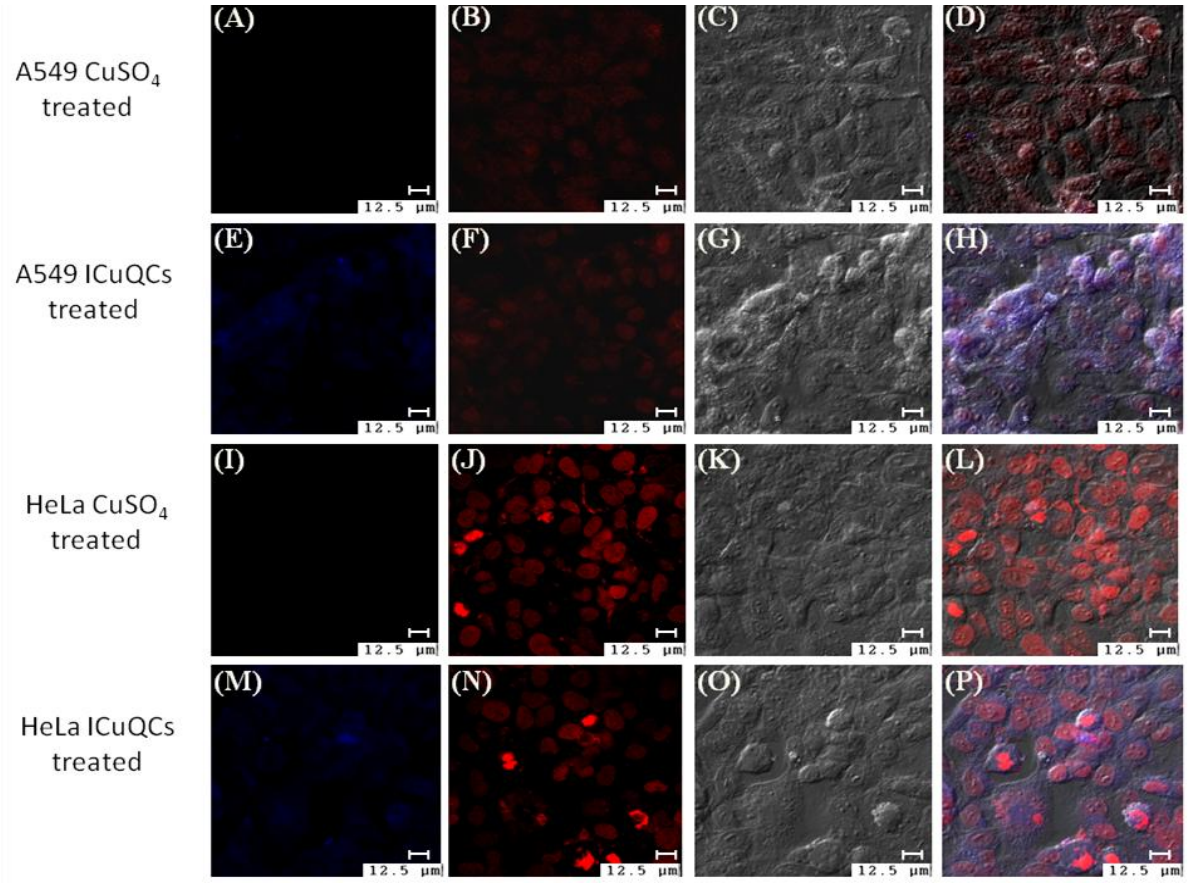

Figure 42: *A549 cells* (A) *treated with $CuSO_4$,* (B) *nucleus stained with PI,* (C) *Phase image of the cell,* (D) *merged imaged of $CuSO_4$ treated and non treated cells,* (E) *treated with ICuQCs,* (F) *nucleus stained with PI,* (G) *Phase image of the cell,* (H) *merged imaged of*

ICuQCs treated and non treated cells and HeLa cells (I) *treated with* $CuSO_4$, (J) *nucleus stained with PI,* (K) *Phase image of the cell,* (L) *merged imaged of* $CuSO_4$ *treated and non treated cells,* (M) *treated with ICuQCs,* (N) *nucleus stained with PI,* (O) *Phase image of the cell, and,* (P) *merged imaged of ICuQCs treated and non treated cells.*

ICuQCs treated both cells showed bright blue fluorescence was observed as a result of the binding of the ICuQCs with the insulin receptors present on the cell surface. **Figure 42A-H** is showing $CuSO_4$ and ICuQCs treated A549 cells. **Figure 42E** is showing the bright blue fluorescence of ICuQCs whereas in **Figure 42A** no fluorescence observed was for the same. **Figure 42A** and **F** are showing the nuclear staining of PI for A549 cells. **Figure 42C** and **G** are showing phase images of the cells and **Figure 42D** and h are showing merged images of the control and treated A549 cells. Similar experiments were performed using HeLa cells. **Figure 42I-P** are showing $CuSO_4$ and ICuQCs treated HeLa cells. **Figure 42M-P** is showing the Blue fluorescence of CuQCs, red of PI, phase and merged images ICuQCs treated HeLa cells respectively. **Figure 42I-L** is showing that of control HeLa cells respectively.

5.9. Conclusions

In this chapter, we synthesized fluorescent ICuQCs. The synthesis was confirmed by performing various studies. The interaction of Cu-metal with insulin protein was confirmed by using TEM micrography, elemental analysis, FTIR, and Metal ion binding site prediction and docking server (MIB). FTIR showed peaks at 556 cm^{-1}, 619 cm^{-1} and 859 cm^{-1} for Cu-N, Cu-O, and Cu-OH respectively indicate the intermolecular interaction between Cu and insulin. Metal protein binding studies show the highest binding potential towards chain B of insulin protein and also has the highest binding potential with Groove 1having GLY8 and HIS10. It was seen that chain A does not show any significant binding with the metal ion whereas the metal ion binds at more than one site in Chain B. In addition to this, the amino acid HIS10 shows the most active and prominent binding with the metal ion in chain B of the Insulin protein. On the other hand, HIS5 in combination with different amino acids forms different binding sites with different levels of binding. It has also been seen through this study that Histidine shows the strongest binding affinity for the metal ion. The reason is that the metal ion binds near HIS in the grooves. Unlike other metal protein quantum clusters, ICuQCs are target specific quantum clusters. Due to the use of insulin in synthesizing the Cu-metal quantum clusters, these ICuQCs showed the property of binding with insulin receptors present on the surface of the cell (**Figure 43**). This target-specific property of these particles

makes these particles different from other quantum clusters. The ICuQCs showed enhanced fluorescence (blue fluorescence) in comparison to control insulin protein due to this enhanced fluorescent property binding of these particles with insulin receptors that can be easily detected by using confocal and fluorescence microscopy (**Figure 43**).

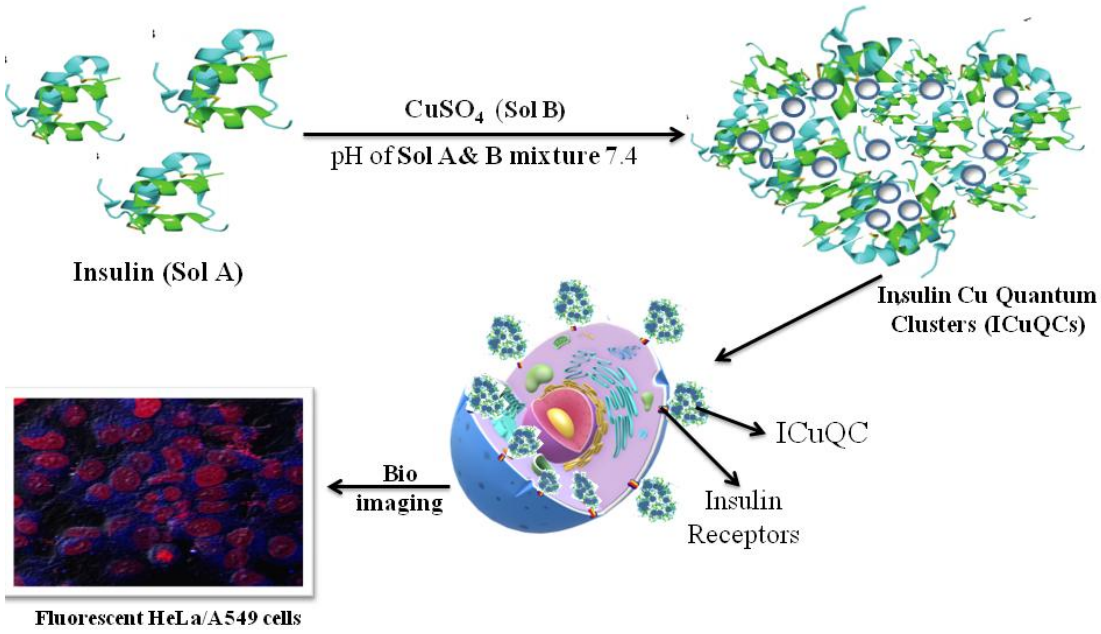

Figure 43: *Shows the binding of insulin copper quantum (ICuQCs) with the insulin receptors present on the cell membrane.*

REFERENCES

1. Diegelmann RF, Evans MC. Wound healing: an overview of acute, fibrotic and delayed healing. *Front Biosci* 2004;**9**:283-89.
2. Friedstat J, Brown David A, Levi B. Chemical, electrical and radiation injuries. *Clin Plast Surg* 2017;**44**:657-69.
3. Frykberg RG, Banks J. Challenges in the treatment of chronic wounds. *Adv Wound Care* 2015;**4**:560-82.
4. Cardona AF, Wilson SE. Skin and soft tissue infections: A critical review and the role of telavancin in their treatment. *Clin Infect* 2015;**61**:69-78.
5. Negut I, Grumezescu V, Grumezescu AM. Treatment strategies for infected wounds. *Molecules* 2018;**23**:2392.
6. Zhao R, Liang H, Clarke E, Jackson C, Xue M. Inflammation in chronic wounds. *Int J Mol Sci* 2016;**17**:2085.
7. Yamada BFA, Santos VLCG. Quality of life of individuals with chronic venous ulcers. *Wounds* 2005;**17**:178-89.
8. Newberg S. Identifying pain and effects on quality of life from chronic wounds secondary to lower extremity vascular disease: An integrative review. *Adv Skin Wound Care* 2018;**31**:102-8.
9. Renner R, Erfurt Berge C. Depression and quality of life in patients with chronic wounds: ways to measure their influence and their effects on daily life. *Chronic Wound Care Manag Res* 2017;**4**:143-51.
10. Strodtbeck F. Physiology of wound healing. *Newborn Infant Nurs Rev* 2001; **1**: 43-52.
11. Khale B, Hermanns HJ, Gallenkemper G. Evidence based treatment of chronic leg ulcers. *Dtsch Arztebl Int* 2011;**108**:231-7.
12. Guo SA, Di Pietro LA. Factors affecting wound healing. *J Dent Res* 2010;**89**:219-29.
13. Larouche J, Sheoran S, Maruyama K, Martino MM. Immune regulation of skin wound healing: mechanism and novel therapeutic targets. *Adv Wound Care* 2018;**7**:209-31.
14. Pecoits FR, Abensur H, Betonico CC, Machado AD, Parente, EB, Queiroz M, *et al*. Interactions between kidney disease and diabetes: dangerous liaisons. *Diabetol Metabol Syndr* 2016;**8**:50.`
15. Sharabi K, Tavares CD, Rines AK, Puigserver P. Molecular pathophysiology of hepatic glucose production. *Mol Aspects Med* 2015;**46**:21-33.

16. Bloomgarden ZT. Diabetic retinopathy and diabetic neuropathy. *Diabetes Care* 2007;**30**:760-65.
17. Asmat U, Abad K, Ismail K. Diabetes mellitus and oxidative stress: a concise review. *Saudi Pharm J* 2016;**24**:547-53.
18. Yach D, Hawkes C, Gould CL, Hofman KJ. Global burden of chronic diseases: overcoming impediments to prevention and control. *JAMA* 2004;**291**:2616-22.
19. Organization WH. *Global report on diabetes*. WHO; 2016.
20. Andersen CA, Roukis TS. The diabetic foot. *Surg Clin North Am* 2007;**87**:1149-77.
21. Frykberg RG, Armstrong DG, Giurini J, Annemarie Edwards D, Marc Kravette D. Steven Kravitz Diabetic foot disorder. *J Foot Ankle Surg* 2000;**39**:S1-S60.
22. Furnary AP, Gao G, Grunkemeier GL, Wu Y, Zerr KJ, Bookin SO, *et al*. Continuous insulin infusion reduces mortality in patients with diabetes undergoing coronary artery bypass grafting. *J Thorac Cardiovasc Surg* 2003;**125**:1007-21.
23. Eming SA, Krieg T, Davidson JM. Inflammation in wound repair: molecular and cellular mechanisms. *J Invest Dermatol* 2007;**127**:514–25.
24. Abrigo M, McArthur SL, Kingshott P. Electrospun nanofibers as dressings for chronic wound care: advances, challenges, and future prospects *Macromol Biosci* 2014;**14**: 772-92.
25. Dhivya S, Padma VV, Santhini E. Wound dressings: a review. *BioMed* 2015;**5**:22.
26. Boateng JS, Matthews KH, Stevens HN, Eccleston GM. Wound healing dressings and drug delivery systems: a review. *J Pharma Sci* 2008;**97**:2892-923.
27. Thu HE, Zulfakar MH, Ng SF. Alginate based bilayer hydrocolloid films as potential slow-release modern wound dressing. *Int J Pharm* 2012;**434**:375-83.
28. Hoffman AS. Hydrogels for biomedical applications. *Adv Drug Deliv Rev* 2012;**64**:18-23.
29. Robson MC. Growth factors as wound healing agents. *Curr opin biotechnol* 1991;**2**:863-7.
30. Pepper MS. Transforming growth factor-beta: vasculogenesis, angiogenesis, and vessel wall integrity. *Cytokine Growth Factor Rev* 1997;**8**:21-43.
31. Herman WH. The economic costs of diabetes: is it time for a new treatment paradigm? *Diabetes care* 2013;**36**:1033-46.
32. Wang N, Liang H, Zen K. Molecular mechanisms that influence the macrophage M1–M2 polarization balance. *Front Immunol* 2014;**5**:614.

33. Werner H, Weinstein D, Bentov I. Similarities and differences between insulin and IGF-I: structures, receptors, and signalling pathways. *Arch Physiol Biochem* 2008;**114**:17-22.
34. Saeedi P, Petersohn I, Salpea P, Malanda B, Karuranga, Unwin N, *et al*. IDF diabetes atlas committee. Global and regional diabetes prevalence estimates for 2019 and projections for 2030 and 2045: results from the international diabetes federation diabetes atlas, 9th edition. *Diabetes Res Clin Pract* 2019;**157**:107843.
35. Cho NH, Shaw JE, Karuranga S, Huang Y, Rocha Fernandas JD, Ohlrogge AW, *et al*. IDF diabetes atlas: global estimates of diabetes prevalence for 2017 and projections for 2045. *Diabetes Res Clin Pract* 2018;**138**:271-81.
36. Singh N, Armstrong DG, Lipsky. Preventing foot ulcers in patients with diabetes. *J Am Med Dir Assoc* 2005;**293**:217-28.
37. Andersen CA, Roukis TS. The diabetic foot. *Surg Clin North Am* 2007;**87**:1149-77.
38. Shoji T, Yoshida S, Mitsunari M, Miyake N, Tsukihara S, Iwabe T, *et al*. Involvement of p38 MAP kinase in lipopolysaccharide-induced production of pro-and anti-inflammatory cytokines and prostaglandin E2 in human choriodecidua. *Am J Reprod Immunol* 2007;**75**:82-90.
39. Morais EA, Chame DF, Melo EM, de Carvalho Oliveira JA, de Paula ACC, Peixoto AC, *et al*. TLR 9 involvement in early protection induced by immunization with rPb27 against Paracoccidioidomycosis. *Microbes Infect* 2016;**18**:137-47.
40. Zheng B, Zhou J, Qu D, Siu K, Lam T, Lo H, *et al*. Selective functional deficit in dendritic cell–T cell interaction is a crucial mechanism in chronic hepatitis B virus infection. *J Viral Hepat* 2004;**11**:217-24.
41. Dinarello CA. Interleukin-1 in the pathogenesis and treatment of inflammatory diseases. *Blood* 2011;**117**:3720-32.
42. http://itsgeniuskey.com/wp-content/uploads/2020/10/IMG_20201009_195619.jpg.
43. Tah B, Pal P, Mishra S, Talapatra GB. Interaction of insulin with anionic phospholipid (DPPG) vesicles. *Phys Chem Chem Phys* 2014;**16**:21657.
44. Sultani M, Stringer AM, Bowen JM, Gibson RJ. Anti-inflammatory cytokines: important immunoregulatory factors contributing to chemotherapy-induced gastrointestinal mucositis. *Chemother Res Pract* 2012.
45. Mayer JP, Zhang F, DiMarchi RD. Insulin structure and function. *J Pept Sci* 2007;**88**:687-713.

46. Whiting DR, Guariguata L, Weil C, Shaw J. IDF diabetes atlas: global estimates of the prevalence of diabetes for 2011 and 2030. *Diabetes Res Clin Pract* 2011;**94**:311-21.
47. Collaboration NRF. Worldwide trends in diabetes since 1980: a pooled analysis of 751 population-based studies with 4·4 million participants. *Lancet* 2016;**387**:1513-30.
48. Demirseren DD, Emre S, Akoglu G, Arpac D, Arman A, Metin A, *et al*. Relationship between skin diseases and extracutaneous complications of diabetes mellitus: clinical analysis of 750 patients. *Am J Clin Dermatol* 2014;**15**:65-70.
49. Qing C. The molecular biology in wound healing & non-healing wound. *Chin J Traumatol* 2017;**20**:189-93.
50. Stem MS, Gardner TW. Neurodegeneration in the pathogenesis of diabetic retinopathy: molecular mechanisms and therapeutic implications. Curr Med Chem. 2013;**20**:3241-50.
51. Tang Y, Zhang MJ, Hellmann J, Kosuri M, Bhatnagar A, Spite M. Proresolution therapy for the treatment of delayed healing of diabetic wounds. *Diabetes* 2013;**62**:618-27.
52. Vileikyte L. Stress and wound healing. *Clin Dermatol* 2007;**25**:49-55.
53. Chen MC, Meckfessel MH. Autoinflammatory disorders, pain, and neural regulation of inflammation. *Dermatol clin* 2013;**31**:461-70.
54. Sprague AH, Khalil RA. Inflammatory cytokines in vascular dysfunction and vascular disease. *Biochem pharmacol* 2009;**8**:539-52.
55. Maczynska I, Millo B, Ratajczak Stefanska V, Maleszka R, Szych Z, Kurpisz M, *et al*. Proinflammatory cytokine (IL-1β, IL-6, IL-12, IL-18 and TNF-α) levels in sera of patients with subacute cutaneous lupus erythematosus (SCLE). *Immunol Lett* 2006;**102**:79-82.
56. Asgari E, Le Friec G, Yamamoto H, Perucha E, Sacks SS, Kohl J, *et al*. C3a modulates IL-1β secretion in human monocytes by regulating ATP efflux and subsequent NLRP3 inflammasome activation. *Blood* 2013;**122**:3473-81.
57. Latz E, Xiao TS, Stutz A. Activation and regulation of the inflammasomes. Nat Rev *Immunol* 2013;**13**:397- 411.
58. Hu X., Ivashkiv LB. Cross-regulation of signaling pathways by interferon-γ: implications for immune responses and autoimmune diseases. *Immunity* 2009;**31**:539-50.
59. Chen MC, Meckfessel MH. Autoinflammatory disorders, pain, and neural regulation of inflammation. *Dermatol clin* 2013;**31**:461-70.

60. Le Blanc K., Mougiakakos D. Multipotent mesenchymal stromal cells and the innate immune system. *Nat Rev Immunol* 2012;**12**:383-96.
61. Zhang JZ, Liu Z, Liu J, Ren JX, Sun TS. Mitochondrial DNA induces inflammation and increases TLR9/NF-kβ expression in lung tissue. *Int J Mol Med* 2014;**33**:817-24.
62. Gerber S, Moran J, Frelinger J, Frelinger J, Fenton B, Lord E. Mechanism of IL-12 mediated alterations in tumour blood vessel morphology: analysis using whole-tissue mounts. *BJC* 2003;**88**:453-61.
63. Liu M, Guo S, Hibbert JM, Jain V, Singh N, Wilson NO, *et al*. CXCL10/IP-10 in infectious diseases pathogenesis and potential therapeutic implications. *Cytokine Growth Factor Rev* 2011;**22**:121-30.
64. Harsoliya MS, Pathan JK, Khan N, Patel VM, Vyas S. Toxicity of Lps and Opa Exposure on Blood with Different Methods. *Webmed Central TOXICOLOGY* 2011;**2**:WMC001696.
65. Al Sadi R, Boivin M, Ma T. Mechanism of cytokine modulation of epithelial tight junction barrier. *Front Biosci* 2009;**14**:2765.
66. Li YV. Zinc and insulin in pancreatic beta-cells. *Endocr* 2014;**45**:178-89.
67. Leopold Wagner CM, Wormley F. Classical versus alternative macrophage activation: the Ying and the Yang in host defense against pulmonary fungal infections. *Mucosal immunol* 2014;**7**:1023-35.
68. Boucher J, Kleinridders A, Kahn CR. Insulin receptor signaling in normal and insulin-resistant states. *Cold Spring Harb Perspect Biol* 2014;**6**:a009191.
69. Masahiro N, Kishio N. Insulin gene mutations and diabetes. *J Diabetes Investig* 2011;**2**:92–100.
70. Ward CW, Menting JG, Lawrence MC. The insulin receptor changes conformation in unforeseen ways on ligand binding: sharpening the picture of insulin receptor activation. *Bioessays* 2013;**35**:945-54.
71. Mosser DM, Edwards JP. Exploring the full spectrum of macrophage activation. *Nat Rev Immunol* 2008;**8**:958-69.
72. Greenway S, Filler L, Geenway F. Topical insulin in wound healing: a randomised, double-blind, placebo-controlled trial. *JWC* 1999;**8**:526-28.
73. Chen X, Zhang X, Liu Y. Effect of topical insulin application on wound neutrophils function. *Wounds* 2012;**24**:178-84.
74. Azevedo F, Pessoa A, Moreira G, Santos MD, Liberti E, Araujo E, *et al*. Effect of topical insulin on second-degree burns in diabetic rats. *Biol Res Nurs* 2016;**18**:181-92.

75. Li W, Gao F, Kan J, Deng J, Wang B, Hao S. Synthesis and fabrication of a keratin conjugated insulin hydrogel for the enhancement of wound healing. *Colloids Surf B* 2019;**175**:436-44.
76. Li X, Liu Y, Zhang J, You R, Qiu J, Li M. Functionalized silk fibroin dressing with topical bioactive insulin release for accelerated chronic wound healing. *Mater Sci Eng* 2017;**72**:394-404.
77. Ehterami A, Salehi M, Farzamfar S, Vaez A, Samadian H, Sahrapeyma H, *et al*. *In vitro* and *in vivo* study of PCL/COLL wound dressing loaded with insulin chitosan nanoparticles on cutaneous wound healing in rats model. *Int J Biol Macromol* 2018;117:601-9.
78. Abdelkader DH, Tambuwala MM, Mitchell CA, Osman MA, El Tanani SA, McCarron PA. Enhanced cutaneous wound healing in rats following topical delivery of insulin loaded nanoparticles embedded in poly (vinyl alcohol) borate hydrogels. *Drug Deliv Transl Res* 2018;**8**:1053-65.
79. Ribeiro MC, Rocha Correa VL, Lopes da Silva FK, Casas AA, de Lima das Chagas A, L.P. de Oliveria, *et al*. Wound healing treatment using insulin within polymeric nanoparticles in diabetic animal model. *Eur J Pharm Sci* 2020;**150**:105330.
80. Adam MM, Michael JN, John C, Tomoyo K, Xiang S, Beatrice YJTY, *et al*. Lactate Treatment Causes NF-B Activation and CD44 Shedding in Cultured Trabecular Meshwork Cells. Glaucoma. 2007;**48**:1615-21.
81. Zhu YP, Brown JR, Sag D, Zhang L, S Jill. Adenosine 5'-Monophosphate activated protein kinase regulates IL-10 mediated Anti-Inflammatory Signaling Pathways in macrophages. *J Immunol* 2015;**194**:584-94.
82. Hosoyama T, Aslam MI, Abraham J, Prajapati SI, Nishijo K, Michalek JE, *et al*. IL-4R drives dedifferentiation, mitogenesis, and metastasis in rhabdomyosarcoma. *Clin Cancer Res* 2011;**17**:2757–66.
83. Sukhanov S, Higashi Y, Shai SY, Vaughn C, Mohler J, Li Y, *et al*. IGF-1 reduces inflammatory responses, suppresses oxidative stress, and decreases atherosclerosis progression in ApoE-deficient mice. *Arter Thromb Vasc Biol* 2007;**27**:2684-90.
84. Price WA, Moats Staats BM, Stiles AD. Pro-and anti-inflammatory cytokines regulate insulin-like growth factor binding protein production by fetal rat lung fibroblasts. *Am J Respir Cell Mol Biol* 2002;**26**:283-9.
85. Fraternale A, Brundu S, Magnani M. Polarization and Repolarization of Macrophages. *Cell Immunol* 2015;**6**:2.

86. Weisser SB, McLarren KW, Kuroda E, Sly LM. Generation and characterisation of murine alternatively activated macrophages. *Methods Mol Biol*. 2013;**946**:225-39.
87. Huang S, Czech MP. The GLUT4 glucose transporter. *Cell Metab*.2007;**5**:237-52.
88. McMillan DE. The microcirculation in diabetes. Microcirc Endothelium Lymphatics. 1984;**1**:3-24.
89. Li Q, Liu X, Yin Y, Zheng JT, Jiang CF, Wang J, *et al*. Insulin regulates glucose consumption and lactate production through reactive oxygen species and pyruvate kinase M2. *Oxid Med Cell longev* 2014;**2014**:504953.
90. Hulsmans M, Van Dooren E, Holvoet P. Mitochondrial reactive oxygen species and risk of atherosclerosis. *Cur Atheroscler Rep* 2012;**14**: 264-76.
91. Kennedy KM, Dewhirst MW. Tumor metabolism of lactate: the influence and therapeutic potential for MCT and CD147 regulation. *Future Oncol*. 2010;**6**:127-48.
92. Punzo C, Xiong W, Cepko CL. Loss of daylight vision in retinal degeneration: are oxidative stress and metabolic dysregulation to blame? *J Biol Chem* 2012;**287**:1642-48.
93. Eltzschig HK, Carmeliet P. Hypoxia and inflammation. *N Engl J Med* 2011;**364**:656-65.
94. Zgheib C, MH Maggie, Hu J, WL Kenneth, Xu Junwang. Long non-coding RNA lethe regulates hyperglycemia induced reactive oxygen species production in macrophages. *PloS ONE* 2017;**12**:e0177453.
95. Griesmacher A, Kindhauser M, Andert SE, Schreiner W, Toma C, Konebl P, *et al*. Enhanced serum levels of thiobarbituric-acid-reactive substances in diabetes milletus. *Am J Med* 1995;**98**:469-75.
96. Mauricio D, Mandrup-Poulsen T. Apoptosis and the pathogenesis of IDDM: a question of life and death. *Diabetes* 1998;**47**:1537-43.
97. Porter BO, Malek TR. Prostaglandin E2 inhibits T cell activation-induced apoptosis and Fas mediated cellular cytotoxicity by blockade of Fas-ligand induction. *Eur J Immunol* 1992;**29**:2360-5.
98. Zeng T, Zhou1 J, He L, Zheng J, Chen L, Wu C, *et al*. Blocking Nuclear Factor-Kappa B Protects against Diet-Induced Hepatic Steatosis and Insulin Resistance in Mice. *PLoS ONE* 2016;**11**:e0149677.
99. Muse ED, Obici S, Bhanot S, Monia BP, McKay RA, Rajala MW. Role of resistin in diet induced hepatic insulin resistance. *J Clin Invest* 2004;**114**:232–39.
100. Schiekofer S, Galasso G, Andrassy M, Aprahamian T, Schneider J, Rocnik E. Glucose control with insulin results in reduction of NFkβ binding activity in mononuclear blood

cells of patients with recently manifested type 1 diabetes. *Diabetes Obes Meta* 2006;**8**:473-82.

101. Huang X, Yang Z. Resistin, obesity and insulin resistance: the continuing disconnect between rodents and humans. *J Endocrinol Invest* 2016;**39**:607-15.
102. Zeng T, Zhou J, He L, Zheng J, Chen L, Wu C, *et al*. Blocking nuclear factor kappa B protects against diet induced hepatic steatosis and insulin resistance in mice. *PloS ONE* 2016;**11**:e0149677.
103. Rapiavoli NA, Qu K, Zhang J, Mikhail M, Laberge RM, Chang HY. A mammalian pseudogene lncRNA at the interface of inflammation and anti-inflammatory therapeutics. *Elife* 2013;**2**:e00762.
104. Xu J, Wu W, Zhang J, Dorset Martin W, Morris MW, Mitchell ME, *et al*. The role of microRNA-146a in the pathogenesis of the diabetic wound healing impairment: correction with mesenchymal stem cell treatment. *Diabetes* 2012;**61**: 2906-12.
105. Sprague A, Khalil RA. Inflammatory cytokines in vascular dysfunction and vascular disease. *Biochem Pharmacol*. 2009;**78**:539-52.
106. Martins GR. Gelaleti GB, Moschetta MG, Maschio-Signorini LB, Pires de Campos Zuccari DA. Proinflammatory and anti- Inflammatory cytokines mediated by NF-*κ*B factor as prognostic markers in mammary tumors. *Mediators Inflamm* 2016;**2016**: 9512743.
107. Paolo EP, Valery LP, Jean PT, Olivier F, Pierre S. Lactate stimulates angiogenesis and accelerates the healing of superficial and ischemic wounds in mice. *Angiogenesis* 2012;**15**:581-92.
108. Ghani QP, Wagner S, Becker HD, Hunt TK, Hussain MZ. Regulatory role of lactate in wound repair. *Methods Enzymol* 2004;**381**:565-75.
109. Zgheib C, Hodges MM, Hu J, Liechty KW, Xu J. Long noncoding RNA lethe regulates hyperglycemia induced reactive oxygen species production in macrophages. *PloS ONE* 2017;**12**:e0177453.
110. Dong J, Jimi E, Zhong H, Hayden MS, Ghosh S. Repression of gene expression by unphosphorylated NF-κB p65 through epigenetic mechanisms. *Genes Dev* 2008;**22:**1159–1173.
111. Wang Y, Cao J, Fan Y, Xie Y, Xu Z, Yin Z, *et al*. Artemisinin inhibits monocyte adhesion to HUVECs through the NF-κB and MAPK pathways *in vitro*. *Int J Mol Med* 2016;**37**:1567-75.

112. Choi CS, Kim YB, Lee FN, Zabolotny JM, Kahn BB, Youn JH. Lactate induces insulin resistance in skeletal muscle by suppressing glycolysis and impairing insulin signaling. *Am J Physiol Endocrinol Metab* 2002;**283**:233-40.
113. Lee FN, Kim YB, Choi CS, Zabolotny JM, Kahn BB, Youn JH. Lactate Induces Insulin Resistance in Skeletal Muscle by Impairing Insulin Signaling and Decreasing Insulin-stimulated Glucose Transport Activity. *Diabetes* 2001;**50**:A330.
114. Guo X, Li H, Xu H, Woo S, Dong H, Lu F, *et al*. Glycolysis in the control of blood glucose homeostasis. *Acta Pharm B* 2012;**2**:358-67.
115. Saltiel AR, Kahn CR. Insulin signalling and the regulation of glucose and lipid metabolism. *Nature* 2001;**414**:799-806.
116. Jensen Urstad AP, Semenkovich CF. Fatty acid synthase and liver triglyceride metabolism: housekeeper or messenger? *BBA Mol Cell Biol L* 2012;**1821**:747-53.
117. Muoio DM, Newgard CB. Molecular and metabolic mechanisms of insulin resistance and β-cell failure in type 2 diabetes. *Nat Rev Mol Cell Biol* 2008;**9**:193-205.
118. Dumont O, Mylorie H, Bauer A, Calay D, Sperone A, Thornton C, *et al*. Protein kinase Cϵ activity induces anti-inflammatory and anti-apoptotic genes via an ERK1/2-and NF-Ƙ B-dependent pathway to enhance vascular protection. *Biochem J* 2012;**447**:193-204.
119. James AM, Collins Y, Logan A, Murphy MP. Mitochondrial oxidative stress and the metabolic syndrome. *Trends Endocrinol Metab* 2012;**23**:429-34.
120. James S, Ryan JH, Xinchun P, Masanori Y, Chen Y, Bradford CB. Fluid shear stress inhibits TNF-α activation of JNK but not ERK1/2 or p38 in human umbilical vein endothelial cells: Inhibitory crosstalk among MAPK family members. *Proc Natl Acad Sci U S A* 2011;**98**:6476-81.
121. Lee JC, Laydon JT, McDonnell PC, Gallagher TF, Kumar S, Green D, *et al*. A protein kinase involved in the regulation of inflammatory cytokine biosynthesis. *Nature* 1994;**372**:739.
122. Baumlova A, Gregor J, Boura E. The Structural Basis for Calcium Inhibition of Lipid Kinase PI4K IIα and Comparison With the Apo State. *Physiol Res* 2016;**65**:987-93.
123. Adolfo RAP, Andres MCG, Marianne LR, Beatriz LC. c-Fos activates and physically interacts with specific enzymes of the pathway of synthesis of polyphosphoinositides. *Mol Biol Cell* 2011;**22**:4716-25.
124. Laurence H, Karima B, Philippe R, Ravi M, Palaniyi R, Frank T, *et al*. Signaling pathways involved in LPS induced TNFalpha production in human adipocytes. *J Inflamm Res* 2010;**8**:7-11.

125. Barrett EJ, Wang H, Upchurch CT, Liu Z. Insulin regulates its own delivery to skeletal muscle by feed-forward actions on the vasculature. *Am J Physiol Endocrinol Metab* 2011;**301**:252-63.
126. Greenhaff PL, Karagounis L, Peirce N, Simpson E, Hazell M, Layfield R, *et al*. Disassociation between the effects of amino acids and insulin on signaling, ubiquitin ligases, and protein turnover in human muscle. *Am J Physiol Endocrinol Metab* 2008;**295**:595-604.
127. Bagry HS, Raghavendran S, Carli F. Metabolic Syndrome and Insulin ResistancePerioperative Considerations. *Anesthesiology: ASA* 2008;**108**:506-23.
128. Fujita S, Rasmussen BB, Cadenas JG, Grady JJ, Volpi E. Effect of insulin on human skeletal muscle protein synthesis is modulated by insulin-induced changes in muscle blood flow and amino acid availability. *Am J Physiol Endocrinol Metab* 206; **291**:745-54.
129. Tesseraud S, Métayer S, Duchene S, Bigot K, Grizard J, Dupont J. Regulation of protein metabolism by insulin: value of different approaches and animal models. *Domest Anim Endocrino* 2007;**33**:123-42.
130. Kanazawa T, Taneike I, Akaishi R, Yoshizawa F, Furuya N, Fujimura S, *et al*. Amino acids and insulin control autophagic proteolysis through different signaling pathways in relation to mTOR in isolated rat hepatocytes. *J Biol Chem* 2004;**279**:8452-59.
131. Stump CS, Short KR, Bigelow ML, Schimke JM, Nair KS. Effect of insulin on human skeletal muscle mitochondrial ATP production, protein synthesis, and mRNA transcripts. *Proc Natl Acad Sci U S A* 2003;**100**:7996-8001.
132. Proud C. Regulation of protein synthesis by insulin. *Portland Press Ltd* 2006.
133. Moller N. Jorgensen JOL. Effects of growth hormone on glucose, lipid, and protein metabolism in human subjects. *Endocr Rev* 2009;**30**:152-77.
134. Wang X, Hu Z, Hu J, Du J, Mitch WE. Insulin resistance accelerates muscle protein degradation: activation of the ubiquitin-proteasome pathway by defects in muscle cell signaling. *Endocrinol* 2006;**14**:4160-68.
135. Rabinowitz JD, White E. Autophagy and metabolism. Science. 2010; 330: 1344-48.
136. Higashi Y, Sukhanov S, Anwar A, Shai SY, Delafontaine P. IGF-1, oxidative stress and atheroprotection. *Trends Endocrinol Metab* 2010;**21**:245-54.
137. Werner H, Weinstein D, Bentov I. Similarities and differences between insulin and IGF-I: structures, receptors, and signalling pathways. *Arch Physiol Biochem* 2008;**114**:17-22.

138. Haase I, Evans R, Pofahl R, Watt FM. Regulation of keratinocyte shape, migration and wound epithelialization by IGF-1-and EGF-dependent signalling pathways. *JSC* 2003;**116**:3227-38.
139. Burks DJ, White MF. IRS proteins and beta-cell function. *Diabetes* 2001;**50**:140.
140. Yamada Y, Kohashi K, Fushimi F, Takahashi Y, Setsu N, Endo M, *et al*. Activation of the Akt-mTOR pathway and receptor tyrosine kinase in patients with solitary fibrous tumors. *Cancer*. 2014;120:864-76.
141. Wilcox G. Insulin and insulin resistance. *Clin Biochem Rev* 2005;**26**:19-39.
142. Salazar JJ, Ennis WJ, Koh TJ. Diabetes medications: Impact on inflammation and wound healing. *J Diabetes Complicat* 2016;**30**:746-52.
143. Novak ML, Koh T.J. Phenotypic transitions of macrophages orchestrate tissue repair. *Am J Pathol* 2013;**183**:1352-63.
144. Falanga V. The chronic wound: impaired healing and solutions in the context of wound bed preparation. *Blood Cells Mol Dis* 2004;**32**:88-94.
145. Strodtbeck F. Physiology of wound healing. *Newborn Infant Nurs Rev* 2001;**1**:43-52.
146. Harding K, Morris H, Patel G. Healing chronic wounds. *BMJ* 2002; **324**:160.
147. McCormick SM, Heller NM. Regulation of macrophage, dendritic cell, and microglial phenotype and function by the SOCS proteins. *Front Immunol* 2015;**6**:549.
148. Guo SA, Di Pietro LA. Factors affecting wound healing. J Dent Res. 2010; 89: 219-29.
149. Jerrold MO, Christopher KG. Macrophages, Inflammation, and Insulin Resistance. *Annu Rev Physiol*. 2010;**72**:219–46.
150. Thomsen LH, Rosendahl A. Polarization of macrophages in metabolic diseases. *Cell Immunol*. 2015;**6**:2.
151. Wang N, Liang H, Zen K. Molecular mechanisms that influence the macrophage M1–M2 polarization balance. *Front Immunol* 2014;**5**:614.
152. Margaret LN, Timothy JK. Phenotypic Transitions of Macrophages Orchestrate Tissue Repair. *Am J Pathol* 2013;**183**:1352-63.
153. Ferreira AE, Sisti F, Sonego F, Wang S, Filgueiras LR, Brandt S, *et al*. PPAR-g/IL-10 axis inhibits MyD88 expression and ameliorates murine polymicrobial sepsis. *J Immunol* 2014;**192**:2357-65.
154. Siamon G, Fernando OM. Alternative activation of macrophages: mechanism and functions. *Immunity* 2010;32:593-604.
155. Kim HI, Ahn YH. Role of Peroxisome Proliferator–Activated Receptor-ϒ in the glucose sensing apparatus of liver and cells. *Diabetes* 2004;53:60-5.

156. Rita EM, Milie MF, William JE, Timothy JK. Blocking Interleukin-1β Induces a Healing-Associated Wound Macrophage Phenotype and Improves Healing in Type 2 Diabetes. *Diabetes* 2013;**62**:2579–87.
157. Mohamed A, Menno PJ, Winthera b, Jan Van den B. Epigenetic mechanisms of macrophage activation in type 2 diabetes. *Immunobiology* 2017;**222**:937–43.
158. Giacco F. Brownlee M. Oxidative Stress and Diabetic Complications. Stress and inflammation in obesity and diabetes. *Circ Res* 2010;**107**:1058-70.
159. Mario AR, Lauterbach F. Thomas W. Macrophage functions in obesity-induced inflammation and insulin resistance. *Pflug Arch Eur J Phy* 2017;**469**:385–96.
160. Glenn FP. Inflammation in Nonhealing Diabetic Wounds The Space Time Continuum Does Matter. Inflammation in Nonhealing Diabetic Wounds. *Am J Pathol* 2001;**159**:399- 403.
161. Sara MM, Steven LP. Proteases and delayed wound healing. *Adv Wound Care* 2013; **2**:438-47.
162. Zhao R, Liang H, Clarke E, Jackson C, Xue M. Inflammation in chronic wounds. *Int J Mol Sci* 2016;**17**:2085.
163. Kasuya A, Tokura Y. Attempts to accelerate wound healing. *J Dermatol Sci* 2014;**76**:169-72.
164. Werner H, Weinstein D, Bentov I. Similarities and differences between insulin and IGF-I: structures, receptors, and signalling pathways. *Arch Physiol Biochem* 2008;**114**:17-22.
165. Wang N, Liang H, Zen K. Molecular mechanisms that influence the macrophage M1–M2 polarization balance. *Front Immunol* 2014;5.
166. Munte CE, Vilela L, Kalbitzer HR, Garratt RC. Solution structure of human proinsulin C-peptide. *FEBSJ* 2005;**272**:4284-93.
167. Lim YC, Bhatt MP, Kwon MH, Park D, Na S, Kim YM, *et al*. Proinsulin C-peptide prevents impaired wound healing by activating angiogenesis in diabetes. *J Investig Dermatol* 2015;**135**:269-78.
168. Haidet J, Cifarelli V, Trucco M, Luppi P. C-peptide reduces pro-inflammatory cytokine secretion in LPS-stimulated U937 monocytes in condition of hyperglycemia. *Inflamm Res* 2012;**61**:27-35.
169. Bloomgarden Z.T. Diabetes complications. *Diabetes Care* 2004;**27**:1506-14.
170. Hills CE, Brunskill NJ, Squires PE. C-peptide as a therapeutic tool in diabetic nephropathy. *Am J Nephrol* 2010;**31**:389-97.

171. Vasic D, Walcher D. Proinflammatory effects of C-Peptide in different tissues. *Int J inflamm* 2012;**2012**.
172. Martin P, Nunan R. Cellular and molecular mechanisms of repair in acute and chronic wound healing. *Br J Dermatol* 2015;**73**:370-8.
173. Association AD. Diagnosis and classification of diabetes mellitus. *Diabetes Care* 2014;**37**:S81-90.
174. Association AD. Treatment of symptomatic polyneuropathy with actovegin in type 2 diabetic patients. *Diabetes Care* 2009;**32**:S62-7.
175. Zunkler B, Lenzen S, Manner K, Panten U, Trube G. Concentration dependent effects of tolbutamide, meglitinide, glipizide, glibenclamide and diazoxide on ATP-regulated K^+ currents in pancreatic B-cells. *Naunyn Schmiedebergs Arch Pharmacol* 1988;**337**:225-30.
176. Nguyen NDT, Le LT. Targeted proteins for diabetes drug design. *Adv Nat Sci: Nanosci Nanotech* 2012;**3**:013001.
177. Lima MHM, Caricilli AM, de Abreu LL, Araujo EP, Pelegrinelli FF, Thirone ACP. Topical insulin accelerates wound healing in diabetes by enhancing the AKT and ERK pathways: a double blind placebo controlled clinical trial. *PLoS One* 2012;7e36974.
178. Choudhury D, Xavier PL, Chaudhari K, John R, Dasgupta AK, Pradeep T, *et al*. Unprecedented inhibition of tubulin polymerization directed by gold nanoparticles inducing cell cycle arrest and apoptosis. *Nanoscale* 2013;**5**:4476-89.
179. Choudhury D, Ganguli A, Dastidar DG, Acharya BR, Das A, Chakrabarti G. Apigenin shows synergistic anticancer activity with curcumin by binding at different sites of tubulin. *Biochimie* 2013;**95**:1297-309.
180. Sharma K, Kumar A, Taneja G, Nagaich U, Deep A, Rajput SK. Synthesis and preliminary therapeutic evaluation of copper nanoparticles against diabetes mellitus and -induced micro- (renal) and macro-vascular (vascular endothelial and cardiovascular) abnormalities in rats. *RSC Adv* 2016;**6**:36870-80.
181. Calisto FC, Calisto SL, Souza AP, Franca CM, Ferreira AP, Moreira MB. Use of low-power laser to assist the healing of traumatic wounds in rats. *Acta Cir Bras* 2015;**30**:204-8.
182. Gal P, Kilik R, Mokry M, Vidinsky B, Vasilenko T, Mozes S, *et al*. Simple method of open skin wound healing model in corticosteroid treated and diabetic rats: standardization of semi-quantitative and quantitative histological assessments. *Vet Med* 2008;**53**:652-9.

183. Kelly SM, Price NC. The use of circular dichroism in the investigation of protein structure and function. *Curr Protein Pept Sci* 2000;**1**:349-84.
184. Choi J, Park S, Stojanovic Z, Han HS, Lee J, Seok HK, *et al*. Facile Solvothermal preparation of monodisperse gold nanoparticles and their engineered assembly of ferritin–gold nanoclusters. *Langmuir* 2013;**29**:15698-703.
185. Brand I, Habecker F, Ahlers M, Kluener T. Structure of collagen adsorbed on a model implant surface resolved by polarization modulation infrared reflection absorption spectroscopy. *Spectrochem Acta A Mol Biomol Spectrosc* 2015;**138**:216-24.
186. Mansour RS, Sallam AA, Hamdan II, Khalil EA, Yousef I. Elucidation of penetration enhancement mechanism of emu oil using FTIR microspectroscopy at EMIRA laboratory of SESAME synchrotron. *Spectrochem Acta A Mol Biomol Spectrosc* 2017;**185**:1-10.
187. Hansen L, Van Renterghem J, Daoussi R, Vervaet C, Remon JP, De Beer T. Spectroscopic evaluation of a freeze-dried vaccine during an accelerated stability study. *Eur J Pharm Biopharm* 2016;**104**:89-100.
188. Gliniak J, Lin JH, Chen YT, Li CR, Jokar E, Chang CH, *et al*. Sulphur doped graphene oxide quantum dots as photocatalysts for hydrogen generation in the aqueous phase. *ChemSusChem* 2017;**10**:3260-7.
189. Beg M, Maji A, Mandal AK, Das S, Aktara MN, Jha PK, *et al*. Green synthesis of silver nanoparticles using Pongamia pinnata seed: characterization, antibacterial property, and spectroscopic investigation of interaction with human serum albumin. *J Mol Recognit* 2017;**30**:1-18.
190. Roeters S, Van Dijk C, Torres Knoop A, Backus EH, Campen RK, Bonn M. Determining in situ protein conformation and orientation from the amide-I sum frequency generation spectrum: theory and experiment. *J Phys Chem A* 2013;**117**:6311-22.
191. Luber S. Solvent effects in calculated vibrational Raman optical activity spectra of α-helices. *J Phys Chem A* 2013;**117**:2760-70.
192. Malon P, Bednarova L, Straka M, Krejci L, Kumprecht L, Kraus T, *et al*. Disulfide chromophore and its optical activity. Chirality 2010:**22**.
193. Stalhandske CM, Stalhandske CI, Persson I, Sandstrom M, Jalilehvand F. Crystal and solution structures of N,N-dimethylthioformamidesolvated copper(I), silver(I), and gold(I) ions studied by X-ray diffraction, X-ray absorption, and vibrational spectroscopy. *Inorg Chem* 2001;**40**:6684-93.

194. Pradhan L, Nabzdyk C, Andersen ND, LoGerfo FW, Veves A. Inflammation and neuropeptides: the connection in diabetic wound healing. *Expert Rev Mol Med* 2009;11e2.
195. Landen NX, Li D, Stahle M. Transition from inflammation to proliferation: a critical step during wound healing. *Cell Mol Life Sci* 2016;**73**:3861-85.
196. Avishai E, Yeghiazaryan K, Golubnitschaja O. Impaired wound healing: facts and hypotheses for multi-professional considerations in predictive, preventive and personalised medicine. *EPMA J* 2017;**8**:23-33.
197. Edwards R, Harding KG. Bacteria and wound healing. *Curr Opin Infect Dis* 2004;**17**:91-6.
198. Werner S, Krieg T, Smola H. Keratinocyte fibroblast interactions in wound healing. *J Invest Dermatol* 2007;**127**:998-1008.
199. Kang YE, Kim JM, Joung KH, Lee JH, You BR, Choi MJ, *et al*. The roles of adipokines, proinflammatory cytokines, and adipose tissue macrophages in obesity associated insulin resistance in modest obesity and early metabolic dysfunction. *PLoS One* 2016;11e0154003.
200. Brem H, Tomic Canic M. Cellular and molecular basis of wound healing in diabetes. *J Clin Invest* 2007;**117**:1219.
201. Jayachandran M, Rodriguez S, Solis E, Lei J, Godavarty A. Critical review of noninvasive optical technologies for wound imaging. Adv. *Wound Care (New Rochelle)* 2016;**5**:349-59.
202. Paul D, Ghassemi P, Ramella Roman JC, Prindeze NJ, Moffatt LT, Alkhalil A, *et al*. Noninvasive Imaging Technologies for Cutaneous Wound Assessment: A Review. *Wound repair regen* 2015;**23**:149-62.
203. Lange F, Tachtsidis I. Clinical Brain Monitoring with Time Domain NIRS: A Review and Future Perspectives. *Appl Sci* 2019;**9**:1612.
204. Van Beekvelt MC, Borghuis MS, Van Engelen BG, Wevers RA, Colier WN. Adipose Tissue Thickness Effects in Vivo Quantitative near IR Spectroscopy in Human Skeletal Muscle. *Cin Sci (Lond)* 2001;**101**:21-8.
205. De Boer LL, Bydlon TM, Van Duijnhoven F, Vranken Peeters MTFD, Loo CE, Winter Warnars GAO, *et al*. Towards the use of diffuse reflectance spectroscopy for real time *in vivo* detection of breast cancer during surgery. *J Transl Med* 2018;**16**:367.
206. Yu B, Shah A, Nagarajan VK, Ferris DG. Diffuse reflectance spectroscopy of epithelial tissue with a smart fiber optic probe. *Biomed Opt Express* 2014;**5**:675-89.

207. Zhou L, El Deiry WS. Multispectral fluorescence imaging. *J Nucl Med* 2009;**50**:1563-66.
208. Cheng H, Duong TQ. Simplified laser-speckle-imaging analysis method and its application to retinal blood flow imaging. *Opt Lett* 2007;**32**:2188-90.
209. Leutenegger M, Williams EM, Harbi P, Thacher T, Raffoul W, Andre M, *et al*. Real time full field laser Doppler imaging. *Biomed Opt Express* 2011;**2**:1470–77.
210. Klein ME, Aalderink DJ, Padoan R, De Bruin G, Steemers TA. Quantitative Hyperspectral Reflectance Imaging. *Sensors* 2008;**8**:5576-618.
211. Zou D, Zhang Y, Cui Y, Qian G. Near infrared emissive metal organic frameworks. *Dalton Trans* 2019;**48**:6669-75.
212. Wang HS. Metal organic frameworks for biosensing and bioimaging applications. *Coord Chem Rev* 2017;**349**:139-55.
213. Liu Y, Xie XY, Cheng C, Shao ZS, Wang HS. Strategies to fabricate metal-organic framework (MOF)-based luminescent sensing platforms. *J Mater Chem C* 2019;**7**:10743-63
214. Liu JM, Lin LP, Wang XX, Lin SQ, Cai WL, Zhang LH, *et al*. Highly selective and sensitive detection of Cu^{2+} with lysine enhancing bovine serum albumin modified carbon dots fluorescent probe. *Analysis* 2012;**137**:2637–42.
215. Le Guevel X. Recent Advances on the Synthesis of Metal Quantum Nanoclusters and Their Application for Bioimaging. *IEEE J Sel Top Quant* 2014;**20**:6801312.
216. Xavier PL, Chaudhari K, Baksi A, Pradeep T. Protein protected luminescent noble metal quantum clusters: an emerging trend in atomic cluster nanoscience. *Nano Rev* 2012;**3**:10.
217. Zheng J, Nicovich PR, Dickson RM. Highly fluorescent noble-metal quantum dots. *Annu Rev Phys Chem* 2007;**58**:409-31.
218. Li C, Chen W, Wu D, Quan D, Zhou Z, Hao J, *et al*. Large Stokes shift and high efficiency luminescent solar concentrator incorporated with $CuInS_2$/ ZnS quantum dots. *Sci Rep* 2015;**5**:17777.
219. Li M, Yang DP, Wang X, Lu J, Cui D. Mixed protein-templated luminescent metal clusters (Au and Pt) for H_2O_2 sensing. *Nanoscale Res Lett* 2013;**8**:182.
220. Lusk AT, Jennings GK. Characterization of Self assembled monolayers formed from sodium *S*-alkyl thiosulfates on copper**.** *Langmuir* 2011;**17**:7830-6.
221. Chen LY, Wang CW, Yuan Z, Chang HT. Fluorescent gold nanoclusters: recent advances in sensing and imaging. *Anal Chem* 2015;**87**:216–29.

222. Liu QM, Zhou DB, Yamamoto Y, Ichino R, Okido M. Preparation of Cu nanoparticles with $NaBH_4$ by aqueous reduction method. *Trans Nonferrous Met Soc* 2012;**22**:117–23.
223. Das NK, Ghosh S, Priya A, Datta S, Mukherjee S. Luminescent Copper Nanoclusters as a Specific Cell-Imaging Probe and a Selective Metal Ion Sensor. J. Phys. Chem. C 2015;**119**:24657-64.
224. Liu CL, Wu HT, Hsiao YH, Lai CW, Shih CW, Peng YK, *et al*. Insulin-Directed Synthesis of Fluorescent Gold Nanoclusters: Preservation of Insulin Bioactivity and Versatility in Cell Imaging. *Angew Chem Int Ed* 2011;**50**:7056-60.
225. Subramanian V, Jena S, Ghosh D, et al. Dual Probe Sensors Using Atomically Precise Noble Metal Clusters. ACS Omega 2017;2:7576-83.
226. Siddique AB, Pramanick AK, Chatterjee S, Ray M. Amorphous Carbon Dots and their Remarkable Ability to Detect 2,4,6-Trinitrophenol. *Sci Rep* 2018;**8**:9770.
227. Benito Q, Le Goff XF, Maron S, Fargues A, Garcia A, Martineau C, *et al*. Polymorphic copper iodide clusters: insights into the mechanochromic luminescence properties. *J Am Chem Soc* 2014;**136**:11311-20.
228. Yang H, Zhang S, Cao R, Deng X, Li Z, Xu X, *et al*. Constructing the novel ultrafine amorphous iron oxyhydroxide/g-C3N4 nanosheets heterojunctions for highly improved photocatalytic performance. *Sci Rep* 2017;**7**:8686.
229. Wang AG, Chen C, Shi H, Chen Y, Shen X, Lotnyk A. The realization of insulator-metal transition in a p-type metastable ZnSb by dual-phase nanostructure. Scr Mater 2020;186:163-8.
230. Cao Y, Wang HJ, Cao C, et al. Inhibition effects of protein-conjugated amorphous zinc sulfide nanoparticles on tumor cells growth. J Nanopart Res 2011;13:2759–67.
231. Xie J, Zheng Y, Ying JY. Protein directed synthesis of highly fluorescent gold nanoclusters. *J Am Chem Soc* 2009;**131**:888-9.
232. Shang L, Dong S. Facile preparation of water-soluble fluorescent silver nanoclusters using a polyelectrolyte template. *Chem Commun* 2008;**9**:1088-90.
233. Roohani N, Hurrell R, Kelishadi R, Schulin R. Zinc and its importance for human health: An integrative review. *J Res Med Sci* 2013;**18**:144–57.
234. Watanabe M, Hayasaki H, Tamayama T, Shimada M. Histological distribution of insulin and glucagon receptors. *Braz J Med Biol Res* 1998;**31**:243-56.
235. Havrankova J, Roth J, Brownstein M. Insulin receptors are widely distributed in the central nervous system of the rat. *Nature* 1978;**272**:827-9.

236. Papa V, Pezzino V, Costantino A, Belfiore A, Giuffrida D, Frittitta L, *et al*. Elevated insulin receptor content in human breast cancer. *J Clin Invest* 1990;**86**:1503-10.
237. Goldfine D, Vigneri R. Elevated insulin receptor content in human breast cancer. *J Clin Invest* 1990;**86**:1503-10.
238. Milazzo G, Giorgno F, Damante G, Sung S, Stampfer MR, Vigneri R, *et al* . Insulin receptor expression and function in human breast cancer cell line. *Cancer Res* 1992;**52**:3924-30.
239. Lin PH, Sermersheim M, Li H, Lee PHU, Steinberg SM, Ma J. Zinc in Wound Healing Modulation. *Nutr J* 2018;**10**:16.
240. Saghiri MA, Asatourian A, Orangi J, Sorenson CM, Sheibani N. Functional role of inorganic trace elements in angiogenesis-Part II: Cr, Si, Zn, Cu, and S. *Crit Rev Oncol Hematol* 2015;**96**:143–55.
241. Tenaud I, Leroy S, Chebassier N, Dreno B. Zinc, copper, and manganese enhanced keratinocyte migration through a functional modulation of keratinocyte integrins. *Exp Dermatol* 2000;**9**:407–16.
242. Jayawardena R, Ranasinghe P, Galappatthy P, Malkanthi R, Constantine G, Katulanda P. Effects of zinc supplementation on diabetes mellitus: a systematic review and meta-analysis. *Diabetol Metab Syndr* 2012;**4**:13.
243. Kim J, Lee S. Effect of zinc supplementation on insulin resistance and metabolic risk factors in obese Korean women. *Nutr Res Pract* 2012;**6**:221–5.
244. Singh RB, Niaz MA, Rastogi SS, Bajaj S, Gaoli Z, Shoumin Z. Current zinc intake and risk of diabetes and coronary artery disease and factors associated with insulin resistance in rural and urban populations of North India. *J Am Coll Nutr* 1998;**17**:564-70.
245. Viktorinova A, Toserova E, Krizko M, Durackova Z. Altered metabolism of copper, zinc, and magnesium is associated with increased levels of glycated hemoglobin in patients with diabetes mellitus. *Metab* 2009;**58**:1477-82.
246. Habeeb Muhammed MA, Verma PK, Pal SK, Retnakumari A, Koyakutty M, Nair S, *et al*. Luminescent quantum clusters of gold in bulk by albumin-induced core etching of nanoparticles: metal ion sensing, metal-enhanced luminescence, and bio labeling. *Chem Eur J* 2010;**16**:10103-12.
247. Jarosz M, Olbert M, Wyszogrodzka G, Mlyniec K, Librowski T. Antioxidant and anti-inflammatory effects of Zinc: Zinc dependent NFkβ signaling. *Inflammopharmacology* 2017;**25**:11-24.

248. Prasad AS. Zinc is an Antioxidant and anti-inflammatory agent: its role in human health. *Front Nutr* 2014;**1**:14.
249. Batool M, Khurshid S, Qureshi Z, Daoush WM. Adsorption, antimicrobial, and wound healing activities of biosynthesised zinc oxide nanoparticles. *Chem Pap* 2020.
250. Han B, Fan WH, Zhao S, Yang Z. Zinc sulfide nanoparticles improve skin regeneration. Nanomedicine: NBM 2020;**29**:102263.
251. Kogan S, Sood A, Mark S. Granick. Zinc and Wound Healing: A Review of Zinc Physiology and Clinical Applications. *Wounds* 2017;**29**102-6.
252. Shang L, Dong S, Nienhaus GU. Ultra-small fluorescent metal nanoclusters: synthesis and biological applications. *Nano today* 2011;**6**:401-18.
253. Datta S, Choudhury D, Das A, Mukherjee DD, Dasgupta M, Bandopadhyay S, *et al*. Correction to Autophagy inhibition with chloroquine reverts paclitaxel resistance and attenuates metastatic potential in human non-small lung adenocarcinoma A549 cells via ROS mediated modulation of β-catenin pathway. *Apoptosis* 2019;**24**:414-33.
254. Choudhury D, Das A, Bhattacharya A, Chakrabarti G. Aqueous extract of ginger shows anti-proliferative activity through disruption of microtubule network of cancer cells. *Food Chem Toxicol* 2010;48:2872-80.
255. Datta S, Choudhury D, Das A, Das Mukherjee D, Roy SS, Chakrabarti G. Paclitaxel resistance development is associated with biphasic changes in ROS, mitochondrial membrane potential, and autophagy with elevated energy production capacity in lung cancer cells: A chronological study. *Tumor Biol* 2017;**39**:1–14.
256. Tran TA, Krishnamoorthy K, Cho SK, Kim SJ. Inhibitory effect of zinc sulphide nanoparticles towards breast csancer stem cell migration and invasion. *J Biomed Nanotechnol* 2016;**12**:329–36.
257. Choudhury D, Ganguli A, Dastidar DG, Acharya BR, Das A, Chakrabarti G. Apigenin shows synergistic anticancer activity with curcumin by binding at different sites of tubulin. *Biochimie* 2013;95:1297-309.
258. Choudhury D, Xavier PL, Chaudhari K, John R, Dasgupta AK, Pradeep T, *et al*. Unprecedented inhibition of tubulin polymerization directed by gold nanoparticles inducing cell cycle arrest and apoptosis. Nanoscale 2013;5(10):4476-89.
259. Clement MJ, Rathinasamy K, Adjadj E, Toma F, Curmi PA, Panda D. Benomyl and colchicines synergistically inhibit cell proliferation and mitosis: evidence of distinct binding sites for these agents in tubulin. *Biochemia* 2008;**47**:13016e13025.

260. Harrison MJ, Burton NA, Hillier IH. Catalytic mechanism of the enzyme papain: predictions with a hybrid quantum mechanical/molecular mechanical potential. *J Am Chem Soc* 1997;**119**:12285-91
261. Zheng XT, Than A, Ananthanaraya A, Kim DH, Chen P. Graphene quantum dots as universal fluorophores and their use in revealing regulated trafficking of insulin receptors in adipocytes. *ACS Nano* 2013;**7**:6278-86.
262. Nagamani K, Prathap P, Lingappa Y, Miles RW, Reddy KTR. Properties of Al doped ZnS films grown by chemical bath deposition. *Phys Procedia* 2012;**25**:137-42.
263. Mehta R, Kaur P, Choudhary D, Paul K, Luxami V. Al^{3+} induced hydrolysis of Rhodamine-based Schiff-base: Applications in cell imaging and ensemble as CN^- sensor in 100% aqueous medium. *J Photochem Photobiol A* 2019;**380**:111851.
264. Lin JJ, Lee JJ, Hsieh K. Fluorescent metal nanoclusters: from synthesis to application: recent progress and present challenges. *Trends Anal. Chem* 2014;**58**:90-8.
265. Medintz IL, Uyeda HT, Goldman ER, Mattoussi H. Quantum dot bioconjugates for imaging, labeling, and sensing. *Nat Mater* 2005;**4**:435-46.
266. Alivisatos P. The use of nanocrystals in biological detection. Nat. Biotechnol. 2004;**22**:47.
267. Lin YF, Cheng CW, Shih CS, Hwang JK, Yu CS, Lu CH. MIB: metal ion-binding site prediction and docking server. *J Chem Inf Model* 2016;**56**:2287-91.
268. Cao W, Li F, Stenberg RH, Matthew MM. Development of Normal and Injury-induced Gene Expression of aFGF, bFGF, CNTF, BDNF, GFAP and IGF-I in the Rat Retina. *Exp Eye Res* 2001;**72**:591-604.
269. Lian H, Zhou Y, Jian ZH, Liu RZ. MiR-323-5p acts as a Tumor Suppressor by Targeting the Insulin like Growth Factor 1 Receptor in Human Glioma Cells. *Asian Pac J Cancer Prev* 2014;**15**:10181-5.
270. Alavi M, Rai M. Topical delivery of growth factors and metal/metal oxide nanoparticles to infected wounds by polymeric nanoparticles: an overview. *Expert Rev Anti Infect Ther* 2020;**18**:1021-32.
271. Alavi M, Jabari E, Jabbari E. Functionalized carbon-based nanomaterials and quantum dots with antibacterial activity: a review. *Expert Rev Anti Infect Ther* 2020.
272. Wang J, Xu J. Effects of topical insulin on wound healing: A review of animal and human evidences. *Diabetes Metab Syndr Obes* 2020;**13**:719-27.
273. Zheng J, Nicovich PR, Dickson RM. Highly fluorescent noble-metal quantum dots. *Annu Rev Phys Chem* 2007;58:409-31.

274. Cha H, Yoon JH, Yoon S. Probing quantum plasmon coupling using gold nanoparticle dimers with tunable interparticle distances down to the subnanometer range. *ACS Nano* 2014;**8**:8554-63.
275. Link S, Beeby A, FitzGerald S, El Sayed MA, Schaaff TG, Whetten RL. Visible to infrared luminescence from a 28-atom gold cluster. *J Phys Chem B* 2002;**106**:3410-15.
276. Hussain A, Sarangi S, Kesarwani J, Sahu S. Au-nanocluster emission based glucose sensing. *Biosens Bioelectron* 2011;**29**:60-5.
277. Yoffe AD. Semiconductor quantum dots and related systems: electronic, optical, luminescence and related properties of low dimensional systems. *Adv Phys* 2001;**50**:1-208.
278. Poderys V, Matulionyte Safine M, Rupsys D, Rotomskis R. Protein stabilized au nanoclusters: spectral properties and photostability. *Lith J Phys* 2016;**56**.
279. Li C, Chen W, Wu D, Quan D, Zhou Z, Hao J, *et al*. Wang, Large Stokes shift and high efficiency luminescent solar concentrator incorporated with $CuInS_2$/ZnS quantum dots. Sci Rep 2015;**5**:17777.
280. Jin YJ, Araki D, Teraguchi M, Aoki T, Kwak G. Dimesitylboryl containing polydiphenylacetylene with a large Stokes shift, high fluorescence efficiency, and fluoride ion sensing ability. *J Polym* 2018;**148**:310-5.
281. Li M, Yang DP, Wang X, Lu J, Cui D. Mixed protein-templated luminescent metal clusters (Au and Pt) for H_2O_2 sensing. *Nanoscale Res Lett* 2013;**8**:182.
282. Liu QM, Zhou DB, Yamamoto Y, Ichino R, Okido M. Preparation of Cu nanoparticles with NaBH4 by aqueous reduction method. Trans Nonferrous Met Soc 2012;**22**:117-23.
283. Wei H, Wang Z, Yang L, Tian S, Hou C, Lu Y. Lysozyme-stabilized gold fluorescent cluster: synthesis and application as Hg^{2+} sensor. *Anal* 2010;**135**:1406-10.
284. Lin YH, Tseng WL. Ultrasensitive sensing of Hg^{2+} and CH_3Hg^+ based on the fluorescence quenching of lysozyme type VI stabilized gold nanoclusters. *Anal Chem* 2010;**82**:9194-200.
285. Kawasaki H, Hamaguchi K, Osaka I, Arakawa R. pH dependent synthesis of pepsin-mediated gold nanoclusters with blue green and red fluorescent emission. *Adv Func Mater* 2011;**21**:3508-15.
286. Kawasaki H, Yoshimura K, Hamaguchi K, Arakawa R. Trypsin-stabilized fluorescent gold nanocluster for sensitive and selective Hg^{2+} detection. *Anal Sci* 2011;**27**:591

287. Shao C, Yuan B, Wang H, Zhou Q, Li Y, Guan Y, *et al*. Eggshell membrane as a multimodal solid state platform for generating fluorescent metal nanoclusters. *J Mater Chem* 2011;**21**:2863-6.
288. Shi H, Ou M, Cao J, Chen G. Synthesis of ovalbumin-stabilized highly fluorescent gold nanoclusters and their application as an Hg^{2+} sensor. *RSC Adv* 2015;5:86740-5.
289. Chen Y, Wang Y, Wang C, Li W, Zhou H, Jiao H, *et al*. Papain-directed synthesis of luminescent gold nanoclusters and the sensitive detection of Cu^{2+}. *J Colloid Interface Sci* 2013;**396**:63-8.
290. Joseph D, Geckeler KE. Synthesis of highly fluorescent gold nanoclusters using egg white proteins. *Colloids Surf B* 2014;**115**:46-50.
291. Xavier PL, Chaudhari K, Verma PK, Pal SK, Pradeep T. Luminescent quantum clusters of gold in transferrin family protein, lactoferrin exhibiting FRET. *Nanoscale* 2010;**2**:2769-76.
292. Wen F, Dong Y, Feng L, Wang S, Zhang S, Zhang X. Horseradish peroxidase functionalized fluorescent gold nanoclusters for hydrogen peroxide sensing. *Anal Chem* 2011;**83**:1193-6.
293. Yan L, Cai Y, Zheng B, Yuan H, Guo Y, Xiao D, *et al*. Microwave-assisted synthesis of BSA stabilized and HSA protected gold nanoclusters with red emission. *J Mater Chem* 2012;**22**:1000-5.
294. Liu JM, Lin LP, Wang XX, Lin SQ, Cai WL, Zhang LH, *et al*. Highly selective and sensitive detection of Cu^{2+} with lysine enhancing bovine serum albumin modified-carbon dots fluorescent probe. *Analysis* 2012;**137**:2637-42.
295. Bhamore JR, Jha S, Basu H, Singhal RK, Murthy Z, Kailasa SK. Tuning of gold nanoclusters sensing applications with bovine serum albumin and bromelain for detection of Hg^{2+} ion and lambda-cyhalothrin via fluorescence turn off and on mechanisms. *Anal Bioanal Chem* 2018;1–11.
296. Liu CL, Wu HT, Hsiao YH, Lai CW, Shih CW, Peng YK, *et al*. Insulin-directed synthesis of fluorescent gold nanoclusters: preservation of insulin bioactivity and versatility in cell imaging. *Angew Chem Int Ed* 2011;**50**:7056-60.
297. Choudhury D, Xavier PL, Chaudhari K, John R, Dasgupta AK, Pradeep T, *et al*. Unprecedented inhibition of tubulin polymerization directed by gold nanoparticles inducing cell cycle arrest and apoptosis. *Nanoscale* 2013;5:4476-89.
298. Chen PF, Liu CL, Lin WK, Chen KC, Chou PT, Chu SW. Fluorescence depletion properties of insulin–gold nanoclusters. *Biomed Opt Express* 2015;**6**:3066-73.

299. Shang L, Dong S. Facile preparation of water-soluble fluorescent silver nanoclusters using a polyelectrolyte template. *Chem Commun* 2008;**9**:1088-90.
300. Shang L, Dong S, Nienhaus GU. Ultra-small fluorescent metal nanoclusters: synthesis and biological applications, *Nano Today* 2011;**6**:401-18.
301. Lin YF, Cheng CW, Shih CS, Hwang JK, Yu CS, Lu CH. MIB: metal ion binding site prediction and docking server. *J Chem Inf Model* 2016;**56**:2287-91.
302. Lu CH, Lin YF, Lin JJ, Yu CS. Prediction of metal ion–binding sites in proteins using the fragment transformation method. *PLoS One* 201;**27**:e39252.
303. Lu CH, Lin YS, Chen YC, Yu CS, Chang SY, Hwang JK. The fragment transformation method to detect the protein structural motifs. *Proteins* 2006;**63**:636-43.
304. Xie J, Zheng Y, Ying JY. Protein directed synthesis of highly fluorescent gold nanoclusters. *J Am Chem Soc* 2009;**131**:888-9.
305. Liu CL, Wu HT, Hsiao YH, Lai CW, Shih CW, Peng YK, *et al*. Insulin-directed synthesis of fluorescent gold nanoclusters: preservation of insulin bioactivity and versatility in cell imaging. *Angew Chem Int Ed* 2011;**50**:7056-60.
306. Lin J, Zhou Z, Li Z, Zhang C, Wang X, Wang K, *et al*. Cui, Biomemetic one-pot synthesis of gold nanoclusters/ nanoparticles for targeted tumor cellular dual-modality imaging. *Nanoscale Res Lett* 2013;**8**:170.
307. Murzin AG, Brenner SE, Hubbard T, Chothia C. SCOP: a structural classification of proteins database for the investigation of sequences and structures. *J Mol Biol* 1995;**247**:536-40.
308. Lu CH, Lin YS, Chen YC, Yu CS, Chang SY, Hwang JK. The fragment transformation method to detect the protein structural motifs. *Proteins* 2006;63:636-43.
309. Gower JCRG. Minimum spanning trees and single-linkage clusteranalysis. *J Royal Stat Soc* 1969;**18**:11.
310. Goswami N, Giri A, Bootharaju MS, Xavier PL, Pradeep T, Pal SK. Copper quantum clusters in protein matrix: potential sensor of Pb^{2+} ion. *Anal Chem* 2011;**83**:9676-80.
311. Moniri S, Ghoranneviss M, Hantehzadeh MR, Asadabad MA. Synthesis and optical characterization of copper nanoparticles prepared by laser ablation. *Bull Mater Sci* 2017;**40**:37-43.
312. Wagner CC, Baran EJ. Vibrational spectra of bis (L-methioninato) copper (II). *Acta Farm Bona* 2002;**21**:287-90.
313. Child MD, Percy GC. Band assignments in the infrared spectra of some metal (II) complexes of Pyrazine. *Spectrosc Lett* 1977;**10**:71-8.

314. Rao C, Venkataraghavan R, Kasturi T. Contribution to the infrared spectra of organosulphur compounds. *Can J Chem* 1964;**42**:36-42.
315. D'Souza L, Devi P, Divya Shridhar M, Naik CG. Use of Fourier Transform Infrared (FTIR) spectroscopy to study cadmium-induced changes in Padina tetrastromatica (Hauck). *Anal Chem Insights* 2008;**3**:117739010800300001.
316. Deb P, Haldar T, Kashid SM, Banerjee S, Chakrabarty S, Bagchi S. Correlating nitrile IR frequencies to local electrostatics quantifies noncovalent interactions of peptides and proteins. *J Phys Chem B* 2016;**120**:4034-46.
317. Baran EJ. Structural data and vibrational spectra of the copper (II) complex of L-selenomethionine. *Z Naturforsch* 2005;**60**:663-6.
318. Skripkin MY, Lindqvist Reis P, Abbasi A, Mink J, Persson I, Sandström M. Vibrational spectroscopic force field studies of dimethyl sulfoxide and hexakis (dimethyl sulfoxide) scandium (III) iodide, and crystal and solution structure of the hexakis (dimethyl sulfoxide) scandium (III) ion. *Dalton Trans* 2004;**23**:4038-49.

SUMMARY

Wound, loss of continuity of tissue structure (such as skin, muscle, nerves, blood vesicles, bones, etc) caused due to mechanical (such as friction, pressure, heat or cold), chemical, electrical, or radiation force exposure.[1,2] Wounds have chronic pain or completely painless, swelling (redness, heat, swelling, pain, and loss of function), susceptible to infection are the signs.[3] Wounds are either internal or external based on their origin. Internally originated wounds also like ingrown toenails or calluses, break the skin and surrounding tissue, create an external wound and open wounds; due to environmental exposure is prone to infection.[4] To prevent infection; initiate a series of dynamic events, collectively known as the wound healing process.[5] But the chronic wound is characterized by a persistent rise of pro-inflammatory cytokines and low anti-inflammatory cytokines and growth signal and is a major issue for patients undergoing surgery.[6] Chronic wounds result in isolation, pain, anxiety, frustration, discomfort, and also lead to depression in patients.[7,8] All conditions affect the normal life, emotions, behavior, and thought pattern of the patient and ruin the quality of life.[9]

The wound healing process riles on activation of a cascade of physiological events such as hemostasis, inflammation, proliferation, and remodeling.[10] The inflammation plays an important role throughout this process, the fast recovery of the wound depends on the transition of pro-inflammatory (M1 macrophages) to anti-inflammatory (M2 macrophages) and in chronic wounds, delay in transition in chronic wounds result in a prolonged proinflammatory phase leading to delay in wound healing.[11] In the early phase, macrophage functions through the release of cytokines (including IL-6, IL-12, IL-1β, and TNF-α, etc) and activating leucocytes to produce proinflammatory response.[12] Secretion of anti-inflammatory cytokines (including IL-4, IL-10, IL-13, and TFG-β, etc) is responsible for the closure of the wound and induces angiogenesis and re-epithelialisation.[13]

Numerous approaches including various kinds of dressings stem cell-based therapies and the use of growth factors (epithelial growth factor, platelet-derived growth factor, fibroblast growth factor, transforming growth factor-beta, and insulin-like growth factor-1) have been targeted to treat chronic wounds.[14] Despite potential usefulness is limited due to limitation including moisture associated delaying (alginates based dressings), reduced aeration (hydrocolloid based dressings), low mechanical strength (hydrogels based dressing), the high cost (stem cell and growth factors based therapies), and increase in the economic burden.[15-20] Healing of wound attained the great attention of investigators but promising

therapeutic intervention is still awaited. Insulin is one of the most common and effective therapeutic choices for the treatment of diabetes type-I; it acts as an anti-inflammatory agent by activating cytokines which can reduce inflammation and promotes glucose uptake by cells thereby helping maintenance of blood glucose level.[21] Insulin also works as a cellular growth promotes and works through insulin-like growth factor receptor-I (IGFR-I) binding.[22]

According to the International Diabetes Federation (IDF) data till 2019, 463 million people were having diabetes.[23] IDF estimates that by 2045 the diabetic cases raise from 628 to 700 million.[23,24] The patients suffering from diabetes are at 25% risk of developing foot ulcers.[25] More than 6% of diabetic ulcer patients needing clinical attention among which 15-20% will need amputation of lower limb due to worsening of the wound.[26] Despite so many uses of insulin as anti-diabetic agents, it has rarely been explored for its wound healing activities.

Keeping the above points in view, the following objectives have been designed

1. Development of different insulin based nanoformulations and their characterization.
2. *In vitro* cell migration assay using different insulin nanoformulations.
3. Evaluation of selected nanoformulations for wound healing activity in the diabetic condition.

In the present work, the wound healing mechanism of insulin had been proposed and three different formulations of protein i.e. insulin capped silver nanoparticles (IAgNPs), amorphous insulin zinc quantum clusters (IZnQCs), and crystalline insulin copper quantum clusters (ICuQCs) had been prepared. Further, these formulations were been investigated for their *in vitro* wound healing activity using Human cell lines (HEKa, A549, and HeLa). In addition to this IAgNPs were further used for *in vivo* wound healing activity testing on Wister rat models.

Chapter 2: Mechanism of wound healing by insulin

2.1. Mechanism of wound healing by insulin

Insulin is a peptide hormone, helps in controlling diabetes. It can also act as an anti-inflammatory agent by activating cytokines which can reduce inflammation and help to recover the wound. Also, through metabolism and synthesis activities, it plays an important role in cell differentiation and survival. Insulin promotes up-regulation of $NFk\beta^{P50/P50}$ by suppression of p65 expression and TNF-α. Suppression of $NFk\beta^{P50/P65}$ decreases the expression of IL-6, IL-1β, IL-12, and TNF-α cytokines in the wound site. Inhibition of proinflammatory cytokines drives the equilibrium toward the expression of anti-inflammatory

cytokines, such as IL-10, IL-4, VEGF, etc, which inhibits cellular apoptosis and induces cell proliferation like IGF. In the following section the regulation of the dynamics of cytokines under the influence of insulin a) inactivated $NFk\beta^{P50/P65}$ to decrease inflammation by inducing glucose uptake, b) induces fatty acid biosynthesis and thereby inactivates the TNF-α mediated inflammatory pathway, c) induces cell growth and differentiation by protein synthesis and inhibits proteolysis through FOXO inactivation to promote cell survival, d) behaves as an IGF growth factor and can activate the same signaling pathway to reduce inflammation, and e) modulates inflammation through the reduction of proinflammatory cytokines and inducing anti-inflammatory cytokines.

2.2. Insulin modulates inflammation through the reduction of proinflammatory cytokines and inducing anti-inflammatory cytokines

In a normal wound, the healing process relies on the activation of a cascade of physiological events such as inflammation, proliferation, epithelisation, vascularisation, maturation, and remodeling at the scar site. Macrophages play an important role throughout the whole process. In the early wound healing phase, macrophages function through the release of cytokines and activating leucocytes to produce an inflammatory response.

Macrophage infiltration takes place into the wound site due to chemotaxis induced by factors such as PDGF, LPS (Lipopolysaccharide), PAMP (Pathogen-associated molecular patterns), Toll-like receptor (TLR) ligand, and IFN-gamma (IFN-ϒ). M1 is responsible for the secretion of high levels of IFN-β/TNF-α, and STAT1. Insulin via PI3/Akt pathway activates STAT3 which inhibits STAT1 synthesis and induces class switching of M1 to M2 macrophages repair macrophages that function in the constructive process like in tissue repair and wound healing. M2 macrophages also produce polyamines and ornithine through the arginase pathway and anti-inflammatory IL-4, IL-10, and IL-13 cytokines. Insulin together with M2 macrophages induced anti-inflammatory activates PI3K/Akt pathway to induce protein and fatty acid biosynthesis, cell division, cell migration, and angiogenesis to promote wound recovery. In diabetes with insulin resistance, there are consistently elevated levels of TNFα and IL-6, the proinflammatory cytokines have been shown. In normal glycemic conditions, the adipocytes produce cytokines, like IL-13, that promotes the activation of alternative or M2 macrophages. M2 or activated macrophages are responsible for the secretion of anti-inflammatory cytokines like IL-10 and may secrete insulin-sensitizing factors, PPAR-ϒ (Peroxisome Proliferator-Activated Receptor Gamma), which generates a

vicious circle for insulin activity. PPAR-ϒ can also activate the anti-inflammatory cytokine IL-10 (**Figure 1**).

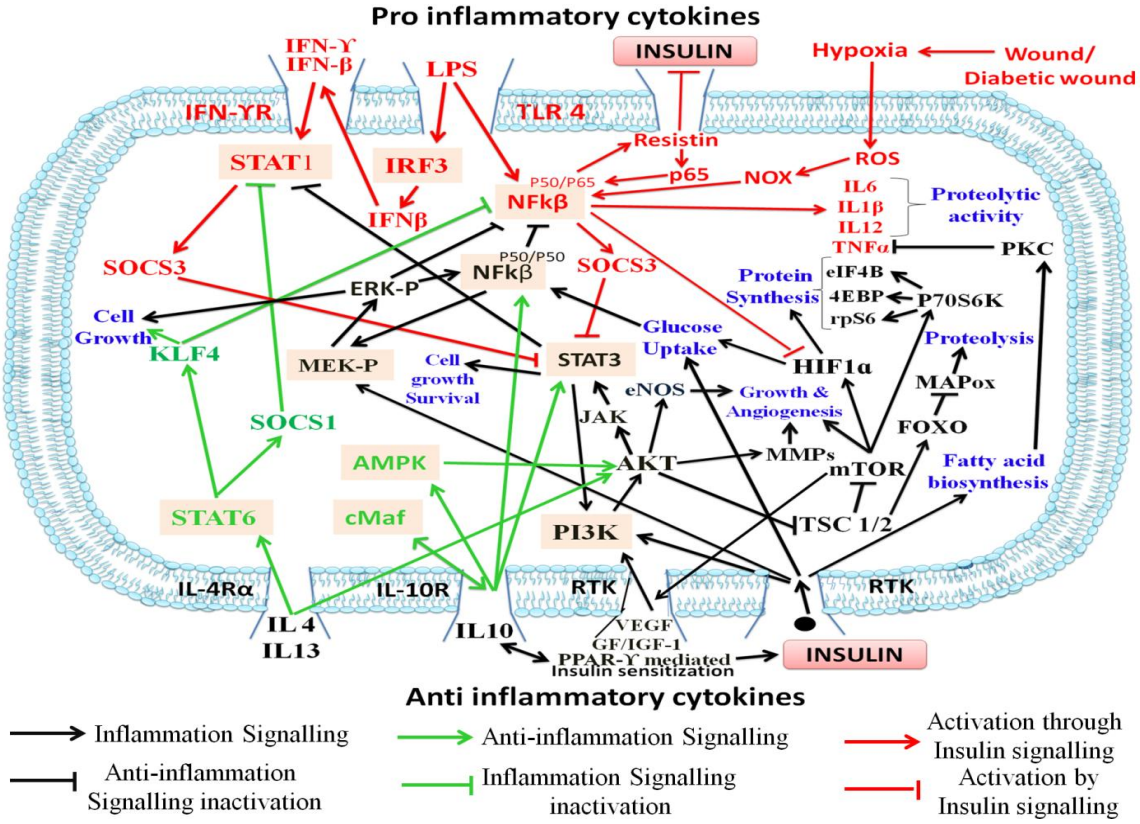

Figure 1: Molecular pathway for the transition of macrophages i.e. from the M1 to M2 phase. IFN-ϒ and TNF-α generation in wounds activates NFkβ, IRF-3, STAT1 which helps in secretion of IL-10, IL-1β, IL-12, TNF-α, STAT1 and NFkβ$^{P50/P65}$, responsible for inflammation. The transition of M1 to M2 macrophages is necessary for wound healing. IL-4, IL-13, IL-10, IGF, VEGF, and insulin can activate PKC, HIF-α, STAT3, and NFkβ$^{P50/P50}$, etc cytokines to produce an anti-inflammatory effect.

In the diabetic condition, there is a prolonged-expression of the pro-inflammatory macrophage phenotype sustained by IL-1β and TNF-α, and wound healing gets impaired. Overexpression of IL-1β, TNF-α, or IL-17 cytokines decrease the expression of inflammatory cytokines, upregulates wound healing related genes, and accelerates the healing of wounds. Furthermore, adipose tissue and the blood have elevated TNF-α cytokines, and TNF-α neutralization improves the sensitivity of insulin in the animals. Diabetes induces changes in gene expression and metabolism in adipocytes and results in increased lipolysis and production of free fatty acids (FFAs) and pro-inflammatory factors that recruit and induce activation of macrophages, such as monocytes chemotactic protein-1 (MCP-1) and tumor

necrosis factor α (TNF-α). Activation of M1 macrophages produces a huge concentration of inflammatory cytokines, like IL-1β, resistin, and TNF-α that acts on adipocyte cells to make them insulin resistant. This signaling forms a kind of feedback loop that increases inflammation and resistance to insulin. TNF-α, an inflammatory cytokine, plays an important role in the normal healing process, but its activation for a long period leads to an increase in protease activity. In non-healing wounds of humans, MMPs were detected at very high concentrations. In chronic or inflamed wounds, there is an imbalance in pro-inflammatory cytokines and their inhibitors, proteases, and their anti-proteases expression. The role of insulin in the transition from inflammatory to anti-inflammatory state and M1 and M2 macrophages transition is depicted in **Figure 1**.

Chapter 3: Synthesis, characterization, *in vitro* wound healing activity, *in vivo* wound contraction assay and anti-inflammatory effect of insulin capped silver nanoparticles (IAgNPs)

3.1. Synthesis

Aqueous Tulsi (*Ocimum tenuiflorum*) leaf extract (ATE) was prepared by boiling 3 g tulsi leaves in 100 ml water for 2h. After cooling and filtration pH of the solution was adjusted to 7.4 and preserved at 4°C. Synthesis of AgNPs was carried out by using ATE as a capping and reducing agent. 240 µM $AgNO_3$ was added in 5000 µl of ATE and was kept under sunlight for 10 min. The color of the solution changed from faint light yellow to reddish-brown under the sunlight. After this, AgNPs were incubated with insulin at physiological temperature (37°C) in an incubator for an hour to produce insulin protected AgNPs (IAgNPs) shown in **Figure 2**.

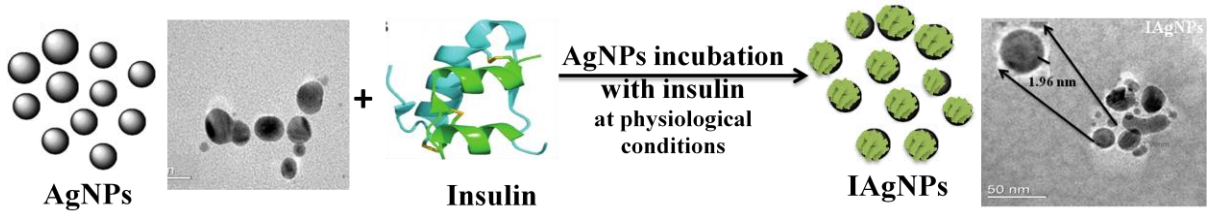

Figure 2: Schematic presentation of the formation of nano-insulin formulation (IAgNPs).

3.2. Characterization

The nanoparticles' surface plasmon resonance, hydrodynamic diameter and stability, and thermodynamic binding parameters using protein internal fluorescence were determined. Using Surface-Enhanced Raman Scattering (SERS) and FTIR spectra structural changes in

insulin protein were observed. Far Ultra Violet Circular dichroism (Far UV CD) measurements were carried out to identify changes in secondary structures of insulin due to interaction. The morphological studies like the size of particle and size distribution of the biosynthesized AgNPs and IAgNPs were studied by placing the solution of samples on carbon-coated TEM grids (400 meshes) by using Transmission Electron Microscope. The number of the protein binds to a single AgNP was determined by the Bradford protein assay.

3.3. *In vitro* wound healing

IAgNPs induced higher HEKa cell migration in comparison to control in experimental sets containing glucose concentration 100, 180, and 360 mg/dl. The extent of migration increased with the increase of time and IAgNPs concentration (**Figure 3A**). After 24h, IAgNPs treated HEKa cells (**Figure 3B**) for normal glycemic (100 mg/dl) and moderate hyperglycaemic conditions (180 mg/dl) showed an increased migration of almost 25% and 27% respectively (**Figure 3C**) whereas 360 mg/dl glucose concentration (**Figure 3C**) showed almost 31% faster cell migration compared to vehicle-treated control, indicating the higher wound healing activity in higher hyperglycaemic conditions.

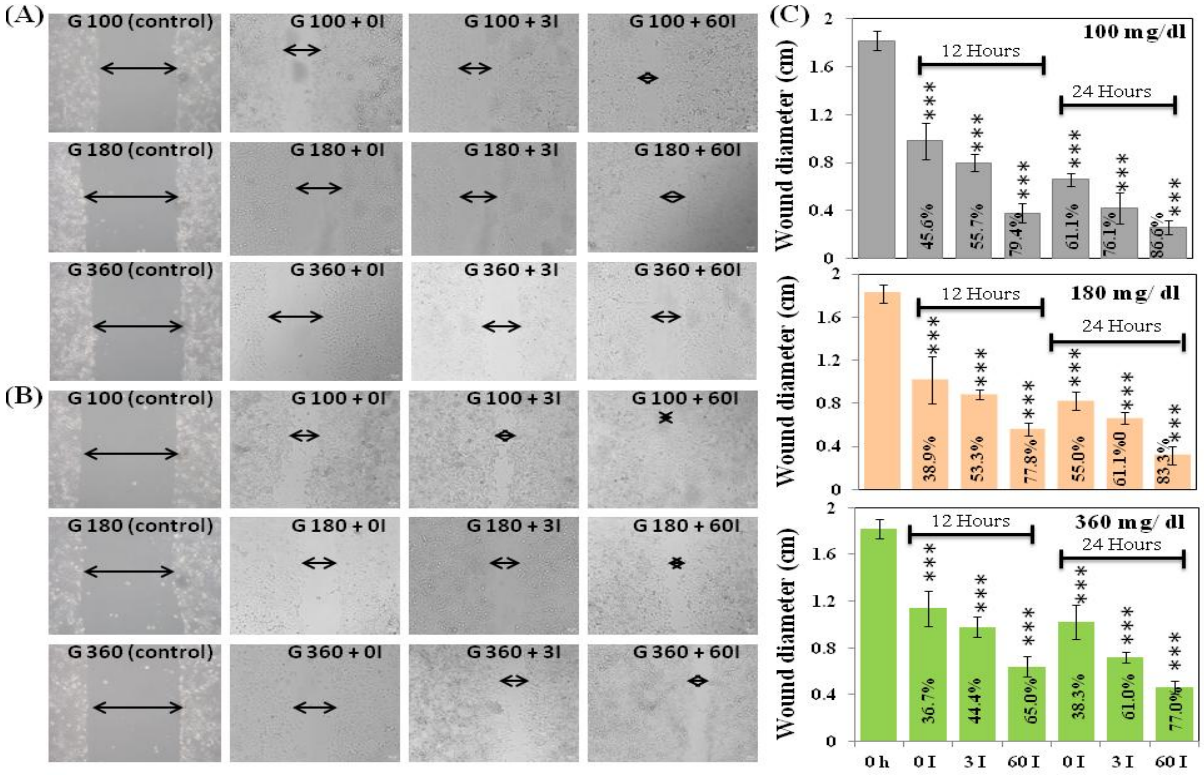

Figure 3: HEKa epithelial cell migration (A) after 12h & (B) 24h and Bar graphs (C) showing cell migration (in cm) at 12h and 24h with different Glucose and IAgNPs

concentration (G = Glucose in mg/dl and I = Molar Concentration of IAgNPs in pM). The statistical significance of the data shown with "*": *** P<0.001, ** P<0.01, and * P<0.05.

3.4. *In vivo* wound contraction assay

3.4.1. Assessment of wound recovery *in vivo*: Full-thickness excision the wound of diameter 15 mm was created initially in all animals (**Figure 4A**) and treated non-diabetic and diabetic animals showed significant variation in the initiation and completion of wound closure in comparison with control. Early and later phases of healing on the 5th and 11th days respectively, indicating important phases of healing, were chosen to measure further biochemical and histological parameters simultaneously.

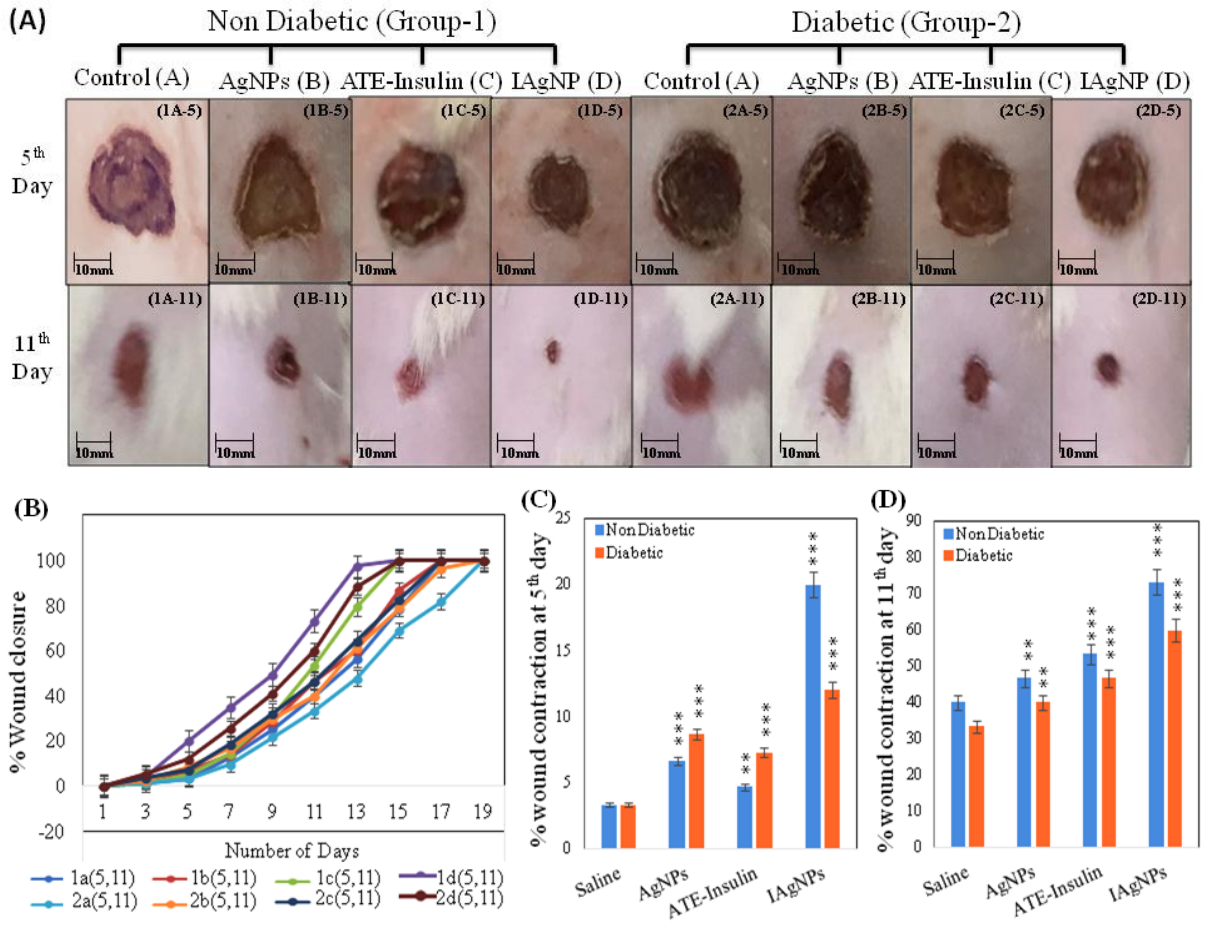

Figure 4: Healing rate of the wound by AgNPs, ATE-insulin, and IAgNPs treatment in both diabetic and non-diabetic animals on the 5th and 11th day. (A) Physical observation of wound contraction in various groups of treatment and control, (B) % wound closure in different treatment groups (AgNPs, ATE-Insulin, and IAgNPs), and respective controls in diabetic and non-diabetic animals until complete wound closure. (C) Represents the % wound contraction in all four subgroups of diabetic and nondiabetic animals on the 5th day. (D) Represents the %

wound contraction in all four subgroups of diabetic and non-diabetic animals on the 11th day. All values are represented by an average ± SD of 6 rats in the group. The statistical significance of the data shown with "*": *** P<0.001, ** P<0.01, and * P<0.05.

The % closure of the wound, measured until the full closure of wound obtained, in treated diabetic and non-diabetic groups along with the vehicle-treated control groups is expressed in F**igure 4B** which indicate the accelerated rate of wound healing in different treatment groups both in nondiabetic as well as a diabetic condition compared to respective control groups. Precisely, on the 5th day, the percentages of wound healing in non-diabetic and diabetic rats were significantly improved (20% and 12% respectively) by topical application of IAgNPs treatment in comparison to normal and diabetic control groups (3.33%) (**Figure 4C**). A slightly higher wound healing was observed with AgNPs treatment (6.67% and 8.67% in normal and diabetic groups) or insulin-ATE treatment (4.67% and 7.27% in normal and diabetic groups) in comparison to control (3.33%) (**Figure 4C**). No significant difference was observed between healing in non-diabetic and diabetic control group animals on the 5th day. A similar pattern was observed on the 11th day of treatment (**Figure 4D**). IAgNPs showed significantly higher wound closure in both normal and diabetic rats (73.33% and 60.0% respectively) in comparison to normal and diabetic controls (40% and 33.33% respectively). AgNPs showed sub-moderate (46.67% and 40.0% in normal and diabetic groups) and Insulin-ATE showed moderately better (53.33% and 46.67% normal and diabetic groups) wound healing efficacy compared to respective control groups (**Figure 4D**).

3.4.2. Evaluation of histology and assessment of inflammatory cytokines: Histological section of non-diabetic animals on the 5th day showed a significantly increased level of lymphocytes cells and initiation of collagen deposition near the excision line of the wound. Exudates formation is responsible for leukocyte infiltration which slows down the healing of the wound. The demarcation line represents the complete separation of exudates and re-epithelization was completely absent in 5thday non-diabetic controls (**Figure 5A**). The histological section of diabetic animals showed a higher accumulation of exudates as compared to non-diabetic animals which confirm the initiation of inflammatory events (**Figure 5A**). Commencement of collagen deposition significantly favors strengthening of surrounding muscles to fast closure of the wound, a featured that was found delayed in diabetic groups (**Figure 5A**). On 5th the day, the re-epithelization was insignificant in all groups of diabetic animals compared to non-diabetic ones. Although, AgNPs, ATE-Insulin,

and IAgNPs treatment in both groups caused a significant reduction of exudates accumulation compared to saline-treated controls (**Figure 5A**). Photomicrographs of the 11th day showed complete re-epithelization in the non-diabetic animals whereas partial re-epithelization was observed in diabetic animals (**Figure 5B**). However, the treatment of IAgNPs in diabetic animals showed complete re-epithelization that was similar to the non-diabetic control group (**Figure 5B**). Additionally, individual treatment of AgNPs, ATE-Insulin, and IAgNPs has shown substantial improvement in collagen deposition in both groups in comparison with corresponding matched controls (**Figure 5B**). Histological data showing good remodeling in treated groups prompted us to evaluate different pro-inflammatory and anti-inflammatory cytokines in the wound milieu. Following IAgNPs treatment quantification of serum IL-6, TNF-α, and IL-10 levels were performed in all groups of animals (**Figure 5C, D,** and **E**). On the 5th day, a 25% higher level of serum IL-6 (**Figure 5C**) and 2-fold higher levels of serum TNF-α (**Figure 5D**) concentration were evaluated in diabetic rats compared to non-diabetic control. IAgNPs treatment showed 50% inhibition in both groups (**Figure 5C** and **D**). Treatment with AgNPs, and insulin-ATE also showed a moderate to a high reduction in these pro-inflammatory cytokine levels in both groups of animals (**Figure 5C** and **D**). Furthermore, the increase of concentration of the anti-inflammatory cytokine IL-10 increased by 70% and 50% in normal and diabetic animals respectively by IAgNPs treatment on the 5th day (**Figure 5E**). AgNPs showed only a slight increase in serum IL-10 level whereas insulin-ATE also showed almost 45% and 30% increased anti-inflammatory cytokine concentration as compared with normal and diabetic controls (**Figure 5E**). Even on the 11th day of treatment, diabetic control animals had a higher level of IL-6, and TNF-α (30% and 50% respectively) as compared to non-diabetic controls. However, the treatment of IAgNPs significantly reduces their level (about 45% of IL-6 and 45% of TNF-α) in both sets of diabetic and non-diabetic. Additionally, a moderate reduction in both pro-inflammatory cytokines was observed in diabetic and non-diabetic animals by individual treatment of AgNPs (IL-6, 10% and TNF-α, 10%) and ATE-Insulin (IL-6, 40% and TNF-α, 30% respectively). Both individual treatment (AgNPs and ATE-Insulin) also increased anti-inflammatory cytokines (IL-10) by about 45% and 50% respectively in diabetic and non-diabetic animals. However, the treatment of IAgNPs showed a higher potential to upsurge the level of IL-10 in both sets of non-diabetic and diabetic animals (65% and 50% respectively). Overall, pro-inflammatory and anti-inflammatory cytokines decreased in the case of all animals on the 11th day showing the neutralization of the inflammatory stage. A faster neutralization was observed with IAgNPs treatment in comparison with respective control groups of diabetic and non-diabetic

animals (**Figure 5C, D,** and **E**). These results indicate an unprecedented mechanism of regulation of the early inflammatory phase by insulin.

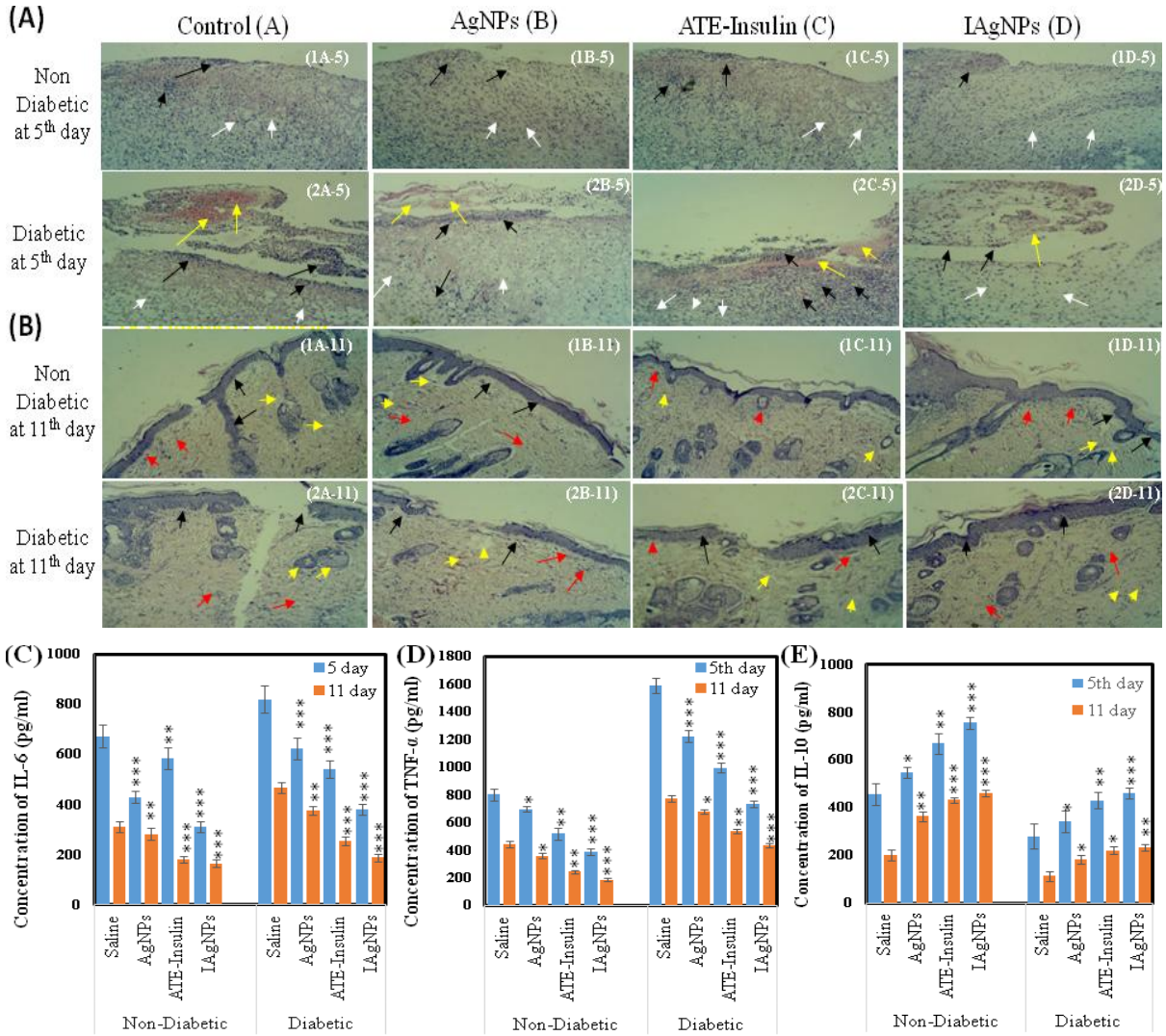

Figure 5: Histological evaluation at the wound site of different groups (40X) on the 5th and 11th day of post-treatment (Figure 5A and B respectively); Leukocyte infiltration, collagen deposition, and exudates formation are denoted by red, white, and yellow arrows respectively. Each slide represents the overall pattern of a group of 6 rats. C, D, and E represent the concentration of pro-inflammatory (IL-6, and TNF-α) and anti-inflammatory cytokines (IL-10) in all subgroups of diabetic and nondiabetic animals on the 5th and 11th day. Results show a significant reduction of proinflammatory cytokines (IL-6, and TNF-α) and increased level of anti-inflammatory cytokines (IL-10) by IAgNPs treatment as compared to control, AgNPs and ATE-Insulin treated animals of both sets on 5th and 11th day respectively. All values are represented by an average ± SD of 6 rats in the group. The statistical significance of the data shown with "*": *** P<0.001, ** P<0.01, and * P<0.05.

Chapter 4: Synthesis, characterization, and *in vitro* wound healing activity of insulin zinc quantum clusters (IZnQCs)

4.1. Synthesis

Insulin metal quantum clusters synthesis was performed by using insulin and $ZnSO_4$ salt solution of 1.82 µM concentration in an aqueous medium. The insulin pH was adjusted to basic (10.5) using NaOH solution and then dialyzed using 3 kDa cut off dialysis membrane (SOLUTION A) and 1.82 µM solution of $ZnSO_4$ (SOLUTION B) was taken. After preparing both the solutions, the insulin was added to the metal salt solution in 1:1 volume, after mixing both the solutions the pH was adjusted to 7.4 (physiological pH) by using the HCl (0.1 N). The resulting solution was kept in an incubator at 37°C for 12h at stirring (240 rpm) and it results in the formation of insulin Zinc quantum clusters (IZnQCs) shown in **Figure 6**.

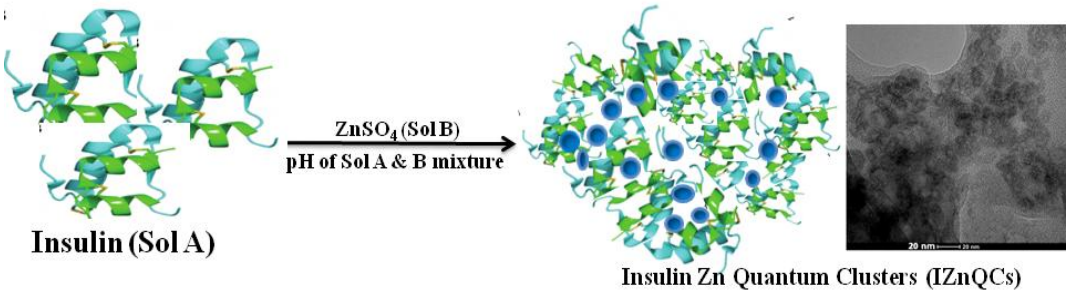

Figure 6: Shows the formation of insulin zinc quantum clusters (IZnQCs).

4.2. Characterization

UV absorption spectra, High-resolution transmission electron microscopy (HRTEM), selected area electron diffraction (SAED), and FTIR Spectrophotometer studies were performed to confirm the synthesis of IZnQCs. The quantum yield was determined using fluorescence spectrophotometer studies.

4.3. *In vitro* Assay

Insulin and zinc are known for their wound healing activity by altering the inflammatory dynamic. Insulin binding to IR and phosphorylate the tyrosine kinase receptor for its activity. Zinc is also known to work through the same pathway and in the absence of insulin, the prolonged exposure of Zn leads to the tyrosine phosphorylation present on IR and plays a similar role as insulin. The similar role of IZnQCs has been tested using HEKa (Normal human epidermal keratinocyte).

4.3.1. Cell viability: Cell division activity or viability on HEKa using 1.5, 7.5, 30, and 60 µM different amounts of controls (Zn salt, insulin, I + Zn), and IZnQCs. Zn + I treated cells

shows 1.5 µM (107.31 ± 7.29%), 7.5 µM (116.849 ± 5.98%), 30 µM (131.466 ± 22.05%), and 60 µM (148.762 ± 24.66%) cell viability. Insulin shows 1.5 µM (102.38 ± 12.8%), 7.5 µM (129.19 ± 3.94%), 30 µM (133.05 ± 6.65%), 60 µM (148.11 ± 3.32%). The cells exposed to Zn salt also showed more cell viability in 1.5 µM (104.08 ± 13.49%), 7.5 µM (123.18 ± 8.88%), 30 µM (126.71 ± 8.67%), and 60 µM (131.51 ± 1.811%). Cell division after IZnQCs treatment showed more significant changes in 1.5 µM treatment (132.24 ± 7.29%), 7.5 µM (175.94 ± 5.64%), 30 µM (186.07 ± 22.81%), and 60 µM (188.71 ± 16.95%) in comparison to treated and untreated controls. The results suggested that these quantum clusters have the potential to enhance cell division and can help in wound healing. The IZnQCs shows 32.26 ± 7.29% more division in 1.5 µM concentration, in 7.5 µM, 30 µM, and 60 µM 75.92 ± 5.64%, in 86.07 ± 22.81%, and 88.71± 16.94% respectively more division in comparison to control. The measurements were statistically significant.

4.3.2. Bioimaging: Confocal imaging was performed to confirm the cellular imaging application of insulin metal quantum clusters. HEKa cell line incubated with 1% IZnQCs or insulin (in control) for 2h, cells were treated with RNase A for 3h at 37°C. Thereafter cells were incubated with 1 µg/ml of propidium iodide (PI) before imaging. IZnQCs treated cells showed bright blue fluorescence as a result of the binding of the IZnQCs with the insulin receptors present on the surface of the cells. With $ZnSO_4$ no fluorescence was observed for the same cell lines shown in **Figure 7(A-H)**. As, the quantum yield 0.021 and 0.112 for insulin and IZnQCs respectively, blue fluorescence was observed in the IZnQCs cells.

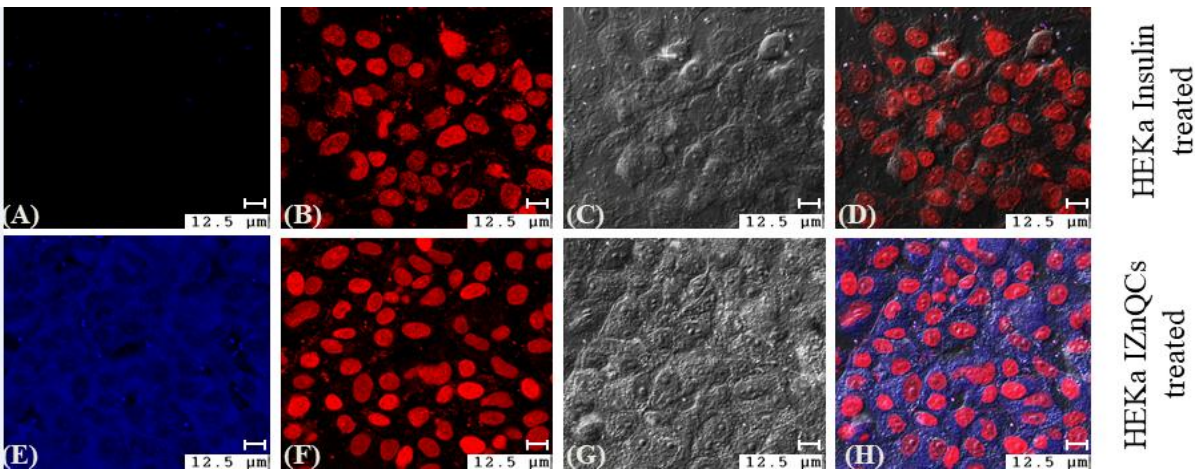

Figure 7: Bioimaging of HEKa cells using Zn-insulin quantum clusters. HEKa cells (A) insulin treated, (B) PI stained nucleus, (C) cell phase image, (D) insulin treated and non

treated cells merged imaged, (E) IZnQCs treated, (F) PI stained nucleus, (G) cell phase image, and (H) IZnQCs non-treated and treated cells merged image.

4.3.3. Cell migration assay: IZnQCs induced HEKa cell migration in comparison to treated (Zn salt, insulin, I + Zn), and untreated controls. The extent of cell division and migration increased with the increase in concentration and time and was monitored using a fluorescence microscope (**Figure 8A**).

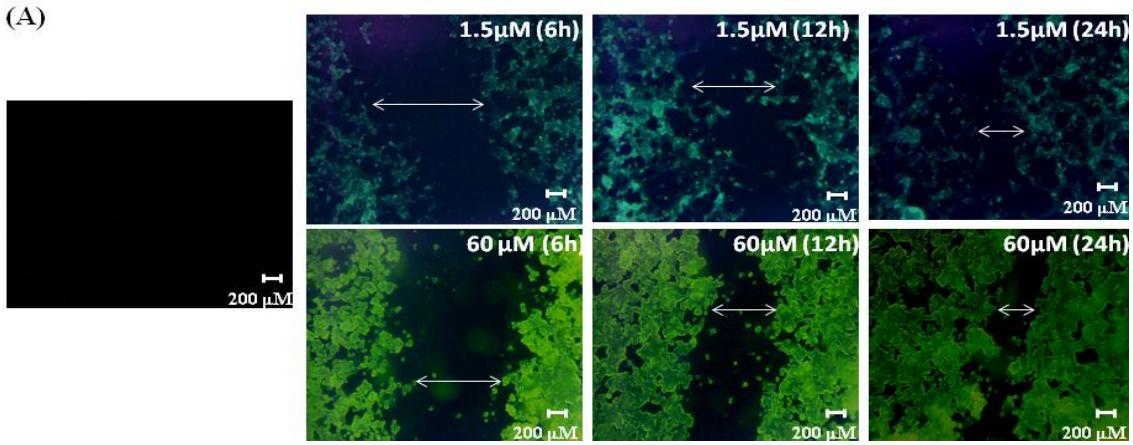

Figure 8: Promotion and monitoring of wound healing in under phase contrast and fluorescence microscopy using IZnQCs. (A) fluorescence imaging of cells at IZnQCs different concentrations (1.5 and 60 µM) and incubation time (6, 12, and 24h).

The cells treated with IZnQCs for 6, 12, and 24h shows 39.49 ± 1.29%, 27.58 ± 3.72%, and 43.02 ± 1.62% at 1.5 µM and 52.88 ± 0.83%, 46.86 ± 1.46%, and 67.81 ± 0.83% for 60 µM cell migration respectively in comparison to untreated control scratch diameter. In addition to these concentrations, the cells were also treated with 7.5 µM and 30 µM concentration of IZnQCs. Cells show 42.03 ± 3.04%, 34.08 ± 1.57%, and 46.51 ± 3.38% migration after treatment with 7.5 µM IZnQCs and 45.25 ± 2.14%, 36.32± 1.63%, and 58.60 ± 0.72% at 30 µM concentrations of IZnQCs at 6, 12 and 24h respectively. Along with IZnQCs treatment; the cells also treated with Zn salt, insulin, I + Zn, show significant migration in comparison to control. With 1.5 µM Zn salt addition to cells, 21.18 ± 3.72%, 0.224 ± 0.030%, and 18.60 ± 2.4% migration, at 7.5 µM Zn salt 22.88 ± 1.27%, 12.11 ± 0.59%, and 35.58 ± 0.76% enhancement in cell growth, with 30 µM 45.25 ± 2.56%, 26.01 ± 3.49%, and 39.07 ± 2.86% wound closure and after 60 µM treatment 49.97 ± 4.69%, 33.86 ± 1.96%, and 45.81 ± 5.09% more cell migration at 6, 12, and 24h respectively in relation to control. Similarly, cells treated with insulin, 1.5 µM insulin treatment, 39.49 ± 1.61%, 20.18 ± 1.29%, and 29.30 ± 1.28% and migration, with 7.5 µM insulin concentration 42.03 ±

1.35%, 24.89 ± 5.17%, and 41.26 ± 2.03% cell growth enhancement, with 30 µM 45.25 ± 2.50%, 32.51 ± 0.38%, and 51.39 ± 3.22%, closure of the wound and after 60 µM treatment 52.88 ± 0.8 %, 45.067 ± 7.07%, and 63.72 ± 1.66% more migration of cell at 6, 12 and 24h respectively in relation to untreated control. With only Zn + I treatment, 1.5 µM concentration treatment, 40.3 ± 1.04%, 26 ± 3.5%, and 29.3 ± 3.8% migration, with 7.5 µM Zn + I concentration 44.3 ± 0.74%, 33 ± 0.39%, and 43.3 ± 4.83% cell growth enhancement, with 30 µM 46.8 ± 1.1%, 35.9 ± 2.42%, and 51.4 ± 2.21% closure of the wound and after 60 µM treatment 48.5 ± 0.76%, 45.1 ± 2.36%, and 65.6 ± 1.52% more cell growth enhancement at 6, 12 and 24h respectively in relation to untreated control. The results are shown in **Figure 9B, C,** and **D**.

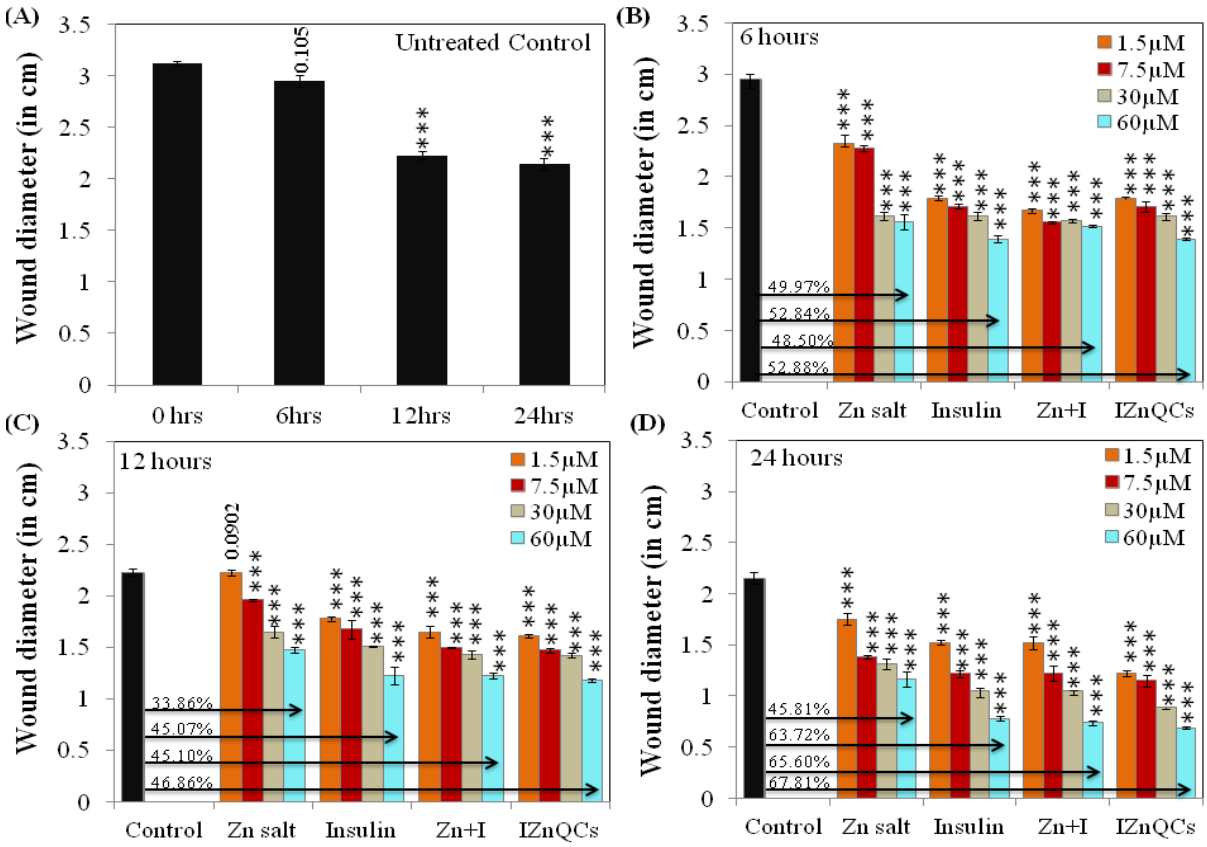

Figure 9: Comparative plots of % of cell migration with respect to control (A) at1.5, 7.5, 30, and 60 µM concentration of Zn salt, insulin, and IZnQCs (B) at 6h, (C) 12h, and (D) 24h. The statistical significance of the data shown with "*": *** P<0.001, ** P<0.01, and * P<0.05.

At 6h insignificant significant differences were observed in cell migration at any concentrations of IZnQCs in comparison with controls (insulin and Zn), and I + Zn combination. With an increase in time, the effect of migration became more prominent and at

24h a faster wound recovery rates were prominent. At lower concentrations, the difference in wound recovery in comparison with various controls (insulin, zinc, and insulin + Zn) was distinguished significantly. At 1.5 µM concentrations of IZnQCs about 14% faster healing of the wound was obtained in comparison with insulin or zinc alone or a combination. At 7.5 µM 5% better wound recovery in comparison to insulin and 3% in insulin in combination with Zn were obtained. Similarly, at 30 µM 5% faster recovery and takes place in comparison to insulin whereas no significant change was observed in comparison with I +Zn. At 60 µM IZnQCs treatment 4% firster recovery took place in comparison to insulin and 2% in comparison to I + Zn. The reason for the reduced difference at higher concentrations may lie in the fact that both insulin and Zinc work through the same pathway and supplement each others work and therefore, at higher concentrations the cellular signaling strength and recovery rate might have reached saturation.

4.3.4. Combination index (CI) of Zinc-insulin: The calculated CI values for different combinations of insulin and Zn salt are less than 1which shows that both behave synergism i.e. two drugs (insulin and Zn) work together and helps each other in enhancing their activity.

Chapter 5: Synthesis, characterization, and *in vitro* wound healing activity of insulin copper quantum clusters (ICuQCs)

5.1. Synthesis

For Insulin copper quantum cluster preparation, 3.47 M fresh insulin was taken and then converted to 1.82 µM and the pH was adjusted to 10.5 using sodium hydroxide (SOLUTION A). Copper sulfate salt solution of similar molarity 1.82 µM was prepared (SOLUTION B) and then these two solutions were mixed and the pH was adjusted to physiological pH 7.4 using 0.1 N HCl. The mixture was kept for incubation in a hot air oven at 37°C and 240 rpm for 48h and resulted in insulin copper quantum clusters (ICuQCs) shown in **Figure 10**.

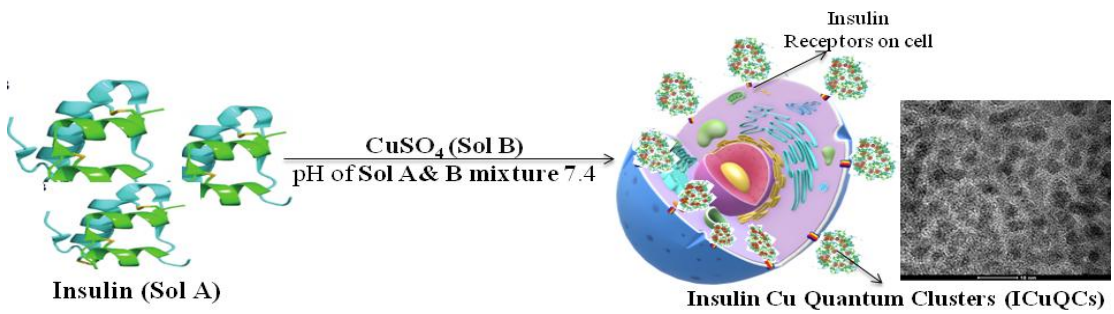

Figure 10: Shows the formation of insulin copper quantum clusters (ICuQCs).

5.2. Characterization

High-resolution transmission electron microscopy (HRTEM), selected area electron diffraction (SAED), UV absorption spectra, and FTIR Spectrophotometer studies were performed to confirm the synthesis of ICuQCs. The quantum yield was determined using fluorescence spectrophotometer studies.

5.3. *In vitro* Assay

The insulin behaves as a growth factor and helps in cell proliferation. Similarly, Cu promotes cell growth helps in cell division. *In vitro* bioimaging and cell growth promotion behavior of ICuQCs was tested.

5.3.1. Cell viability: ICuQCs shows non-toxic behavior. 5% concentration of ICuQCs showed an almost double increase in the growth of cells in 24h when these were compared to control (blank, insulin, salt, and insulin + Cu) indicates the cell growth-promoting effect of ICuQCs.

5.3.2. Bioimaging: To confirm the application of ICuQCs for cellular imaging confocal microscopy was performed using human lung non-small epithelial carcinoma cell line (CCL-185, ATCC, USA) and HeLa, human cervical cancer cell lines (CCL-2, ATCC, USA).

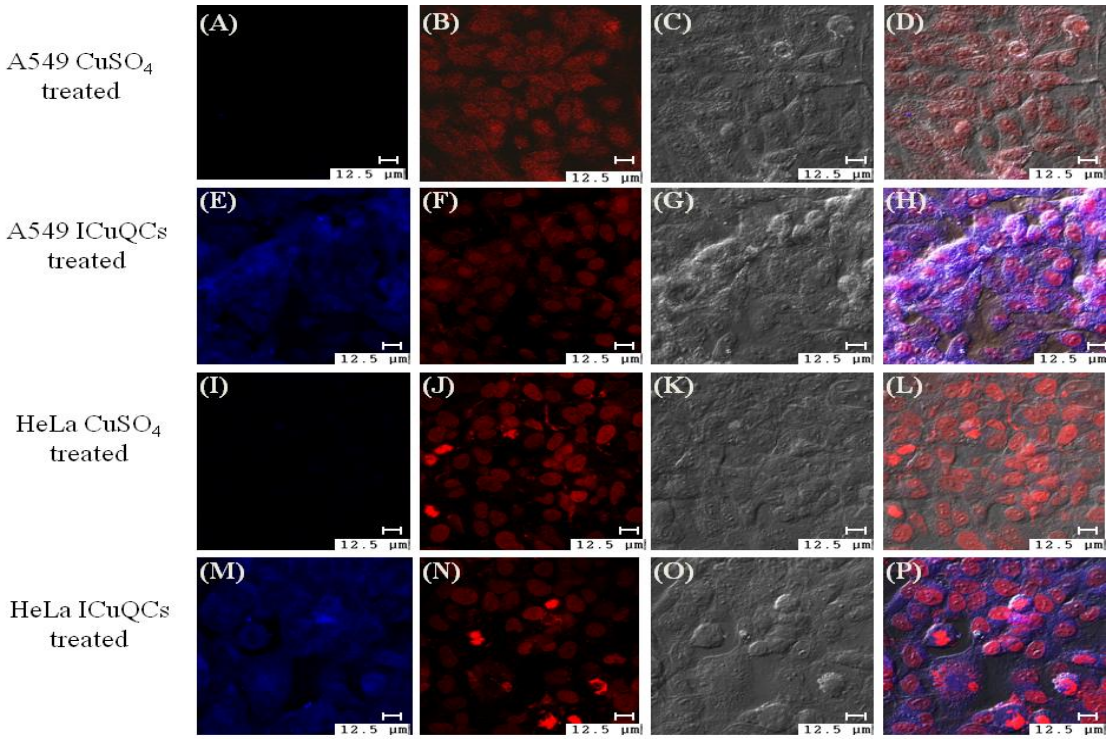

Figure 11: A549 cells (A) treated with $CuSO_4$, (B) nucleus stained with PI, (C) Phase image of the cell, (D) merged imaged of $CuSO_4$ treated and non treated cells, (E) treated with

ICuQCs, (F) nucleus stained with PI, (G) Phase image of the cell, (H) merged imaged of ICuQCs treated and non treated cells and HeLa cells (I) treated with $CuSO_4$, (J) nucleus stained with PI, (K) Phase image of the cell, (L) merged imaged of $CuSO_4$ treated and non treated cells, (M) treated with ICuQCs, (N) nucleus stained with PI, (O) Phase image of the cell, and (P) merged imaged of ICuQCs treated and non treated cells.

After incubation of cells with 1% ICuQCs or insulin (in control) for 2h, cells were treated with RNase A for 3h at 37°C. Thereafter cells were incubated with 1 μg/ml of propidium iodide (PI) before imaging. ICuQCs treated cells showed bright blue fluorescence as a result of the binding of the ICuQCs with the insulin receptors present on the surface of the cells. With $CuSO_4$ no fluorescence was observed for the same cell lines shown in **Figure 11**.

6. Conclusions

The explored nanoformulations of insulin are biocompatible, stable, helps in cell division and migration, and wound healing. The IAgNP showed enhanced *in vitro* cell migration in both diabetic and no diabetic conditions compared to controls. *In vivo* histology evaluation showed a significant decrease in the level of leukocyte infiltration, faster deposition of collagen, and rapid re-epithelization anti-inflammatory activity which is beneficial in treating chronic wounds. The *in vivo* studies showed a rapid decrease in inflammatory (IL-6, and TNF-α) cytokines and an increase in anti-inflammatory (IL-10) cytokines. IZnQCs and ICuQCs showed specific receptor binding, bioimaging, and wound healing properties. In IZnQCs both insulin and zinc showed a synergistic effect through targeting IR and phosphorylating the same. These formulations are helpful in the recovery of the wound as well as monitoring of the wound.

7. Future perspectives

Further intervention is needed to explore the *in vivo* wound healing, anti-inflammatory role and bioimaging role of IZnQCs and ICuQCs. It is also needed to translate these three formulations (IAgNPs, IZnQCs, and ICuQCs) into pre-clinical and clinical models.

8. References

1. Diegelmann RF, Evans MC. Wound healing: an overview of acute, fibrotic and delayed healing. *Front Biosci* 2004;**9**:283-9.
2. Friedstat J, Brown David A, Levi B. Chemical, electrical and radiation injuries. *Clin Plast Surg* 2017;**44**:657-69.
3. Frykberg RG, Banks J. Challenges in the treatment of chronic wounds. *Adv Wound Care* 2015;**4**:560-82.
4. Cardona AF, Wilson SE. Skin and soft tissue infections: A critical review and the role of telavancin in their treatment. *Clin Infect* 2015;**61**:69-78.
5. Negut I, Grumezescu V, Grumezescu AM. Treatment strategies for infected wounds. *Molecules* 2018;**23**:2392.
6. Zhao R, Liang H, Clarke E, Jackson C, Xue M. Inflammation in chronic wounds. *Int J Mol Sci* 2016;**17**:2085.
7. Yamada BFA, Santos VLCG. Quality of life of individuals with chronic venous ulcers. *Wounds* 2005;**17**:178-89.
8. Newberg S. Identifying pain and effects on quality of life from chronic wounds secondary to lower extremity vascular disease: An integrative review. *Adv Skin Wound Care* 2018;**31**:102-8.
9. Renner R, Erfurt Berge C. Depression and quality of life in patients with chronic wounds: ways to measure their influence and their effects on daily life. *Chronic Wound Care Manag Res* 2017;**4**:143-51.
10. Strodtbeck F. Physiology of wound healing. *Newborn Infant Nurs Rev* 2001;**1**:43-52.
11. Khale B, Hermanns HJ, Gallenkemper G. Evidence based treatment of chronic leg ulcers. *Dtsch Arztebl Int* 2011;**108**:231-7.
12. Zuo SA, Di Pietro LA. Factors affecting wound healing. *J Dent Res* 2010;**89**:219-29.
13. Larouche J, Sheoran S, Maruyama K, Martino MM. Immune regulation of skin wound healing: mechanism and novel therapeutic targets. *Adv Wound Care* 2018;**7**:209-31.
14. Dhivya S, Padma VV, Santhini E. Wound dressings: a review. *BioMed* 2015;**5**:24-8.
15. Boateng JS, Matthews KH, Stevens HN, Eccleston GM. Wound healing dressings and drug delivery systems: a review. *J Pharma Sci* 2008;**97**:2892-923.
16. Thu HE, Zulfakar MH, Ng SF. Alginate based bilayer hydrocolloid films as potential slow-release modern wound dressing. *Int J Pharm* 2012;**434**:375-83.

17. Hoffman AS. Hydrogels for biomedical applications. *Adv Drug Deliv Rev* 2012;**64**:18-23.
18. Jude EB, Blakytny R, Blumer J, Boulton AJM, Ferguson MWJ. Transforming growth factor-beta 1,2,3 and receptor type I and II in diabetic foot ulcers. *Diabet Med* 2002; **19**: 440-7.
19. Wu Y, Chen L, Scott PG, Tredget EE. Mesenchymal stem cell enhances wound healing through differentiation and angiogenesis. *Stem cells* 2007;**25**:2648-59.
20. Herman WH. The economic costs of diabetes: is it time for a new treatment paradigm? *Diabetes care* 2013;**36**:1033-46.
21. Wang N, Liang H, Zen K. Molecular mechanisms that influence the macrophage M1–M2 polarization balance. *Front Immunol* 2014;**5**:614.
22. Werner H, Weinstein D, Bentov I. Similarities and differences between insulin and IGF-I: structures, receptors, and signalling pathways. *Arch Physiol Biochem* 2008;**114**:17-22.
23. Saeedi P, Petersohn I, Salpea P, Malanda B, Karuranga, Unwin N, *et al*. IDF diabetes atlas committee. Global and regional diabetes prevalence estimates for 2019 and projections for 2030 and 2045: results from the international diabetes federation diabetes atlas, 9th edition. *Diabetes Res Clin Pract* 2019;**157**:107843.
24. Cho NH, Shaw JE, Karuranga S, Huang Y, Rocha Fernandas JD, Ohlrogge AW, *et al*. IDF diabetes atlas: global estimates of diabetes prevalence for 2017 and projections for 2045. *Diabetes Res Clin Pract* 2018;**138**:271-81.
25. Singh N, Armstrong DG, Lipsky BA. Preventing foot ulcers in patients with diabetes. *J Am Med Dir Assoc* 2005;**293**:217-28.
26. Andersen CA, Roukis TS. The diabetic foot. *Surg Clin North Am* 2007;**87**:1149-77.

LIST OF PUBLICATIONS

1. Kaur P, Choudhury D. Functionality of Receptor Targeted Zinc-Insulin Quantum Clusters in skin tissue augmentation and bioimaging. *J Drug Target* 2020;**14**:1-26.
2. Kaur P, Sharma S, Choudhury SD, Singh D, Sharma S, Gadhave K, *et al*. Insulin-copper quantum clusters preparation and receptor targeted bioimaging. *Colloids Surface B* 2020;**188**:110785.

P50/P65

3. Kaur P, Choudhury D. Insulin Promotes Wound Healing by Inactivating NFkβ and Activating Protein and Lipid Biosynthesis and alternating Pro/Anti-inflammatory Cytokines Dynamics. *Bimol Concepts* 2019;**10**:11–24.
4. Kaur P, Sharma AK, Nag D, Das A, Datta S, Ganguli A, *et al*. Novel nano-insulin formulation modulates cytokine secretion and remodeling to accelerate diabetic wound healing. *Nanomedicine: NBM* 2019;**15**:47–57.

OTHER PUBLICATIONS

1. Goel V, Kaur P, Singla LD, Choudhury D. Biomedical evaluation of *Lansium parasiticum* extract protected silver nanoparticles against *Haemonchus contortus*, a parasitic worm. *Front Mol Biosci* 2020;**17**:595646.
2. Mehta R, Kaur P, Choudhury D, Paul K, Luxami V. Al^{3+} induced hydrolysis of Rhodamine based Schiff-base: Applications in cell imaging and esemble as CN^- sensor in 100% aqueous medium. *J Photochem Photobiol A* 2019;**380**:111851.
3. Kaur P, Gadhave K, Garg N, Deb D, Choudhury D. Probing the interaction of glutathione with different shape nanoparticles by optical spectroscopy. *Mater Today Commun* 2021;**26**:102137.
4. Sharma S, Kaur P,* Choudhury D. Inflammation modulation as a potential treatment for diabetic patients suffering from COVID-19.
5. Goel V, Kaur P, Sharma S, Choudhury D. Silver nanoparticles cause oxidative stress mediated physical damage and death in *Eisenia fetida,* a free living organism.
6. Attri K, Sharda D, Kaur P, Choudhury D. Probing of Pb induced cytotoxicity using paramagnetic nickel insulin quantum clusters.
7. Sharma S, Goel V, Kaur P, Gadhave K, Garg N, Singla LD, *et al*. Targeted drug delivery using beewax derived Albendazole loaded solid lipid nanoparticles in *Haemonchous contortus*, an albendazole tolerate nematode.

8. Kaur P, Ghosh S, Basu B, Choudhury D. Soluble insulin loaded chitoasn nanocapsules for healing of burn wound.